

# Bistable [2]Rotaxane Based Molecular Electronics: Fundamentals and Applications

Thesis by

Jang Wook Choi

In Partial Fulfillment of the Requirements

For the Degree of

Doctor of Philosophy

California Institute of Technology

Pasadena, California

2007

(Defended May 17, 2007)

© 2007

Jang Wook Choi

All Rights Reserved

*Dedicated with Love and Gratitude*

*To Dami, Justin and Alexis*

*And to my dearest parents, Kyungwon Choi and Kisoan Lee*

## Acknowledgement

I would not be able to stand at this point without advice and helps from many people nearby. Here, I like to leave my sincere gratitude toward all who have been in my scientific journey in the past five years.

In my native land of Korea, there is an old saying - the wisest mother is the one who finds home near a school where her children can be educated by the smartest teacher. In such a sense, I found home here in Southern California exactly on time when the best teacher just moved in the school crossby. The period with my primary mentor, Professor Jim Heath, can hardly be described by words of gratitude. Locally, his insightful guidance in all the projects I have been involved in as well as his sharp advice on finding breakthroughs have been always primary driving forces in moving the projects forward and eventually, completing the decent scientific stories. Globally, his endless passion for every single piece of science has been constantly inspiring a number of people in the society including many young scientists as myself and even the general public. I believe that he will maintain his prestige as a true leader in the field for good.

I was even luckier to have another great mentor in a neighboring school. The marvelous fortune to meet Professor Fraser Stoddart is also beyond a simple description. Having such a supportive and experienced scientist directly in all of my molecular electronics projects must have been very rare privilege. Fraser has also shown that one scientist's passion throughout his entire life could flourish the society by sharing scientific visions and joys with younger generations over the years. On other collaboration sides, I would appreciate Professor Bill Goddard for molecular dynamic

studies on rotaxane molecules, and Professor Bob Grubbs for the supports of polymers in the nanofluidic project.

Also, I can not forget all of my group members for sharing pleasure and frustration on real job spots: Especially, Dr. Yi Luo and Dr. Amar Flood were great mentors in teaching detailed experimental and problem-solving skills in the very beginning of research. I thank Jonathan Green for the perfect teamwork in the 160 kbit memory project and Ehud Vermesh for thorough help in the nanofluidic project. I also appreciate John Nagarah for numerous joyful discussions at many nights. Conversation with John was always a fun and was very helpful in forgetting research problems during the day. Many Korean friends will be in my memory forever as well. I feel very grateful and indebted for their sharing in scientific visions and general life. Finally, and most importantly, I would give my best heart to my lovely family, Dami, Justin and Alexis. I am literally a lucky person to have Dami as a companion for my lifetime journey. Thank you very much for all of your love, support and tolerance. All the wonderful moments with my adorable kids, Justin and Alexis, will also remain as a great happiness forever. Above all, I thank God, my Lord, with my true sincerity for being in my mind all the time and giving confidence at every hard moment.

All of the works in this thesis were funded from the Defense Advanced Research Projects Agency (DARPA), Samsung Lee Kun Hee Scholarship Foundation (SLSF) and Caltech.

Chapter 1 is taken in part from “Recent advances in molecular electronics,” in *CRC Handbook of Nanotechnology*, in press, 2006.

Chapter 2 is taken in part from “Ground-state equilibrium thermodynamics and switching kinetics of bistable [2]rotaxanes switched in solution, polymer gels, and molecular electronic devices,” *Chem. Eur. J.*, 2006, 12, 261-279. Copyright 2006 Wiley-VCH Verlag GmbH.

Chapter 3 is taken in part from “A 160 kilobit molecular electronic crossbar memory circuit patterned at  $10^{11}$  Bits per square centimeter,” *Nature*, 2007, 445, 414-417. Copyright 2007 Nature Publishing Group.

## Abstract

Bistable [2]rotaxanes are a unique class of supramolecules that have two constitutional isomers. Upon sandwiched between two electrodes, these two isomeric states show different conducting states, thus behaving as molecular switches. In this thesis, I describe how the bistable [2]rotaxanes have been investigated to ensure that the switching characteristics in solid-state devices are those of the bistable [2]rotaxanes and not those of extraneous elements. In addition, integration of these molecules onto ultra-dense nanowire arrays to constitute a memory circuit is presented.

The bistable [2]rotaxanes have been examined in various environments to study kinetics and ground-state thermodynamics between both isomeric states. In the kinetic study, as molecules are embedded in more viscous environments (solution→polymer gel→solid-state device), a key step in switching cycle slows down significantly, thus reflecting the environments where the molecules are surrounded. In thermodynamic study, one of the major units in the molecular structure was modified and then equilibrium population ratio between both isomeric states was monitored at various temperatures. In both solution and solid-state devices, the population ratio of the modified [2]rotaxane was more sensitive to temperature. This result is very critical in that the properties of devices can be tailored by manipulating the structure of molecular components.

The bistable [2]rotaxanes were integrated into crossbar nanowire arrays to constitute a memory circuit. Ultra-dense nanowire arrays used as electrodes are generated by superlattice nanowire pattern transfer (SNAP) method. Due to extremely narrow pitch ( $\sim 33$  nm) of the SNAP nanowire arrays, the device sets a remarkable record in memory density ( $\sim 10^{11}$  Bits/cm<sup>2</sup>). Although the circuits were found to have large

numbers of defects, those defects were identified through electronic testing and the working bits were configured to form a fully functional random access memory for storing and retrieving information.

Finally, nanofluidic devices have been developed by utilizing the SNAP method. Due to small channel dimensions ( $<$  Debye screening length), passage of ions was modulated by electrostatic interactions between the ions and the nanochannel walls. Devices are being developed to quantify isoelectric points of peptides so that ultimately, the device could function as a protein identifier at a single molecule level.

# Table of Contents

Acknowledgement .....	iv
Abstract .....	vii
Table of Contents .....	ix
List of Figures and Tables .....	xi
Chapter 1	Overview: Molecular electronics and nanofluidics..... 1
1.1	Introductions: Recent Advances in Molecular Electronics..... 1
1.2	The Molecule/Electrode Interfaces..... 3
1.3	Spectroscopy of Molecular Electronic Devices..... 5
1.4	Electrode Materials..... 8
1.5	Molecular Rectifiers..... 10
1.6	Surface Immobilized Molecular Switches..... 12
1.7	Heath/Stoddart Switching Molecules: Basics and Directions..... 15
1.8	Scale-down: 160 kbit Molecular Electronic Memory Circuits..... 20
1.9	Nanofluidics..... 21
1.10	Structure and Scope of the Thesis..... 22
1.11	References..... 22
Chapter 2	Ground State Equilibrium Thermodynamics and Switching Kinetics of Bistable [2]Rotaxane Switched in Solution, Polymer Gels, and Molecular Electronic Devices..... 31
2.1	Introduction..... 31
2.2	Molecular Design..... 39
2.3	Kinetics and Thermodynamics of Switching in Solution and in Polymer Electrolytes..... 44
2.4	Kinetics and Thermodynamics of Molecular Switch Tunnel Junctions..... 53
2.5	A Summary of Kinetic and Thermodynamic Studies in All of Three Environments..... 65
2.6	Conclusion..... 70

2.7	References.....	71
Chapter 3	Molecular Electronic Crossbar Memory Circuits .....	79
3.1	Introduction.....	79
3.2	Superlattice Nanowire Pattern Transfer (SNAP) Method .....	86
3.3	160 kbit Molecular Electronic Memory Circuits: Overview .....	91
3.4	160 kbit Molecular Electronic Memory Circuits: Fabrication Flow ...	93
3.5	160 kbit Molecular Electronic Memory Circuits: Device Testing.....	106
3.6	Limitations of the SNAP Process for Crossbar Memory Formation .	117
3.7	Conclusion .....	118
3.8	References.....	120
Chapter 4	Nanofluidics .....	125
4.1	Introduction.....	125
4.2	Device Fabrication .....	128
4.3	Toward Single-Molecule chemical filters.....	130
4.4	Conclusion and Future Work: Toward Quantification of Isoelectric Point via Gating Bias .....	144
4.5	References.....	146
Appendix A	Syntheses of the [2]Rotaxanes RBPTTF•4PF <sub>6</sub> and RBLOCK•4PF <sub>6</sub> .....	148
Appendix B	LabWindow Code for Memory Measurement .....	171

## List of Figures and Tables

Chapter 1	
Figure 1-1	Raman spectrum of NAB with varying Ti thicknesses..... 7
Figure 1-2	Molecular rectification from Au-S-(CH <sub>2</sub> ) <sub>3</sub>  A <sup>+</sup> -π-D structures..... 12
Figure 1-3	Molecular switching of pseudo-rotaxanes driven by biological reactions..... 15
Figure 1-4	Bistable molecular mechanical switching molecules, each with similar recognition groups ..... 16
Figure 1-5	Molecular switching of bistable [2]rotaxanes ..... 18
Chapter 2	
Figure 2-1	Molecular structure and potential energy surface of bistable [2]rotaxane..... 33
Figure 2-2	Structural formulas of the translational isomers of the bistable rotaxanes ..... 36
Figure 2-3	Control studies for designing stations in bistable [2]rotaxanes ..... 40
Table 2-1	Thermodynamic binding data corresponding to the complexation between CBPQT <sup>4+</sup> and the individual components of the bistable rotaxane..... 41
Figure 2-4	CV data of RBPTTF <sup>4+</sup> recorded in acetonitrile and polymer gel..... 46
Figure 2-5	The first CV cycles of RBPTTF <sup>4+</sup> , RATTF <sup>4+</sup> and RBLOCK <sup>4+</sup> recorded at various temperatures..... 47
Figure 2-6	Normalized CV data in the second cycles..... 50
Figure 2-7	MSCC→equilibrium kinetics of RBPTTF <sup>4+</sup> in solution and polymer phases..... 51
Figure 2-8	Switching responses of three rotaxanes within MSTJs..... 56
Figure 2-9	Decay curves of RTTF <sup>4+</sup> and RBPTTF <sup>4+</sup> MSTJs recorded as a function of temperature..... 58
Figure 2-10	Schematic representation of a volatility curve defining I <sub>CLOSED</sub> and I <sub>OPEN</sub> ..... 62

Table 2-2	Kinetics data for the relaxation from the MSCC to the GSCC for RBPTTF <sup>4+</sup> and the free energy barriers for RATTF <sup>4+</sup> and RTTF <sup>4+</sup> .	66
Figure 2-11	The temperature-dependent GSCC/MSCC equilibria and Eyring plots of the MSCC → GSCC relaxation process .....	67
Chapter 3		
Figure 3-1	A nanoscale molecular computational platform .....	82
Figure 3-2	A series of crossbar molecular electronic memory circuits .....	86
Figure 3-3	SEM images of Si nanowire arrays of 15 nm pitch and 1400 wires .	88
Figure 3-4	SNAP process flow .....	90
Figure 3-5	The process flow for preparing the 160 kbit molecular electronic memory circuit at 10 <sup>11</sup> bits/cm <sup>2</sup> .....	94
Figure 3-6	Scanning electron micrographs of the nanowire crossbar memory fabrication process .....	96
Figure 3-7	Conductance monitoring during the Ti layer etching .....	102
Figure 3-8	Scanning electron micrographs (SEMs) of the NW crossbar memory .....	105
Figure 3-9	Writing and reading procedures in crossbar memory measurements .....	108
Figure 3-10	Data from evaluating the performance of the 128 ebits within the crossbar memory circuit .....	110
Figure 3-11	A map of the defective and useable ebits, along with a pie chart giving the testing statistics .....	113
Figure 3-12	A demonstration of point-addressability within the crossbar .....	114
Figure 3-13	A histogram representing the 1/e decay time of the ‘1’ state to the ‘0’ state .....	116
Chapter 4		
Figure 4-1	Scanning electron micrograph (SEM) images of nanofluidic devices .....	129
Figure 4-2	Nanofluidic device and characterization set up .....	130

Figure 4-3	Nanochannel wetting progress .....	133
Figure 4-4	Diffusion of a cationic dye .....	134
Figure 4-5	Diffusion of an anionic dye.....	135
Figure 4-6	Diffusion of a zwitterionic dye .....	140
Figure 4-7	Bias measurements for the charge determination of the zwitterionic dye .....	142

## Chapter 1

### Overview: Molecular Electronics and Nanofluidics

#### 1.1 Introductions: Recent Advances in Molecular Electronics

The field of molecular electronics is largely based on harnessing the power and versatility of chemical synthesis to control the properties of electronic devices and circuits. This field, which dates back several decades, has exploded in recent years. The reasons behind this are multifold. First, researchers have become increasingly adept at synthesizing molecules that are potentially interesting from the perspective of molecular electronics device properties. Second, rigorous surface science methods have been adapted for the task of quantitating the properties of the molecule/electrode interface. Third, continued scaling of electronics devices to nanometer dimensions has brought added incentive to this field. Fourth, a few theoretician are beginning to generate reliable and predictive models that go well beyond capturing ‘model’ systems but instead are beginning to yield real insight into more complex and realistic device properties. Finally, a host of new and unique device demonstrations that are enabled by both the molecules and the electronics platforms have been reported. For example, within recent years, molecular electronic switches (1, 2), light harvesting devices (3), molecular electronic based random access memory and configurable logic circuits (4), molecular mechanical biosensors (5), actuated molecular valves (6), ion channel mimics (7), molecular muscles (8-11), and novel electrochromic devices (12) have all been demonstrated, and in each of these demonstrations the molecules have played an active and critical role.

A key result that has emerged over the past year or two has been the ability to measure the properties of a particular molecular electronic solid state device, and then to utilize those measurements to optimize and improve the device through solution-phase chemical synthesis. In other words, for at least a few systems, a feedback loop that links the properties of molecular electronic devices to properties that can be optimized through chemical synthesis has been established.

This chapter consists of two major stories in different streams: the first and major story will be on molecular electronics, whereas the second and relatively minor story will be on nanofluidics. They are tied together, however, in that the nanofluidics story relies on technological and nanofabrication advances that were achieved in the arena of fabricating and testing ultra-high density molecular electronic circuitry.

For molecular electronics, I will cover a subset of the recent advances in this field including those from my research group. First, I will review molecular electronic devices in which the molecules constitute the active (and thus enabling) element within the devices. For any molecular electronic device, understanding and controlling the molecular electronic interface is a necessity, and this will be the second highlighted topic. The recent application of infrared and Raman spectroscopies towards interrogating molecular monolayers – even when they are sandwiched between two electrodes, has opened up a powerful window into understanding these interfaces. Finally, switching molecules that have been developed and characterized in the Heath/Stoddart groups will be focused. Not only will be fundamental background of the molecules such as the correlation of molecular structure with the switching mechanism be covered, but I will

also discuss how the physical environment of the molecular switch influences molecular mechanical switching mechanism.

In the nanofluidics, I will introduce a first generation device that is ultimately intended as a platform for protein discovery and identification. Preliminary results on model systems will be discussed.

## **1.2 The Molecule/Electrode Interfaces**

To a great extent, the success of molecular electronics will depend on whether the molecule/electrode interface can be understood and designed to optimize the exploitation of the designed molecular properties. Several molecular electronics devices, including rectifiers and molecular switch tunnel junctions (MSTJs), consist of a molecular monolayer sandwiched between two electrodes – and so are called two-terminal (2T) devices. 2T devices are not only interface-rich devices, but they are also devices in which the molecules are not easily characterized since they reside at a buried interface.

Fabrication techniques for the preparation of two-terminal sandwich devices include the use of self-assembled monolayers (SAMs), usually on gold or platinum surfaces, Langmuir-Blodgett films on metal or silicon surfaces, and the covalent attachment of molecules onto SiO<sub>2</sub> or silicon surfaces. Deposition of the top electrode is potentially a process that can damage the molecules, and so a number of methods have been reported with the object of avoiding or minimizing such damage. Examples include the use of a mercury drop (13-16) or an STM tip as the top electrode. These methods, while clearly non-destructive, are also limited to single device demonstrations. More scaleable methods, such as electron-beam or sputtering deposition of the top electrode

materials, are more general but potentially more damaging. Ideally the deposited metal will adhere to, but not destroy or penetrate, the molecular film. In addition, the metal/molecular interface should not dominate charge transport through the junction. If it does dominate, then the molecular properties themselves are difficult to interrogate using charge transport methods.

This interface has historically been very difficult to study, and, until recently investigations were primarily limited to the use of X-ray photoelectron spectroscopy (XPS) (17). However, those studies are now complemented by surface-sensitive infrared and Raman spectroscopies, atomic force microscopy (AFM) and time of flight secondary ion mass spectroscopy (TOF-SIMS) (18-24).

Studies have shown that if a deposited metal does not chemically react with the molecular layer in some way, device failure can also occur through penetration of the metal through the monolayer (and thus cause device shorting). If the metal does chemically react, then that reaction can either destroy or protect the functional properties of the molecular monolayer. For cases in which the molecules are small and/or loosely packed on a surface, metal deposition can be irreversibly damaging to the monolayer. However, many research groups have shown that when the molecule/metal system is designed carefully, the desired molecular functionality can remain intact upon deposition of the top electrode. This has been achieved by incorporating a reactive or sacrificial molecular moiety, thereby “protecting” the desired functional groups. Examples include designing the interface that the molecules present to the deposited metals with functionalities that will react with and adhere to those metals, such as thiols with Au or

Al (25). For more reactive metals, such as Ti, bulky molecular groups at the interface can, via steric interactions, prevent the penetration of impinging metal atoms (1, 18).

Even if the deposited metals neither short the devices nor destroy the molecules, they can still strongly influence the measured device properties. McCreery and coworkers investigated the role of background O<sub>2</sub> during the formation of a Ti/molecule interface(26) and found that trace amounts of O<sub>2</sub> ( $5 \times 10^{-7}$  Torr) can influence both the resistance and the rectifying characteristics of the junction.

For some devices, such as single- or few-molecule break junctions(27-33), both metal electrodes are effectively deposited prior to deposition of the molecular component. Such devices allow for an independent assessment of how the composition of the molecule/electrode interface can influence charge transport through the molecule. In certain cases those interfaces have been found to be rate limiting to charge transport, meaning that the molecule/electrode interface can dominate the measured charge transport characteristics(34, 35).

### **1. 3 Spectroscopy of Molecular Electronic Devices**

Researchers have recently begun to quantitatively characterize these interfaces by correlating spectroscopic analysis of the devices with device transport measurements.

By choosing a molecule/electrode system that was amenable to study with Raman spectroscopy, Nowak and McCreery have done a series of experiments on carbon/nitroazobenzene (NAB)/titanium/gold devices (21, 36). They have studied both how the titanium/gold evaporated film affects the molecular structure of the devices and the changes in the molecular layer with varying Ti top electrode thickness, over time

(from < one hour to two weeks) and with applied voltages. Upon evaporation of Ti onto the molecular layer of NAB, XPS shows formation of a Ti-N bond (21) and Raman spectroscopy shows that the NO<sub>2</sub> Raman modes are decreased (indicating some reduction of the NAB), which partially recover over a period of several days.

Spectroscopic feedback on these devices is especially interesting when coupled with electrical transport measurements. Figure 1-1 is adapted from reference 36(36). Figure 1A shows the molecular structure of NAB. Figure 1-1B illustrates the affect that the Ti evaporation has on the Raman spectrum of NAB with varying Ti thicknesses (from 1 to 5 nm). The spectrum shows a steady decrease in the peaks at 1107 (phenyl-NO<sub>2</sub> stretch), 1340 (NO<sub>2</sub> stretch) and 1450 (N=N vibration) with increasing Ti thickness. Similar changes take place when the NAB is reduced in a spectroelectrochemical experiment, indicating that the Ti reduces the NAB as it evaporates. Figure 1-1C summarizes some of the electrical measurements. Only the Raman modes assigned to the azo stretches (1401 and 1450 cm<sup>-1</sup>) show changes with applied voltage. The ratio of the peak intensities for the 1401 and 1450 cm<sup>-1</sup> bands indicates the oxidation state of the NAB molecule. When +3 V (carbon relative to Ti/Au) is applied, the molecule is reoxidized. The authors are able to reverse the oxidation when the voltage polarity is reversed to -1V (up to three times). This groundbreaking study represents one of the most complete characterizations of molecules embedded within 2T devices.

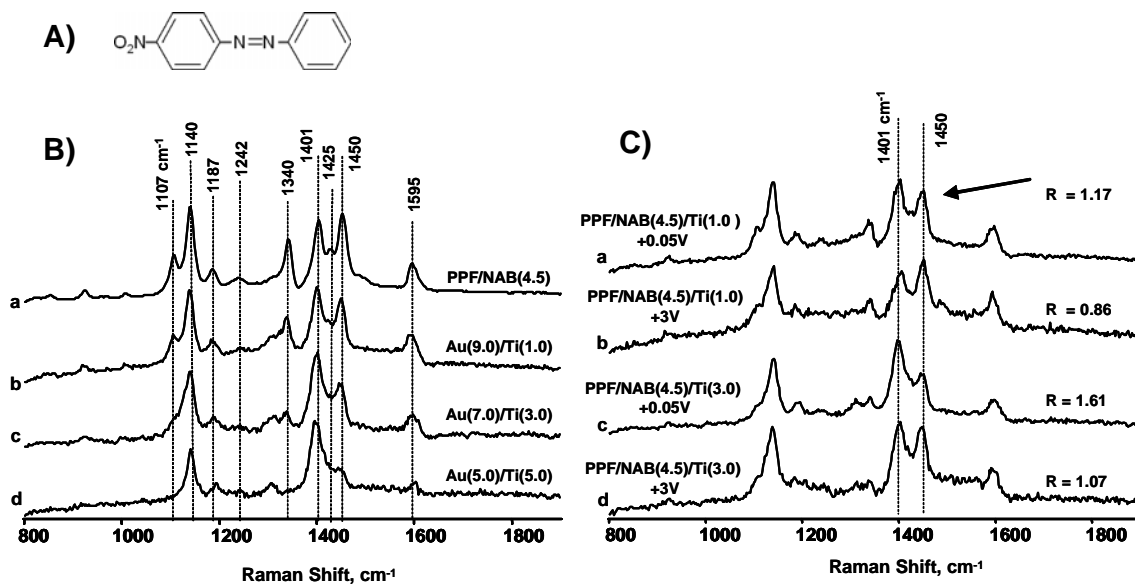


**Figure 1-1.** Raman spectrum of NAB with varying Ti thicknesses. (A) Structure of nitroazobenzene. (B) Raman spectra of PPF/NAB(4.5) surfaces before (a) and after (b-d) deposition of top contact. (C) Raman spectra of PPF/NAB(4.5) junctions with an applied bias voltage. Spectra b and d were acquired after a total of 270 s at +3 V (PPF relative to Ti).  $R$  is the ratio of peak intensities for the 1401 and 1450  $\text{cm}^{-1}$  bands, measured relative to baseline. Reproduced with permission from reference 36. Copyright 2004 American Chemical Society.

Dr. DeLonno in my research group has investigated MSTJ devices, in which the molecular components are bistable, electrochemically switchable [2]catenanes or [2]rotaxanes(37). For these devices, spectroscopy on a device is not practical due to the very small cross-section of the active area ( $50 \mu\text{m}^2$  to  $\sim 100 \text{nm}^2$ ) and the choice of electrode materials. For a device that cannot be spectroscopically measured directly, spectroscopic measurements can be taken on a device analog and the current-voltage characteristics of the device can be correlated to the spectroscopic data. Dr. DeLonno performed a study on poly-Si/[2]rotaxane/Ti/Al crossbar MSTJs. The purpose of the

study was to determine the effect of transferring Langmuir monolayers at different pressures, and therefore different areas/molecule on device performance. Fourier transform reflection absorption infrared spectroscopy (FT-RAIRS) was used to determine the effect of Ti evaporation on the monolayers at the different pressures. The study showed that the transfer pressure of the monolayer affects both the FT-RAIRS and the transport properties. For lower transfer pressure, (i.e. larger area per molecule), the Ti metal evaporation affected a larger part of the molecule, leading to increased current and reduced switching performance in the devices.

#### **1.4 Electrode Materials**

Although metal has been the most commonly used electrode material, silicon has gained increasing interest due to existing infrastructure surrounding silicon-based devices, as well as the interesting material properties. Historically, my research group has fabricated the MSTJ devices using silicon (either poly-silicon or silicon-on-insulator (SOI), both passivated with the native oxide) (1), as the bottom electrode. These devices yield data that can be correlated back to the structure and physical properties of the molecule within the junction. Metal electrodes, by contrast (38), tend to yield molecule-independent device responses that originate from electrochemical processes or electromigration (filament formation) at the metal surface. More recently, there have been several in depth STM studies on silicon as an electrode material (39-44).

In collaboration with Lewis' group, my research group has studied a methyl-passivated silicon (111) surface with low temperature scanning tunneling microscopy (43). For this work, the Si(111) surface was initially chlorinated, and then alkylated using

the methyl Grignard reagent (45). This passivation yields a nearly atomically perfect surface, removing interface states (46) as well as stabilizing against oxidation. Several other groups have investigated silicon surfaces, typically with STM probes. For example, rectifying devices (47) as well as bistable switching of chemisorbed molecules (48) have been demonstrated.

Several interesting ultra high vacuum (UHV) STM studies have been done by Hersam group on silicon (100) surfaces. This surface, while more common to semiconductor manufacturing, does not yet have an accompanying chemistry that can render it stable to oxidation. Hersam and colleagues have studied a series of different molecules on both p-type and n-type Si(100). They have shown (and modeled using theory) negative differential resistance (NDR) signatures from several molecules (40-42). This work takes advantage of the silicon band edge to study the NDR effect. Depending on the silicon doping, NDR is seen at either positive (for p-type Si) or negative (for n-type Si) bias. In addition, they have studied the effect of packing density on transport and shown that for two molecules, cyclopentene and 2,2,6,6-tetramethyl-1-piperidinyloxy (TEMPO), suppression of NDR occurs with increased packing density.

Another interesting result from the same group relates to the motion of individual organic molecules on the Si (100)-2 X 1 surface (49). They have shown that by using different molecules, they were able to predictably control molecular motion over the surface. Specifically, 4-methoxystyrene molecules were observed to translate laterally during STM imaging, while styrene molecules showed no detectable motion. They theorized that the additional rotational degree of freedom in the 4-methoxystyrene versus styrene was enabling the motion. They synthesized a third molecule, 5-vinyl-2,3-

dihydrobenzofuran, where the rotational degree of freedom is suppressed, which also led to the suppression of motion on the Si surface. These types of fundamental studies may eventually lend an additional degree of control over the behavior of molecules on surfaces.

## 1.5 Molecular Rectifiers

In 1974, Aviram and Ratner suggested the basic concept of molecular rectification. They proposed that a molecule, comprised of a donor-( $\sigma$ -bridge)-acceptor sequence, could preferentially flow electrons in one direction(50), leading to asymmetric electronic transport. Based on this initial theory, many experimental groups have demonstrated molecular rectification (51-62) and have shown that modifications to the molecule can lead to changes in the rectification ratios, in a predictable way(51, 52, 56, 63).

A challenge in the fabrication of these devices is that rectification in a molecular electronic device is not always due to the molecular component. For example, it has been shown that in a junction (electrode/molecule/electrode), rectification can arise from the molecule/electrode interface (60, 61). Therefore, careful selection of the electrode material is critical. Oxidizable electrodes can give rise to a current-voltage asymmetry (18, 60-62, 64). In addition, asymmetric coupling of the molecular film to the electrodes can contribute to rectification, potentially masking or distorting the rectification from the molecule (60, 65).

Ashwell's group has demonstrated molecular rectification in a number of systems (51-58, 63). Critical to their work has been the both control experiments and careful selection of electrode materials. They prepared self-assembled monolayers of donor-( $\pi$ -

bridge)-acceptor structures on gold substrates, which were probed by a Au or PtIr scanning tunneling microscope (STM) tip. The donor-( $\pi$ -bridge)-acceptor structure was located in the center of the junction, by attaching the same length of alkyl chain to the STM tip and to the SAM on the substrate. In this way, they were able to exclude rectification effects from the molecule/electrode interface. Furthermore, they observed the reversible suppression of the rectification (51, 58) when donor-( $\pi$ -bridge)-acceptor structure was chemically perturbed by HCl, which protonates the acceptor moiety. The rectification was restored when the device was exposed to NH<sub>3</sub>.

More interestingly, the Ashwell's group (51, 52, 63) has also demonstrated the highest rectification ratio to date,  $\sim 450$  at 1 V, from Au-S-(CH<sub>2</sub>)<sub>3</sub> | A<sup>+</sup>- $\pi$ -D structures (figure 1-2a). They first covalently attached 3-mercapto-1-propanesulfonate anion onto a gold substrate. Then, a *N*-methyl-5-(4-dibutylamino-benzylidene)-5,6,7,8-tetrahydroisoquinolinium cation (A<sup>+</sup>- $\pi$ -D) was aligned to the anion on the surface by self-organization. They attributed the very high rectification ratio to the fact that the ionic coupling allows one to maintain the polarity of the molecular structure more efficiently, as compared to LB films and SAMs of same dye molecule in which the iodide counterion induces a dipole reversal, thereby reducing the rectification. In a similar study on the molecular rectification from LB films, my research group (59) demonstrated a rectification ratio of 18 at 0.9 V from a dye molecule of tetrathiafulvalene (TTF) donor-( $\sigma$ -bridge)-tetracyanoquinodimethane (TCNQ) acceptor. They attributed the rectification to the strong donor/acceptor character and this claim was supported by cyclic voltammogram (CV) data as well as molecular dynamic (MD) calculations. Even more

compelling is the fact that if the sequence of donor and acceptor moieties is reversed, the direction of rectification is also reversed.

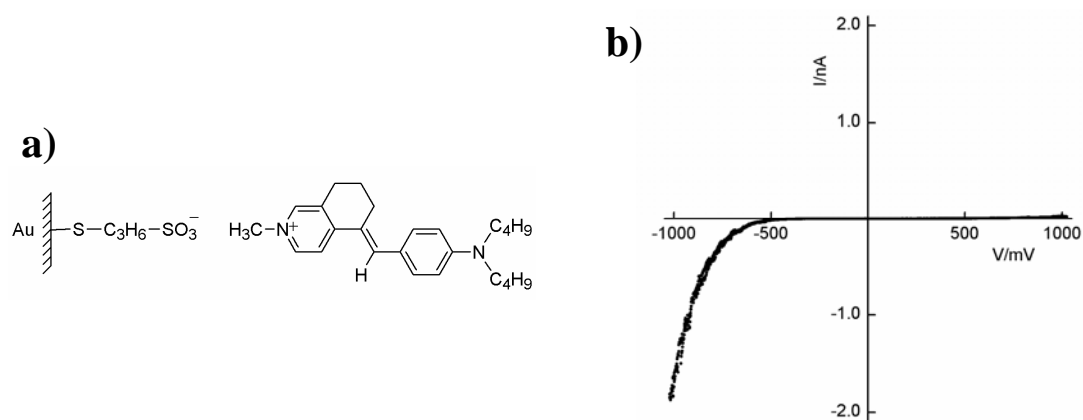


**Figure 1-2.** Molecular rectification from Au-S-(CH<sub>2</sub>)<sub>3</sub> |A<sup>+</sup>- $\pi$ -D structures. (a) Molecular structures of the chemisorbed 3-mercaptopropylsulfonate anion and ionically coupled *N*-methyl-5-(4-dibutylaminobenzylidene)-5,6,7,8-tetrahydroisoquinolinium cation. (b) I-V characteristics from the molecule shown in (a) contacted by a PtIr probe. Data were obtained for a set point current of 0.1 nA and substrate voltage of  $-0.1$  V and averaged for ten scans from the same site. The bias is designated by the sign of the substrate electrode. Reproduced with permission from reference 61. Copyright 2006 Royal Society of Chemistry.

## 1.6 Surface Immobilized Molecular Switches

Molecular electronic devices such as switches represent a more sophisticated molecular electronic device than rectifiers or resistors. This area has also advanced significantly over the past few years, with most work being carried out on bistable [2]rotaxanes, pseudorotaxanes, and [2]catenanes. These classes of switching molecule

have been studied mostly in two major platforms: immobilized on the surface by as self-assembled monolayers (SAMs) or using Langmuir-Blodgett (LB) technique and then embedded between two electrodes, thus mainly functioning as molecular switch tunnel junction (MSTJ) devices. Among these platforms, in this subchapter, I discuss the work on surface immobilized molecular switches accomplished by many groups in various applications.

Investigations of catenanes and rotaxanes prepared as molecular monolayers (Langmuir-Blodgett (LB)) films (66-68) or self-assembled monolayers (SAMs) (7, 66, 69), date back more than a decade, beginning with the early work of Lu, et al. in 1993 (70), with considerable amount of early work dedicated to the fabrication of these monolayers. More recent work has been focused on detecting and harnessing the molecular mechanical motions of bistable rotaxanes, pseudorotaxanes, and catenanes prepared as in LB films, SAMs, and other molecular monolayers. Recent works have shown that these molecular switches are controllable by appropriate chemical, electrochemical and optical stimuli.

Optically driven switching processes(3, 67, 70-72) have been demonstrated by several groups. Chia et al. (73) demonstrated the photochemically and chemically-induced reversible threading of pseudorotaxanes anchored onto a sol-gel surface, and found evidence for reversible threading that correlated well with similar measurements in the solution phase.

Electrochemically driven switching processes (74, 75) for different applications have also been demonstrated. Fitzmaurice's group has investigated both pseudorotaxanes (76) and bistable [2]rotaxanes (77) bound to the surfaces of TiO<sub>2</sub> nanoparticles. They

reported that a crown ether ring could be threaded onto the pseudorotaxane after the tripodal viologen was assembled onto the nanoparticle surface. For the case of the [2]rotaxane, it was also possible to electronically address and switch the bound rotaxane, through a process that involved transferring between one and four electrons from the conduction band of the TiO<sub>2</sub> nanoparticle to the viologen recognition sites. More recently, they developed a new NMR technique (78), paramagnetic suppression spectroscopy (PASSY), which allowed them to see structural conformation of these switching molecules at different redox states.

Other groups have utilized the electrochemical driven switching processes as molecular valves. Kim's group (7) has demonstrated chemically-induced reversible threading of a pseudorotaxane SAM on Au surface. A novel aspect of this work was that the threading/dethreading process could be utilized as a gate, allowing or preventing access of ions to the electrode surface. This striking result led the authors to make an analogy with how ion channel proteins gate ion transport in and out of cells. Hernandez, et al. (6) also covalently bonded pseudorotaxanes to the surface of a mesoporous material. Initially, the pores were diffusion-filled with a fluorophore, and then a CBPQT<sup>4+</sup> ring was threaded. Reduction of the CBPQT<sup>4+</sup> ring with NaCNBH<sub>3</sub> led to the dethreading of the rings from 1,5-dioxynaphthalene (DNP) recognition site, which was followed by the release of the fluorophore.

Electrochemically driven switching processes have also been applied as biological sensors. Willner's group (5) has reported a rotaxane self-assembled onto an Au electrode. This molecule was utilized to shuttle charge between a redox-active enzyme and the surface (figure 1-3). In that work, the linear component of a pseudorotaxane

incorporating a diimine recognition site was assembled stepwise on the Au surface, threaded with a  $\text{CBPQT}^{4+}$  ring, and then stoppered with flavin adenine dinucleotide (FAD). The FAD provides for a binding site for glucose oxidase enzyme. They demonstrated that, under open circuit conditions, the oxidation of glucose leads to a reduction of the  $\text{CBPQT}^{4+}$  ring on the rotaxane. This results in a translation of the ring to a position close to the electrode, where it is re-oxidized and then returns to the diimine recognition site. Thus, the  $\text{CBPQT}^{4+}$  ring acts as a charge shuttle between the Au electrode and the glucose oxidase.

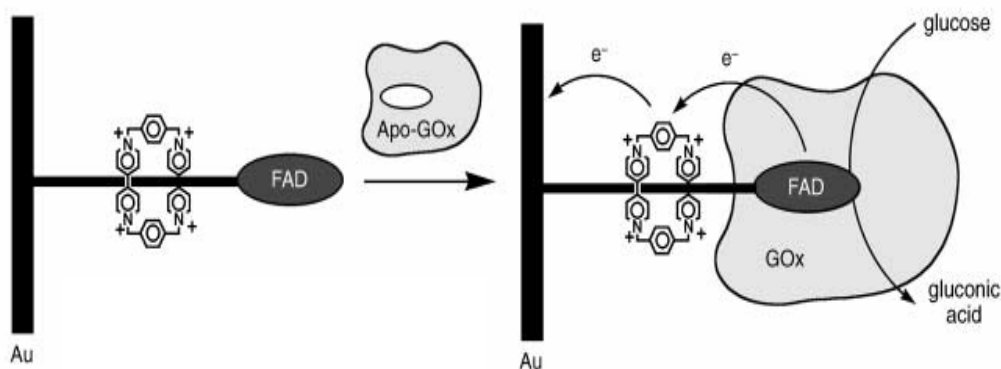


**Figure 1-3.** Molecular switching of pseudo-rotaxanes driven by biological reactions. Schematic representation of binding apo-GOx on pseudorotaxane-FAD self-assembled onto an Au and the mechanism of bioelectrocatalytic oxidation of glucose. Reproduced with permission from reference 5. Copyright 2004 Wiley-VCH Verlag GmbH.

### 1.7 Heath/Stoddart Switching Molecules: Basics and Directions

In the next platform, switching molecules embedded between top and bottom electrodes, Heath/Stoddart groups have made significant progresses into achieving a

better understanding of their switching mechanism within such confined environments including quite complex memory circuits, which require the integration of the switching molecules with a nanowire crossbar array.

In general, bistable [2]catenanes and [2]rotaxanes consist of two mechanically interlocked (or threaded) components. The two interlocked components are oriented with respect to one another in either of at least two conformations through non-bonding interactions. The detailed structures of those molecules are presented in figure 1-4. While studies for both [2]catenanes and [2]rotaxanes have been performed to almost identical extent, the major focus of my studies has been on a set on [2]rotaxanes. Therefore, [2]rotaxanes will lead the story in the following chapters.

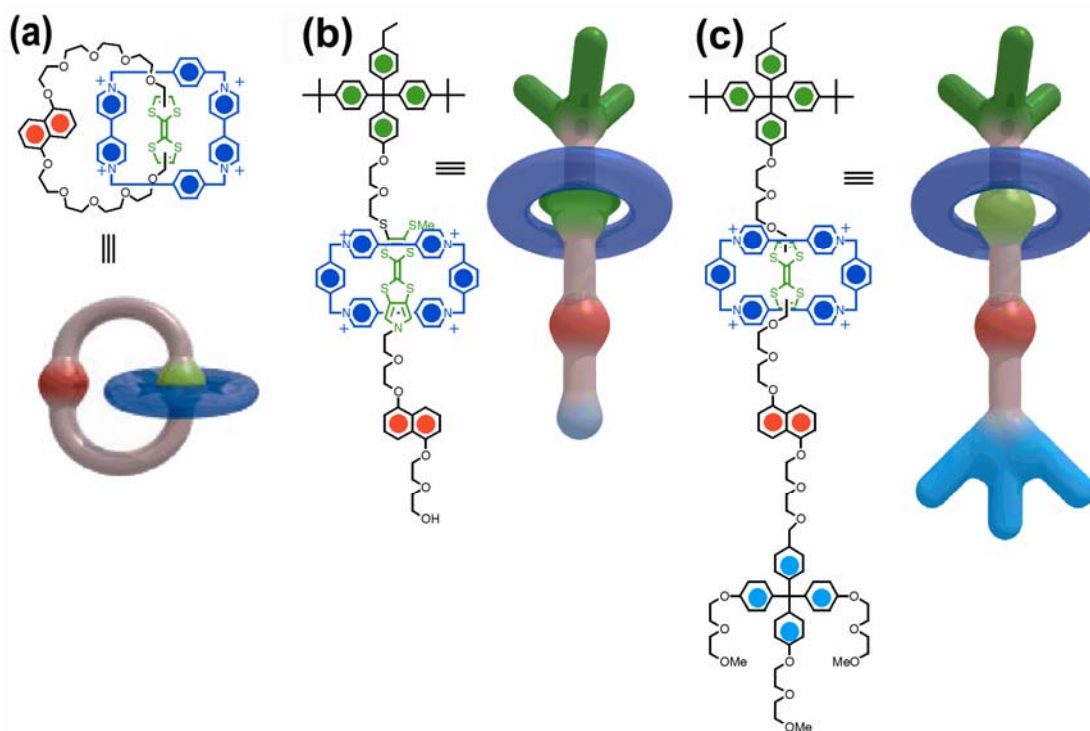


**Figure 1-4.** Bistable molecular mechanical switching molecules, each with similar recognition groups. (a) A [2]catenane, which is a molecular structure consisting of two

interlocked rings. A crown ether ring containing tetrathiafulvalene (TTF) and dioxynaphthalene (DNP) recognition units are threaded through a tetracationic cyclobisparaquat (CBPQT<sup>4+</sup>) ring. (b) A pseudorotaxane containing a modified TTF unit, a DNP group on a thread component, and a CBPQT<sup>4+</sup> ring encircling the modified TTF unit. (c) A [2]rotaxane amphiphile, containing TTF and DNP units on a dumbbell component and a CBPQT<sup>4+</sup> ring. For each of these molecules, the lowest energy structure is shown (CBPQT<sup>4+</sup> ring) encircling the (modified)TTF unit. Many variations on these themes are possible, including molecular switches with modified recognition units, different ends on the dumbbell or thread components (for the [2]rotaxane and pseudorotaxane structures, respectively) for attaching the molecules to different surfaces, etc.

The advantage of these switching molecules is that they can be switched precisely by applying appropriate redox stimuli between two conformations (figure 1-5a). These two conformations are separated by an energy barrier. While an equilibrium exists between the two co-conformers, that equilibrium is typically shifted towards one (the ground-state co-conformation, or GSCC) and away from the other (the metastable-state co-conformation, or MSCC). One example is the bistable [2]rotaxane shown in figure 1-5a. In figure 1-5a, the CBPQT<sup>4+</sup> ring encircles a tetrathiafulvalene (TTF) unit on a dumbbell-shaped component, which represents the GSCC. The MSCC is the structure in which the CBPQT<sup>4+</sup> ring encircles the dioxynaphthalene (DNP) unit. For this and related other molecules, a GSCC dominated distribution is switched to an MSCC dominated distribution via oxidation of the TTF unit (TTF → TTF<sup>+</sup>). The detailed switching cycle is shown in figure 1-5b.

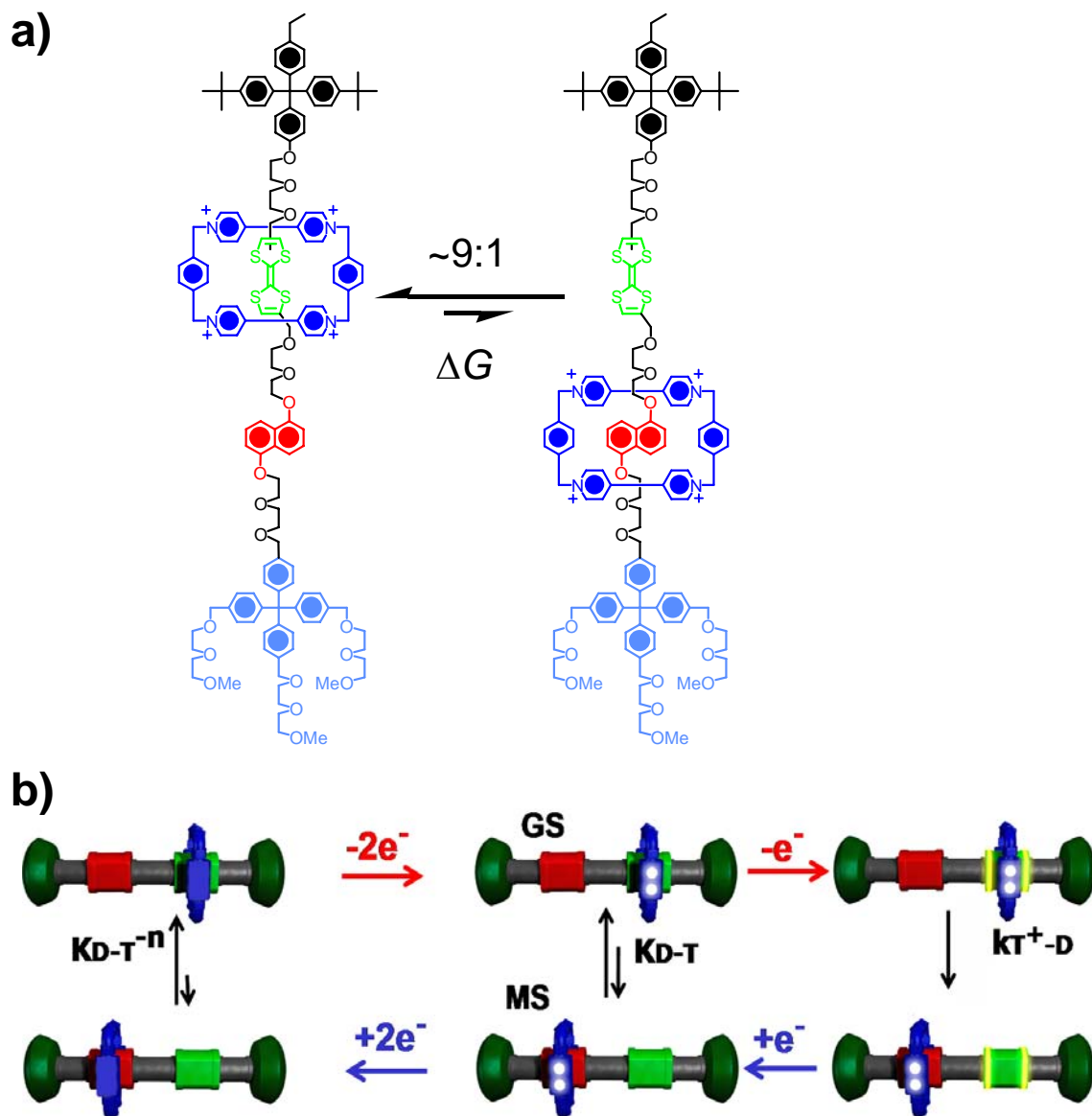


**Figure 1-5.** Molecular switching of bistable [2]rotaxanes. (a) Structural formulas of the two translational isomers of the representative bistable rotaxane corresponding to the ground state co-conformation (GSCC) and the metastable state co-conformation (MSCC). (b) The switching cycle for bistable [2]rotaxanes. The green and red sites on the dumbbell components correspond to tetrathiafulvalene (TTF) and dioxynaphthyl (DNP) units, respectively. When the TTF unit is oxidized, it is drawn with highlighted green. The blue ring corresponds to the  $\text{CBPQT}^{4+}$  ring carrying the positive charges indicated as

white spots. Reproduced with permission from reference 12. Copyright 2004 Wiley-VCH Verlag GmbH.

For the past several years, major efforts in my research group have been dedicated towards validate the switching mechanism especially as it applies to molecular electronic devices. The validation of the switching mechanism has been pursued in two directions. First, a number of these switching molecules have been tested in different physical environments including molecular switch tunnel junction (MSTJ) devices. Second, several [2]rotaxanes with different recognition units have been investigated in those physical environments. The overall objective has been to take fundamental molecular properties - the thermodynamic and kinetic parameters that describe the bistable switching mechanism - and attempt to understand how those properties are influenced by physical environment, including the environment of a molecular switch tunnel junction

Studies in different physical environments have demonstrated that this overall switching cycle is universal. However,  $k_{D \rightarrow T}$ , a recovery rate from the MSCC to the GSCC-dominating equilibrium, exhibits a strong environmental dependence. As one moves from acetonitrile solution (79) to (high viscosity) polymer gels (12) to SAMs on Au surfaces (69) to a highly compressed LB monolayer sandwiched within an MSTJ(1, 4, 80-82), thermal decay corresponding to  $k_{D \rightarrow T}$  in figure 1-5b is decreased by as much as  $10^4$ - $10^5$ .

The influence of the molecular structure on the ground-state equilibrium was also investigated in various environments (80). Two different [2]rotaxanes were tested: the [2]rotaxane shown in figure 1-5a and a rotaxane in which the TTF unit was replaced by a  $\pi$ -extended analogue (a bispyrrolotetrathiafulvalene, or BPTTF) (83). In contrast to the MSCC  $\rightarrow$  GSCC relaxation kinetics, the thermodynamic equilibrium was found to be

relatively independent of environment, depending almost solely on molecular structure. In all environments, the TTF-based [2]rotaxane maintained a constant value ( $\sim 9/1$ ) of GSCC/MSCC equilibrium ( $K_{(D/T)^{4+}}$ ) over broad range of temperatures, whereas BPTTF-based [2]rotaxane exhibited a strongly temperature-dependent GSCC/MSCC ( $1/1\sim 3/1$ ) over even smaller temperature range.

These studies in different environments not only validate the proposed switching mechanism, but provide evidence that one of the key device properties such as On/Off ratio is reflective of the molecular structure.

## **1.8 Scale-down: 160 kbit Molecular Electronic Memory Circuits**

One of the major advantages of molecular electronics is a potential scaling of devices to molecular dimensions. In other words, until patterning techniques defining electrodes in the molecular dimensions are developed, the efforts to understand molecular electronics and how it might be applied to ultra-small devices would be academic.

For these reasons, my research group has developed a technique for the preparation of ultra-dense nanowire arrays, called the superlattice nanowire pattern transfer (SNAP) method. At the same time, through our collaboration with the Stoddart group, a variety of [2]rotaxanes have been developed and found to maintain somewhat robust switching characteristics within the MSTJs. Finally, ultra-dense molecular electronic crossbar circuits (84) were achieved by integrating the SNAP nanowires with optimized functional [2]rotaxanes (85). These memory circuits represent a world-record in terms of the bit density per unit area of an electronically addressable memory. They

were demonstrated to be capable of storing information and to function as complete circuits.

Consequently, the successful demonstration of these delicate circuits indicates that new materials and architectures based on nanotechnology could provide solutions to scale-down issues that have been very difficult to address with the current CMOS technology.

## **1.9 Nanofluidics**

Owing to recent advances in fabrication technology, one could routinely generate nanostructures such as nanopores, nanowires and nanotubes. In particular, the capability of controlling geometry in one dimensional nanostructures has opened up a new field, nanofluidics.

The most noticeable character of the nanofluidics, compared to microfluidics, is small channel dimensions that are comparable to the size of macromolecules and are also comparable to the length scales associated with surface-charge Debye screening. The small channel dimensions bring many novel scientific phenomena as well as useful findings for applications. Entangled molecules could be stretched out along one dimension. This allow for specific chemical sites that are not readily accessible within the entangled molecule to be interrogated. A good example is the restriction mapping for DNA molecules(86). Also, the target molecules delivered to the nanochannel experience electrostatic interactions with the nanochannel walls because at least one dimension of the channel dimensions might be on the order of the Debye screening length. Under this condition, ionic transport would be dominated by the nanochannel surface charges and

charges carried by the ions(87, 88). This extraordinary feature can be utilized for biosensors(89). Moreover, extremely fast fluid flow is possible because no-slip condition may not hold true in several nanometer channel diameters(90-92).

## **1.10 Structure and Scope of the Thesis**

The thesis is composed of four chapters. Each chapter has its own introduction, figures and references. Chapter 2 covers the kinetic and thermodynamic studies for bistable [2]rotaxanes. These studies were critical for validating the switching mechanism for [2]rotaxanes and [2]catenanes that had been previously proposed for their operation within molecular switch tunnel junction devices. Thus, all the claims and descriptions in chapter 2 now provide a foundation for the further understanding and development of these molecules within solid-state device settings. Chapter 3 is dedicated to the project of fabricating and testing the 160 kbit molecular electronic memory circuits. Completion of this project represented a long term goal of my research group - the production of fully functional molecular electronic memory devices at true molecular dimensions. This project required the development of non-trivial nanofabrication processes, and certain of those are presented in some detail. This chapter is also related to the results of chapter 2, since the successful demonstration of the operation of this memory circuit relies on the mechanistic models for the switching molecules that are covered in chapter 2. Chapter 4 covers the nanofluidics project. This project was initiated in the summer of 2006 and thus is currently in the early development stage, although there has been a significant progress. Future directions for this project are also described.

## 1.11 References

1. Collier, C. P., Mattersteig, G., Wong, E. W., Luo, Y., Beverly, K., Sampaio, J., Raymo, F. M., Stoddart, J. F. & Heath, J. R. (2000) *Science* 289, 1172-1175.
2. Pease, A. R., Jeppesen, J. O., Stoddart, J. F., Luo, Y., Collier, C. P. & Heath, J. R. (2001) *Acc. Chem. Res.* 34, 433-444.
3. Sheeney-Haj-Ichia, L. & Willner, I. (2002) *J. Phys. Chem. B* 106, 13094-13097.
4. Luo, Y., Collier, C. P., Jeppesen, J. O., Nielsen, K. A., Delonno, E., Ho, G., Perkins, J., Tseng, H. R., Yamamoto, T., Stoddart, J. F. & Heath, J. R. (2002) *Chemphyschem* 3, 519-525.
5. Katz, E., Sheeney-Haj-Ichia, L. & Willner, I. (2004) *Angew. Chem. Int. Ed.* 43, 3292-3300.
6. Hernandez, R., Tseng, H. R., Wong, J. W., Stoddart, J. F. & Zink, J. I. (2004) *J. Am. Chem. Soc.* 126, 3370-3371.
7. Kim, K., Jeon, W. S., Kang, J. K., Lee, J. W., Jon, S. Y., Kim, T. & Kim, K. (2003) *Angew. Chem. Int. Ed.* 42, 2293-2296.
8. Jimenez, M. C., Dietrich-Buchecker, C. & Sauvage, J. P. (2000) *Angew. Chem. Int. Ed.* 39, 3284-3287.
9. Jimenez-Molero, M. C., Dietrich-Buchecker, C. & Sauvage, J. P. (2003) *Chem. Com.*, 1613-1616.
10. Marsella, M. J. & Reid, R. J. (1999) *Macromolecules* 32, 5982-5984.
11. Taylor, E. W. (1993) *Science* 261, 35-36.

12. Steuerman, D. W., Tseng, H. R., Peters, A. J., Flood, A. H., Jeppesen, J. O., Nielsen, K. A., Stoddart, J. F. & Heath, J. R. (2004) *Angew. Chem. Int. Ed.* 43, 6486-6491.
13. Grave, C., Tran, E., Samori, P., Whitesides, G. M. & Rampi, M. A. (2004) *Synthetic Metals* 147, 11-18.
14. Slowinski, K., Fong, H. K. Y. & Majda, M. (1999) *J. Am. Chem. Soc.* 121, 7257-7261.
15. Tran, E., Rampi, M. A. & Whitesides, G. M. (2004) *Angew. Chem. Int. Ed.* 43, 3835-3839.
16. York, R. L. & Slowinski, K. (2003) *J. Electroanal. Chem.* 550, 327-336.
17. Konstadinidis, K., Zhang, P., Opila, R. L. & Allara, D. L. (1995) *Surface Science* 338, 300-312.
18. Chang, S. C., Li, Z. Y., Lau, C. N., Larade, B. & Williams, R. S. (2003) *Appl. Phys. Lett.* 83, 3198-3200.
19. Fisher, G. L., Hooper, A. E., Opila, R. L., Allara, D. L. & Winograd, N. (2000) *J. Phys. Chem. B* 104, 3267-3273.
20. Hooper, A., Fisher, G. L., Konstadinidis, K., Jung, D., Nguyen, H., Opila, R., Collins, R. W., Winograd, N. & Allara, D. L. (1999) *J. Am. Chem. Soc.* 121, 8052-8064.
21. Nowak, A. M. & McCreery, R. L. (2004) *Anal. Chem.* 76, 1089-1097.
22. Tighe, T. B., Daniel, T. A., Zhu, Z. H., Uppili, S., Winograd, N. & Allara, D. L. (2005) *J. Phys. Chem. B* 109, 21006-21014.

23. Walker, A. V., Tighe, T. B., Cabarcos, O. M., Reinard, M. D., Haynie, B. C., Uppili, S., Winograd, N. & Allara, D. L. (2004) *J. Am. Chem. Soc.* 126, 3954-3963.
24. Walker, A. V., Tighe, T. B., Stapleton, J., Haynie, B. C., Upilli, S., Allara, D. L. & Winograd, N. (2004) *Appl. Phys. Lett.* 84, 4008-4010.
25. de Boer, B., Frank, M. M., Chabal, Y. J., Jiang, W. R., Garfunkel, E. & Bao, Z. (2004) *Langmuir* 20, 1539-1542.
26. McGovern, W. R., Anariba, F. & McCreery, R. L. (2005) *J. Electrochem. Soc.* 152, E176-E183.
27. Liang, W. J., Shores, M. P., Bockrath, M., Long, J. R. & Park, H. (2002) *Nature* 417, 725-729.
28. Park, H., Lim, A. K. L., Alivisatos, A. P., Park, J. & McEuen, P. L. (1999) *Appl. Phys. Lett.* 75, 301-303.
29. Park, H., Park, J., Lim, A. K. L., Anderson, E. H., Alivisatos, A. P. & McEuen, P. L. (2000) *Nature* 407, 57-60.
30. Park, J., Pasupathy, A. N., Goldsmith, J. I., Chang, C., Yaish, Y., Petta, J. R., Rinkoski, M., Sethna, J. P., Abruna, H. D., McEuen, P. L. & Ralph, D. C. (2002) *Nature* 417, 722-725.
31. Reed, M. A., Zhou, C., Muller, C. J., Burgin, T. P. & Tour, J. M. (1997) *Science* 278, 252-254.
32. Reichert, J., Ochs, R., Beckmann, D., Weber, H. B., Mayor, M. & von Lohneysen, H. (2002) *Phys. Rev. Lett.* 88.
33. Xu, B. Q. & Tao, N. J. J. (2003) *Science* 301, 1221-1223.

34. Yaliraki, S. N. & Ratner, M. A. (1998) *J. Chem. Phys.* 109, 5036-5043.
35. Yu, H. B., Luo, Y., Beverly, K., Stoddart, J. F., Tseng, H. R. & Heath, J. R. (2003) *Angew. Chem. Int. Ed.* 42, 5706-5711.
36. Nowak, A. M. & McCreery, R. L. (2004) *J. Am. Chem. Soc.* 126, 16621-16631.
37. DeIonno, E., Tseng, H. R., Harvey, D. D., Stoddart, J. F. & Heath, J. R. (2006) *J. Phys. Chem. B* 110, 7609-7612.
38. Stewart, D. R., Ohlberg, D. A. A., Beck, P. A., Chen, Y., Williams, R. S., Jeppesen, J. O., Nielsen, K. A. & Stoddart, J. F. (2004) *Nano Lett.* 4, 133-136.
39. Cao, P. G., Yu, H. B. & Heath, J. R. (2006) *J. Phys. Chem. B* 110, 23615-23618.
40. Guisinger, N. P., Basu, R., Greene, M. E., Baluch, A. S. & Hersam, M. C. (2004) *Nanotechnology* 15, S452-S458.
41. Guisinger, N. P., Greene, M. E., Basu, R., Baluch, A. S. & Hersam, M. C. (2004) *Nano Lett.* 4, 55-59.
42. Guisinger, N. P., Yoder, N. L. & Hersam, M. C. (2005) *Proc. Nat. Acad. Sci.* 102, 8838-8843.
43. Yu, H. B., Webb, L. J., Ries, R. S., Solares, S. D., Goddard, W. A., Heath, J. R. & Lewis, N. S. (2005) *J. Phys. Chem. B* 109, 671-674.
44. Yu, H. B., Webb, L. J., Solares, S. D., Cao, P. G., Goddard, W. A., Heath, J. R. & Lewis, N. S. (2006) *J. Phys. Chem. B* 110, 23898-23903.
45. Bansal, A., Li, X. L., Lauermaun, I., Lewis, N. S., Yi, S. I. & Weinberg, W. H. (1996) *J. Am. Chem. Soc.* 118, 7225-7226.
46. Royea, W. J., Michalak, D. J. & Lewis, N. S. (2000) *Appl. Phys. Lett.* 77, 2566-2568.

47. Lenfant, S., Krzeminski, C., Delerue, C., Allan, G. & Vuillaume, D. (2003) *Nano Lett.* 3, 741-746.
48. Mayne, A. J., Lastapis, M., Baffou, G., Soukiassian, L., Comtet, G., Hellner, L. & Dujardin, G. (2004) *Phys. Rev. B* 69, 045409.
49. Basu, R., Tovar, J. D. & Hersam, M. C. (2005) *J. Vac. Sci. & Tech. B* 23, 1785-1789.
50. Aviram, A. & Ratner, M. A. (1974) *Chem. Phys. Lett.* 29, 277-283.
51. Ashwell, G. J., Chwialkowska, A. & High, L. R. H. (2004) *J. Mat. Chem.* 14, 2848-2851.
52. Ashwell, G. J., Ewington, J. & Moczko, K. (2005) *J. Mat. Chem.* 15, 1154-1159.
53. Ashwell, G. J. & Gandolfo, D. S. (2002) *J. Mat. Chem.* 12, 411-415.
54. Ashwell, G. J., Gandolfo, D. S. & Hamilton, R. (2002) *J. Mat. Chem.* 12, 416-420.
55. Ashwell, G. J., Hamilton, R. & High, L. R. H. (2003) *J. Mat. Chem.* 13, 1501-1503.
56. Ashwell, G. J., Mohib, A. & Miller, J. R. (2005) *J. Mat. Chem.* 15, 1160-1166.
57. Ashwell, G. J., Sambles, J. R., Martin, A. S., Parker, W. G. & Szablewski, M. (1990) *J. Chem. Soc. Comm.*, 1374-1376.
58. Ashwell, G. J., Tyrrell, W. D. & Whittam, A. J. (2003) *J. Mat. Chem.* 13, 2855-2857.
59. Ho, G., Heath, J. R., Kondratenko, M., Perepichka, D. F., Arseneault, K., Pezolet, M. & Bryce, M. R. (2005) *Chem. Eur. J.* 11, 2914-2922.
60. McCreery, R. L. (2004) *Chem. Mater.* 16, 4477-4496
61. Metzger, R. M. (2003) *Chem. Rev.* 103, 3803-3834.

62. Metzger, R. M., Baldwin, J. W., Shumate, W. J., Peterson, I. R., Mani, P., Mankey, G. J., Morris, T., Szulczewski, G., Bosi, S., Prato, M., Comito, A. & Rubin, Y. (2003) *J. Phys. Chem. B* 107, 1021-1027.
63. Ashwell, G. J., Urasinska, B. & Tyrrell, W. D. (2006) *Phys. Chem. Chem. Phys.* 8, 3314-3319.
64. McCreery, R., Dieringer, J., Solak, A. O., Snyder, B., Nowak, A. M., McGovern, W. R. & DuVall, S. (2003) *J. Am. Chem. Soc.* 125, 10748-10758.
65. Taylor, J., Brandbyge, M. & Stokbro, K. (2002) *Phys. Rev. Lett.* 89.
66. Asakawa, M., Higuchi, M., Mattersteig, G., Nakamura, T., Pease, A. R., Raymo, F. M., Shimizu, T. & Stoddart, J. F. (2000) *Adv. Mat.* 12, 1099-1102.
67. Ashton, P. R., Horn, T., Menzer, S., Preece, J. A., Spencer, N., Stoddart, J. F. & Williams, D. J. (1997) *Synthesis-Stuttgart*, 480-488.
68. Brown, C. L., Jonas, U., Preece, J. A., Ringsdorf, H., Seitz, M. & Stoddart, J. F. (2000) *Langmuir* 16, 1924-1930.
69. Tseng, H. R., Wu, D. M., Fang, N. X. L., Zhang, X. & Stoddart, J. F. (2004) *Chemphyschem* 5, 111-116.
70. Lu, T. B., Zhang, L., Gokel, G. W. & Kaifer, A. E. (1993) *J. Am. Chem. Soc.* 115, 2542-2543.
71. Asakawa, M., Ashton, P. R., Balzani, V., Brown, C. L., Credi, A., Matthews, O. A., Newton, S. P., Raymo, F. M., Shipway, A. N., Spencer, N., Quick, A., Stoddart, J. F., White, A. J. P. & Williams, D. J. (1999) *Chem. Eur. J.* 5, 860-875.
72. Saha, S., Johansson, E., Flood, A. H., Tseng, H. R., Zink, J. I. & Stoddart, J. F. (2005) *Chem. Eur. J.* 11, 6846-6858.

73. Chia, S. Y., Cao, J. G., Stoddart, J. F. & Zink, J. I. (2001) *Angew. Chem. Int. Ed.* 40, 2447-2451.
74. Katz, E., Baron, R., Willner, I., Richke, N. & Levine, R. D. (2005) *Chemphyschem* 6, 2179-21789.
75. Katz, E., Lioubashevsky, O. & Willner, I. (2004) *J. Am. Chem. Soc.* 126, 15520-15532.
76. Long, B., Nikitin, K. & Fitzmaurice, D. (2003) *J. Am. Chem. Soc.* 125, 5152-5160.
77. Long, B., Nikitin, K. & Fitzmaurice, D. (2003) *J. Am. Chem. Soc.* 125, 15490-15498.
78. Nikitin, K. & Fitzmaurice, D. (2005) *J. Am. Chem. Soc.* 127, 8067-8076.
79. Flood, A. H., Peters, A. J., Vignon, S. A., Steuerman, D. W., Tseng, H. R., Kang, S., Heath, J. R. & Stoddart, J. F. (2004) *Chem. Eur. J.* 10, 6558-6564.
80. Choi, J. W., Flood, A. H., Steuerman, D. W., Nygaard, S., Braunschweig, A. B., Moonen, N. N. P., Laursen, B. W., Luo, Y., DeIonno, E., Peters, A. J., Jeppesen, J. O., Xu, K., Stoddart, J. F. & Heath, J. R. (2006) *Chem. Eur. J.* 12, 261-279.
81. Collier, C. P., Jeppesen, J. O., Luo, Y., Perkins, J., Wong, E. W., Heath, J. R. & Stoddart, J. F. (2001) *J. Am. Chem. Soc.* 123, 12632-12641.
82. Diehl, M. R., Steuerman, D. W., Tseng, H. R., Vignon, S. A., Star, A., Celestre, P. C., Stoddart, J. F. & Heath, J. R. (2003) *Chemphyschem* 4, 1335-1339.
83. Laursen, B. W., Nygaard, S., Jeppesen, J. O. & Stoddart, J. F. (2004) *Org. Lett.* 6, 4167-4170.

84. Green, J. E., Choi, J. W., Boukai, A., Bunimovich, Y., Johnston-Halperin, E., DeLonno, E., Luo, Y., Sheriff, B. A., Xu, K., Shin, Y. S., Tseng, H. R., Stoddart, J. F. & Heath, J. R. (2007) *Nature* 445, 414-417.
85. Tseng, H. R., Vignon, S. A., Celestre, P. C., Perkins, J., Jeppesen, J. O., Di Fabio, A., Ballardini, R., Gandolfi, M. T., Venturi, M., Balzani, V. & Stoddart, J. F. (2004) *Chem. Eur. J.* 10, 155-172.
86. Riehn, R., Lu, M. C., Wang, Y. M., Lim, S. F., Cox, E. C. & Austin, R. H. (2005) *Proc. Nat. Acad. Sci.* 102, 10012-10016.
87. Karnik, R., Fan, R., Yue, M., Li, D. Y., Yang, P. D. & Majumdar, A. (2005) *Nano Lett.* 5, 943-948.
88. Stein, D., Kruithof, M. & Dekker, C. (2004) *Phys. Rev. Lett.* 93, 035901.
89. Karnik, R., Castelino, K., Fan, R., Yang, P. & Majumdar, A. (2005) *Nano Lett.* 5, 1638-1642.
90. Hinds, B. J., Chopra, N., Rantell, T., Andrew, R., Gavalas, V. & Bachas, L. G. (2005) *Science* 303, 62-65.
91. Holt, J. K., Park, H. K., Wang, Y., Stadermann, M., Artyukhin, A. B., Grigoropoulos, S. P., Noy, A. & Bakajin, O. (2006) *Science* 312, 1034-1037.
92. Majumdar, M., Chopra, N., Andrew, R. & Hinds, B. J. (2005) *Nature* 438, 44-44.

## Chapter 2

### Ground State Equilibrium Thermodynamics and Switching Kinetics of Bistable [2]Rotaxane Switched in Solution, Polymer Gels, and Molecular Electronic Devices

#### 2.1 Introduction

One of the goals (1-3) of the field of molecular electronics is to be able to control the properties of molecular-based solid-state devices through chemical design and synthesis. Such control has been demonstrated (4-15) for passive devices, the simplest of which are molecular tunnel junction resistors consisting of a molecular monolayer, often a functionalized alkane, sandwiched between two conductors. Several groups have shown that the tunnel current varies exponentially with chain length (10, 12), although they have also found that atomistic details (4, 5, 7, 8, 14), such as the packing of the chains, the molecular alignment within the monolayer, and the nature of the electrodes (6, 9, 13), are all important.

Molecular rectifiers, typically represented by an electron donor-bridge-acceptor molecule extended between two electrodes (16), represent a more sophisticated passive device. Demonstrations of molecular control over current rectification have required a substantial effort by a number of groups (16-32), and have only been achieved within the past few years. Details such as the nature of the

molecule/electrode interface, the donor and acceptor molecular orbital energies, and the structure of the molecule within the device – i.e., the extension of the donor-bridge-acceptor between the two electrodes – are all important since rectification can arise from many areas within a junction (16-32).

Active molecular electronic (33) devices (switches) represent a significant jump in terms of molecular complexity. My research group has used electrochemically switchable, donor-acceptor, bistable [2]catenane and [2]rotaxane molecules within molecular switch tunnel junctions (MSTJs) (34-36). As in the case of the molecular tunnel junction resistors and rectifiers, MSTJs also represent a highly coupled molecule/electrode system (6, 9, 13, 37, 38). However, for the bistable [2]catenane and [2]rotaxane switches, there are a number of experimental parameters that can be measured to correlate molecular structure and solution-phase switching behavior with molecular electronic device switching properties. These parameters include colorimetric changes (39), shifts in electrochemical potentials (40, 41), and temperature dependent kinetics (39-41) for the cycling of the switch.

As an example, consider the redox-switchable [2]rotaxane **RATTF**<sup>4+</sup> illustrated in figure 2-1a. This bistable [2]rotaxane is composed of electron-accepting cyclobis(paraquat-*p*-phenylene) (CBPQT<sup>4+</sup>) ring (blue) that encircles either a tetrathiafulvalene (TTF) unit (green) or a 1,5-dioxynaphthalene (DNP) unit (red), both

electron-donating systems. This mechanically-interlocked molecular compound and other closely related bistable rotaxanes (10, 40, 42-47) as well as rotaxanes constructed from different donor-acceptor units (48-50) and from hydrogen-bonded systems (51-54) and transition metal templates (55-58), have been investigated in depth previously.

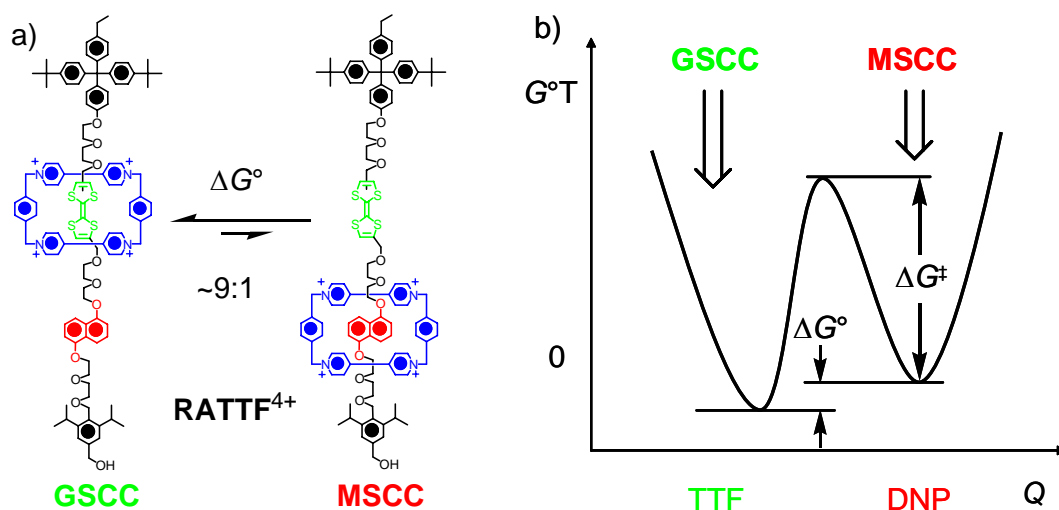


**Figure 2-1.** Molecular structure and potential energy surface of bistable [2]rotaxane. (a) Structural formulas of the two translational isomers of the bistable rotaxane **RATTF**<sup>4+</sup> corresponding to the ground state co-conformation (GSCC) and the metastable state co-conformation (MSCC). (b) Potential energy surface for the bistable **RATTF**<sup>4+</sup> where the energy wells correspond to the GSCC and MSCC. The free energy difference  $\Delta G^\circ$ , between the wells and the free energy barrier to relaxation,  $\Delta G^\ddagger$ , from the MSCC to the GSCC are defined against a normal coordinate,  $Q$ , representing translation of the ring along the dumbbell component of the [2]rotaxane.

Under ambient conditions in acetonitrile solution, the CBPQT<sup>4+</sup> ring in **RATTF**<sup>4+</sup> encircles the TTF unit preferentially (>90%) with respect to the DNP unit. This equilibrium is described by the  $\Delta G^\circ_{298}$  change shown in figure 2-1b where  $\Delta G^\circ = +1.6$  kcal/mol when the CBPQT<sup>4+</sup> ring moves from the TTF to the DNP unit. Hence, the co-conformation (CC) with the CBPQT<sup>4+</sup> ring encircling the TTF is unit is referred to as the ground state co-conformation (GSCC). The first two oxidation states of **RATTF**<sup>4+</sup> correspond to the  $\text{TTF}^0 \rightarrow \text{TTF}^{*+} \rightarrow \text{TTF}^{2+}$  processes. Upon formation of  $\text{TTF}^{*+}$  cation radical, the Coulombic repulsion between the CBPQT<sup>4+</sup> ring and the  $\text{TTF}^{*+}$  results in translation of the ring to the DNP unit. This process is fast and is believed to convert all of the GSCC into the MSCC. Although the Coulombic-driven switching movement of the CBPQT<sup>4+</sup> ring has not been measured, I estimate that the barrier corresponding to the mono- and di-cation  $\text{TTF}^{2+/+}$  would be at least  $\sim 3$  and  $\sim 6$  kcal/mol less than the 16 kcal/mol barrier observed for the free energy barrier between the MSCC and GSCC leading to room temperature time constants of  $t \sim 500$  and 3 ms, respectively. By the same reasoning, for the  $\text{TTF}^{2+}$  dication, the movement of the CBPQT<sup>4+</sup> ring to results. When the  $\text{TTF}^{*+}$  cation radical is reduced back to  $\text{TTF}^0$ , the CBPQT<sup>4+</sup> ring remains around the DNP unit for a period of time. This translational isomer of the GSCC is the metastable state co-conformation (MSCC). Recovery of the MSCC/GSCC equilibrium distribution ( $\sim 1:9$ ) is an activated process.

This switching cycle can be detected by a number of experimental observations. First, the lowest oxidation potential (corresponding to  $\text{TTF}^0 \rightarrow \text{TTF}^{*+}$ ) of the GSCC is +490 mV, while that for the MSCC is +310 mV. (All potentials referenced to an Ag/AgCl electrode.) Second, the colors of GSCC- and MSCC-dominated solutions are green and red, respectively. Thus, electrochemistry and spectroscopy can be employed to quantify the MSCC/GSCC ratio in such a bistable rotaxane at any given time. Third, the (activated) relaxation of an MSCC- back to a GSCC-dominated distribution is temperature dependent and so the kinetic parameters may be quantified through time- and temperature-dependent measurements. For example, the  $\Delta G_{298}^{\ddagger}$  for this process in the case (40) of **RATTF**<sup>4+</sup> in the solution phase is 16.2 ( $\pm$  0.3) kcal/mol.

My research group has reported on the MSCC  $\rightarrow$  GSCC relaxation kinetics for a number of bistable [2]catenanes and [2]rotaxanes in several different environments, including (i) in acetonitrile solution (40), (ii) in monolayers ([2]rotaxanes only) bonded to the surfaces of Au working electrodes (41), and (iii) in solid-state polymer electrolytes (39). In the case of the acetonitrile solution and the polymer electrolyte devices, My research group has demonstrated (39, 40) that the relaxation kinetics were sensitive to both molecular structure and physical environment, although the overall switching mechanism remains the same. I extended these measurements to

include MSTJ devices, as well as establishing the ground-state equilibrium thermodynamics. Three bistable [2]rotaxanes – namely **RATTF**<sup>4+</sup>, **RTTF**<sup>4+</sup> and **RBPTTF**<sup>4+</sup> – plus the control (59) [2]rotaxane **RBLOCK**<sup>4+</sup> were investigated.

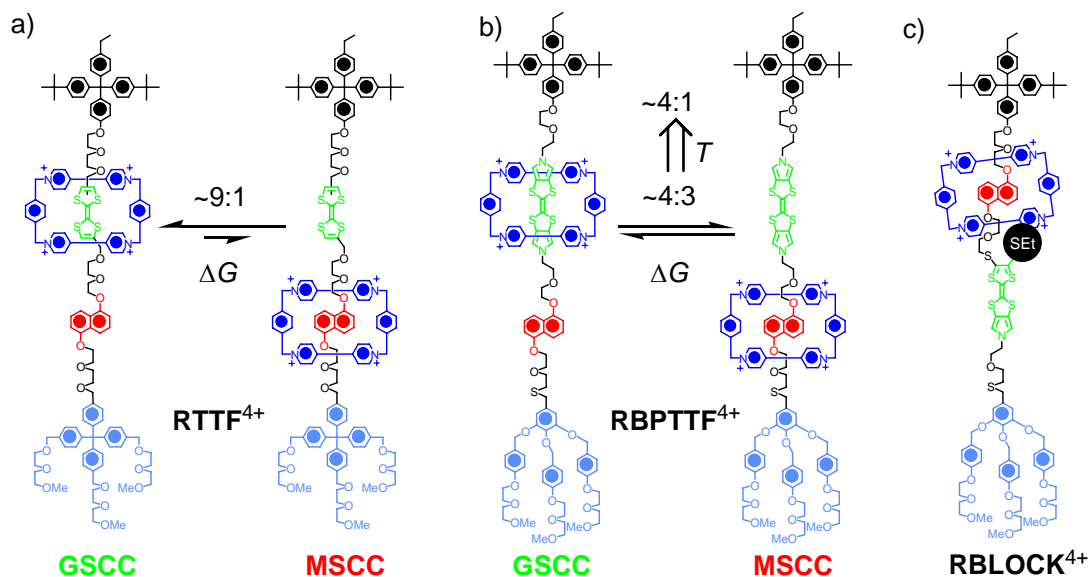


**Figure 2-2.** Structural formulas of the translational isomers of the bistable rotaxanes (a) **RTTF**<sup>4+</sup> and (b) **RBPTTF**<sup>4+</sup> both in their GSCC and MSCC. (c) Structural formula of the sterically-blocked (SEt) [2]rotaxane **RBLOCK**<sup>4+</sup> used in control studies.

It is evident from inspection of the structural formulas of these three [2]rotaxanes shown in figures 2-1 and 2-2 that **RATTF**<sup>4+</sup>, **RTTF**<sup>4+</sup> and **RBPTTF**<sup>4+</sup> can exist at equilibrium as two translational isomers (or co-conformations). By contrast, **RBLOCK**<sup>4+</sup> has the CBPQT<sup>4+</sup> ring located exclusively around the DNP unit as a result of the presence of the bulky SEt group on the monopyrrolotetrathiafulvalene

unit acting as an effective steric barrier, thus preventing translational isomerism. The critical difference in the molecular structures between the **RATTF**<sup>4+</sup> and **RTTF**<sup>4+</sup> pair and the **RBPTTF**<sup>4+</sup> lies with the replacement of the simple TTF unit for the bispyrrolotetrathiafulvalene (BPTTF) unit (60). However, all three bistable rotaxanes have slightly different stoppers – **RATTF**<sup>4+</sup> bears a substituted benzylic alcohol function and both **RTTF**<sup>4+</sup> and **RBPTTF**<sup>4+</sup> have slightly different hydrophilic stoppers facilitating their incorporation into MSTJ devices. The major difference in the switching properties between these bistable rotaxanes is that the equilibrium MSCC/GSCC ratio (~1:9) for **RATTF**<sup>4+</sup> and **RTTF**<sup>4+</sup> is relatively temperature independent while the equilibrium MSCC/GSCC ratio (~1:4 at 298 K) for **RBPTTF**<sup>4+</sup> exhibits a strong temperature dependence. These thermodynamic differences will be rationalized in the following subchapter by reference to binding constants obtained by isothermal titration calorimetry (ITC) for the complexation of model guests containing TTF, BPTTF and DNP units, by the **CBPQT**<sup>4+</sup> host in acetonitrile solution at 298 K.

Previously my research group has hypothesized (34-37, 39, 40) that the GSCC corresponds to the low-conductance (switch-open) state of an MSTJ, while the MSCC corresponds to the high-conductance (switch-closed) state. This hypothesis is consistent with many observations, including the shift in the oxidation potential of the

TTF group that correlates with the switching from the GSCC to the MSCC structure. In addition, Goddard's group (61, 62) has found by computational methods that the MSCC structure has extended electron delocalization – and thus enhanced conductivity – in comparison with the GSCC.

The switching kinetics of **RATTF**<sup>4+</sup>, **RTTF**<sup>4+</sup> and **RBPTTF**<sup>4+</sup> should be relatively similar. By contrast, the ground-state thermodynamics – and hence the temperature-dependence of the switching amplitude – should be quite different. In this study, I employed temperature dependent electrochemical and current-voltage measurements to correlate *qualitatively* the thermodynamic properties of **RATTF**<sup>4+</sup> in (i) acetonitrile solution, and (ii) solid-state polymer electrolytes, and of **RTTF**<sup>4+</sup> in (iii) MSTJs together with **RBPTTF**<sup>4+</sup> across all three environments. I also correlated *quantitatively* the MSCC → GSCC relaxation kinetics in these three different physical environments. I find that the ground-state thermodynamic differences between the pair of TTF-containing rotaxanes (**RATTF**<sup>4+</sup> and **RTTF**<sup>4+</sup>) and **RBPTTF**<sup>4+</sup> are relatively independent of physical environment, but strongly influenced by molecular structure. I also find that, although the MSCC → GSCC relaxation kinetics exhibit a strong environmental dependence in the case of all three rotaxanes, the switching mechanism appears to be similar for all three compounds, and is robust and consistent in all three environments. These findings allow me to refine our initial hypothesis

such that the high-conductance (switch-closed) state of an MSTJ still corresponds to the MSCC but that the low-conductance (switch-open) state is now related to the MSCC/GSCC ratio at equilibrium. These experiments provide a proof-of-principle for the control of molecular structure over a key device characteristic – temperature-dependent switching amplitudes in molecular electronic devices.

## 2.2 Molecular Design

Although the bistable [2]rotaxanes **RATTF**<sup>4+</sup>, **RTTF**<sup>4+</sup> and **RBPTTF**<sup>4+</sup> all contain DNP sites, they differ in the first two contain a TTF unit and the third a BPTTF. In order to understand how these units influence the switching in these bistable rotaxanes, a series of model guests were investigated for their binding with the **CBPQT**<sup>4+</sup> host – as its tetrakis(hexafluorophosphate) salt – using ITC.



of magnitude. By contrast, the binding of **BPTTF** by the **CBPQT**<sup>4+</sup> host is already quite high and only doubles.

**Table 2-1.** Thermodynamic binding data<sup>[a]</sup> corresponding to the complexation between **CBPQT**<sup>4+</sup> and the individual components of the bistable rotaxanes in MeCN determined by isothermal titration microcalorimetry at 298 K<sup>[38]</sup> in addition to solution-phase thermodynamic data of bistable rotaxanes.

Guest	$H^\circ$ [b] (kcal/mol)	$S^\circ$ [c] (cal/mol K)	$G^\circ$ [d] (kcal/mol)	$K_a$ [e] ( $10^3 \text{ M}^{-1}$ )
<b>TTF</b> <sup>[e]</sup>	$-10.64 \pm 0.12$	-18.1	$-5.27 \pm 0.03$	$6.9 \pm 0.18$
<b>TTF-DEG</b>	$-14.21 \pm 0.06$	-22.1	$-7.66 \pm 0.07$	$380.0 \pm 22.0$
<b>BPTTF</b> <sup>[f]</sup>	$-9.00 \pm 0.02$	-7.9	$-6.66 \pm 0.03$	$70.8 \pm 0.98$
<b>BPTTF-DEG</b>	$-8.20 \pm 1.70$	-3.6	$-7.17 \pm 0.12$	$168.0 \pm 17.0$
<b>DNP-OH</b> <sup>[g]</sup>	$-16.04 \pm 8.11$	-41.7	$-3.63 \pm 0.36$	$0.44 \pm 0.13$
<b>DNP-DEG</b> <sup>[h]</sup>	$-15.41 \pm 0.02$	-30.8	$-6.26 \pm 0.04$	$36.4 \pm 0.25$
<b>RATTF</b> <sup>4+ [i]</sup>	$-2.82 \pm 1.79$ <sup>[l]</sup>	$-14.7 \pm 6.8$ <sup>[l]</sup>	$+1.56 \pm 0.24$	
<b>RBPTTF</b> <sup>4+ [j]</sup>	$-6.64 \pm 0.67$	$-26.0 \pm 2.5$	$+1.11 \pm 0.07$	

[a] A 0.39 mM standard solution of **CBPQT**<sup>4+</sup> was used for all titrations into which solutions of various concentrations of guest were added in 5  $\mu\text{L}$  aliquots (4.7 mM **TTF**; 3.2 mM **TTF-DEG**; 5.0 mM **BPTTF**; 2.1 mM **BPTTF-DEG**; 5.4 mM **DNP-OH**; 3.9 mM **DNP-DEG**). [b] Under the constant pressure of the instrument,  $\Delta H^\circ$  is obtained from the heat of the reaction (65). [c] Fits were performed using software provided by Microcal LLC software, and the stoichiometry of all complexes was

between 0.97 and 1.03 indicating a 1:1 complex was formed. [d] Calculated from the fitted value of  $K_a$ . [e] The binding constant for the complex formed between **TTF** and **CBPQT<sup>4+</sup>**, previously measured in MeCN by the <sup>1</sup>H NMR single-point method, was determined (66, 67) to be 8,000 M<sup>-1</sup>, and was found (67) to be 10,000 M<sup>-1</sup> by the UV/Vis dilution method. [f] The binding constant for the complex formed between **BPTTF** and **CBPQT<sup>4+</sup>**, previously measured in Me<sub>2</sub>CO by the UV/Vis dilution method, was determined (68) to be 12,000 M<sup>-1</sup>. [g] The binding constant for the complex formed between **DNP-OH** and **CBPQT<sup>4+</sup>**, previously measured in MeCN by the UV/Vis dilution method, was determined (69) to be 990 M<sup>-1</sup>. [h] The binding constant for the complex formed between **DNP-DEG** and **CBPQT<sup>4+</sup>**, previously measured in MeCN by the UV/Vis dilution method, was determined (69) to be 25,400 M<sup>-1</sup>. [i] The given thermodynamic values for **RATTF<sup>4+</sup>** and **RBPTTF<sup>4+</sup>** were obtained by the variable temperature CV measurements. [j] The linear fit to  $\Delta G^\circ/T$  vs.  $1/T$  for **RATTF<sup>4+</sup>** produced a low R<sup>2</sup> of 0.4 because the  $\Delta G^\circ$  for **RATTF<sup>4+</sup>** was reasonably insensitive to temperature changes and therefore the data obtained reflects the standard error from the CV measurements.

The enthalpic contribution  $\Delta H^\circ$  to the binding affinity  $K_a$  between **DNP-DEG** and the **CBPQT<sup>4+</sup>** host is similar (Table 2-1) to that for **TTF-DEG**, but it is almost double that for **BPTTF-DEG**. This larger difference between the enthalpy changes ( $\Delta H^\circ$ ) of the two complexes is also represented in the bistable rotaxanes by the enthalpy change ( $\Delta H^\circ$ ) associated with the affinity of the **CBPQT<sup>4+</sup>** ring for the two recognition units. Correspondingly, the bistable rotaxane **RBPTTF<sup>4+</sup>** (-7.2 to -6.6

kcal/mol) shows a much higher  $\Delta H^\circ$  than **RATTF**<sup>4+</sup> (-1.2 to -2.8 kcal/mol). The direct consequence of this large  $\Delta H^\circ$  difference between the complexes of the **CBPQT**<sup>4+</sup> host with **DNP-DEG** and **BPTTF-DEG** is that the MSCC/GSCC ratio for **RBPTTF**<sup>4+</sup> exhibits a strong temperature dependence such that the ratio changes from 0.73 at 262 K to 0.25 at 284 K. The impact of temperature on equilibrium constants,  $K$  and their associated population ratios, MSCC/GSCC, are related by the Eyring equation ( $\Delta H^\circ / T - \Delta S^\circ = -R \ln K$ ) such that it is the enthalpic contribution that determines the temperature sensitivity.

Moreover, this variable ratio should be detectable in all three environments. In the solution phase and polymer gels, the MSCC/GSCC ratio can be quantified directly through CV measurements. In the MSTJs, the temperature dependent MSCC/GSCC ratio should be reflected in a temperature-dependent switching amplitude. By contrast with **RBPTTF**<sup>4+</sup>, the smaller  $\Delta H^\circ$  difference for the binding of the **CBPQT**<sup>4+</sup> ring to the TTF and DNP units should favor a relatively temperature-independent MSCC/GSCC ratio in **RATTF**<sup>4+</sup>, with the GSCC remaining the dominant conformation at all temperatures and in all environments, a situation which is indeed observed. Irrespective of these differences in the ground state thermodynamics, for both **RATTF**<sup>4+</sup> and **RBPTTF**<sup>4+</sup>, the actual electrochemically-driven switching mechanism should be the same.

## 2.3 Kinetics and Thermodynamics of Switching in Solution and in Polymer Electrolytes

The Heath and Stoddart research groups have previously demonstrated that the first oxidation potentials of bistable rotaxanes can be utilized to quantify the MSCC/GSCC ratios in the solution phase (40), for monolayers assembled onto Au surfaces (41), and for polymer electrolyte gels (39). In this section, I report on a set of similar variable time and temperature cyclic voltammetry (VTTCV) measurements in solution and polymer environments to probe the thermodynamics of the MSCC/GSCC equilibrium ratios for **RATTF**<sup>4+</sup> and **RBPTTF**<sup>4+</sup>. From these measurements, I can extract free energy differences ( $\Delta G^\circ$  from figure 2-1b) between the two conformations.

I also utilized VTTCV to quantify the kinetics ( $\Delta G^\ddagger$  from figure 2-1b) associated with the recovery of the equilibrium MSCC/GSCC distribution for **RBPTTF**<sup>4+</sup> and **RATTF**<sup>4+</sup>. The relaxation kinetics for [2]rotaxane **RATTF**<sup>4+</sup> and for related TTF-based rotaxanes, were thoroughly investigated previously (39-41), while the equivalent VTTCV measurements for **RBPTTF**<sup>4+</sup> are reported here.

The VTTCV measurements are carried out as follows: two CV cycles are collected in succession, starting with the system at equilibrium. This first CV cycle displays peaks that can be assigned to the resting state populations of the MSCC and

GSCC, since the first oxidation potential of the TTF (BPTTF) group is sensitive to whether or not it is encircled by the CBPQT<sup>4+</sup> ring. The second cycle, if collected quickly enough, records a shift in the equilibrium population towards the one dominated by the MSCC. This shift is reflected in an increase in the area of the peak assigned to the MSCC, in coincidence with a decrease in the area for the GSCC peak. By controlling the time between the first and second CV cycles, and the temperature of the experiment, the kinetic parameters associated with the recovery of the MSCC/GSCC equilibrium ratio can be quantified. The representative CV data for **RBPTTF**<sup>4+</sup> showing the enhanced MSCC peak in the second cycle and scan-rate dependence for maintaining the MSCC peak in the second cycle were presented in figure 2-4.

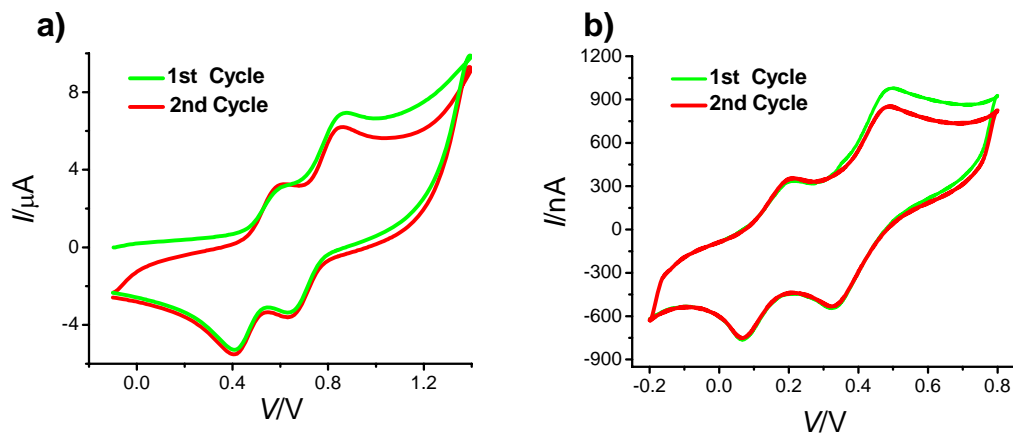


**Figure 2-4.** CV data of **RBPTTF<sup>4+</sup>** recorded in acetonitrile and polymer gel. Two cycles of CV data displayed enhanced MSCC peak in the second cycle in both (a) acetonitrile (measured at 800 mV/s, 262 K) and (b) polymer gel (measured at 130 mV/s, 303 K).

I first focus on utilizing VTTCV to probe the MSCC/GSCC population ratio at thermal equilibrium. The CVs of **RBPTTF<sup>4+</sup>** in the solution phase exhibit a peak at +530 mV, which corresponds to the  $\text{BPTTF} \rightarrow \text{BPTTF}^{*+}$  oxidation of the proportion of the bistable rotaxane that exists in the MSCC (figure 2-4a). The smaller peak at +680 mV corresponds to the  $\text{BPTTF} \rightarrow \text{BPTTF}^{*+}$  oxidation of the GSCC. The larger peak at +780 mV corresponds to the second oxidation ( $\text{BPTTF}^{*+} \rightarrow \text{BPTTF}^{2+}$ ). This second oxidation is independent of the co-conformation, since once the  $\text{BPTTF}^{*+}$  is formed, the  $\text{CBPQT}^{4+}$  ring moves to the DNP unit. The MSCC/GSCC population was thus measured as a function of temperature. For **RBPTTF<sup>4+</sup>**, decreasing the temperature led to a significant increase in the MSCC/GSCC population ratio. The ratio, for

example, increases (figure 2-5a) more than two-fold (from around 0.3 to 0.7) as the temperature is decreased from 284 to 262 K. By comparison, for **RATTF**<sup>4+</sup>, the MSCC/GSCC population ratio does not deviate significantly from 0.1, even when the rotaxane is probed (figure 2-5b) over a broader temperature range (248 – 283 K).

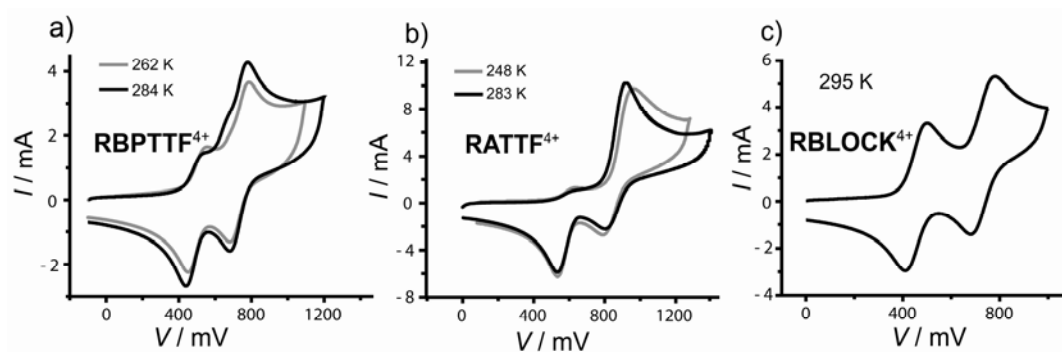


**Figure 2-5.** The first CV cycles of (a) **RBPTTF**<sup>4+</sup> recorded at 262 and 284 K, (b) **RATTF**<sup>4+</sup> recorded at 248 and 283 K and (c) **RBLOCK**<sup>4+</sup> recorded at 295 K (MeCN / 0.1 M TBAPF<sub>6</sub> / 200 mV s<sup>-1</sup>). The peak assigned to the MSCC at ca. +500 mV for **RBPTTF**<sup>4+</sup> fluctuates more than for **RATTF**<sup>4+</sup> across different temperature ranges. The simple, dumbbell-like CV for **RBLOCK**<sup>4+</sup>, displaying a full-intensity MSCC peak at ca. 500 mV, verifies that the CBPQT<sup>4+</sup> ring is sterically blocked.

The relative temperature dependences of the MSCC/GSCC ratios for **RBPTTF**<sup>4+</sup> and for **RATTF**<sup>4+</sup> are consistent with the ITC investigations of the complexation of the **CBPQT**<sup>4+</sup> host with the individual **BPTTF-DEG**, **TTF-DEG**, and **DNP-DEG** guests that were discussed in the previous subchapter and presented in Table 2-1. Translating the behavior of the guests to what might be predicted for the

two bistable [2]rotaxanes, one expects that the enthalpic contribution  $\Delta H^\circ = (H^\circ_{\text{MSCC}} - H^\circ_{\text{GSCC}})$  should be significantly less than 0 for **RBPTTF**<sup>4+</sup>. By comparison, the corresponding  $\Delta H^\circ$  for **RATTF**<sup>4+</sup> should be much closer to zero. As a consequence, the MSCC/GSCC ratio for **RBPTTF**<sup>4+</sup> varies more readily with temperature. The impact of temperature on equilibrium constants,  $K$  and their associated population ratios, MSCC/GSCC, are related by the Eyring equation ( $\Delta H^\circ / T - \Delta S^\circ = -R \ln K$ ) such that it is the enthalpic contribution that determines the temperature sensitivity.

Although it is not so straightforward to interpret, the long and flexible diethylene glycol chains appear to have an impact on the binding  $K_a$  and therefore the population ratios of the bistable rotaxanes. The DEG chains enhance (Table 2-1) the binding affinity for each of the three guests with the **CBPQT**<sup>4+</sup> host, but they do so by influencing the  $\Delta H^\circ$  and  $\Delta S^\circ$  of each component differently. For **TTF-DEG**, the DEG chains leads to better enthalpy but worse entropy. However, for the **DNP-DEG** and **BPTTF-DEG** guests, it is the opposite with the entropy contribution favoring binding and enthalpy disfavoring it, albeit only mildly so. Furthermore, it is known that when these DEG chains are attached to DNP and TTF units they are capable of wrapping themselves around the **CBPQT**<sup>4+</sup> ring in order to acquire stabilizing, noncovalent [C–H···O] interactions (63, 64). Consequently, the significant enhancement of the enthalpic contribution to the complexation between **TTF-DEG**

and the **CBQPT**<sup>4+</sup> host by the DEG chains brings its  $\Delta H^\circ$  to within a few kcal / mol of the **DNP-DEG** guest, leading to a relatively temperature insensitive MSCC/GSCC ratio for the rotaxane **RATTF**<sup>4+</sup>. However, the DEG chains have little effect on the  $\Delta H^\circ$  contribution to complexation of the **DNP-DEG** and **BPTTF-DEG** guests by the **CBPQT**<sup>4+</sup> host such that they maintain their large and significant differences in enthalpy within the **RBPTTF**<sup>4+</sup>, leading to the rotaxane's correspondingly large sensitivity of the population ratios to temperature. The DEG chains are thus an essential factor influencing the temperature sensitivities of the MSCC/GSCC population ratios of these bistable rotaxanes. The observation from the electrochemical studies in the solution phase and in the polymer matrix provide a view of both **RATTF**<sup>4+</sup> and **RBPTTF**<sup>4+</sup> that is completely consistent with the ITC measurements on the subunits of the rotaxanes. It is also consistent with the molecular structure differences between these two switches.

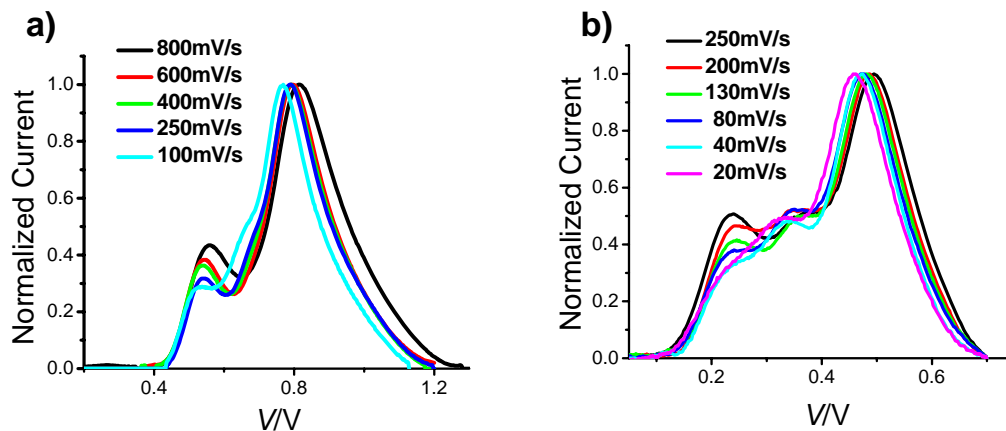


**Figure 2-6.** Normalized CV data in the second cycles. The larger MSCC peaks in the second cycle were maintained at faster scan rate in both (a) acetonitrile at 284 K and (b) polymer gel at 313 K. CV currents were normalized after subtracting base lines from original currents.

The relaxation kinetics and thermodynamics associated with the free energy barrier ( $\Delta G^\ddagger$ ) for relaxation from the MSCC to the GSCC for **RATTF**<sup>4+</sup> and **RBPTTF**<sup>4+</sup> were also analyzed quantitatively. The viscosity of the acetonitrile solution phase and polymer gel were about 3.5 cp and 50,000 cp at 298 K, respectively. This large increase in viscosity is reflected in the slower first-order decay kinetics for **RBPTTF**<sup>4+</sup> as measured by VTTCV. Data for acetonitrile solution and the polymer gel are presented in figures 2-6 and 2-7. In addition to the viscosity effects, these plots also reveal how the thermally activated relaxation rates drop as the temperature is lowered.

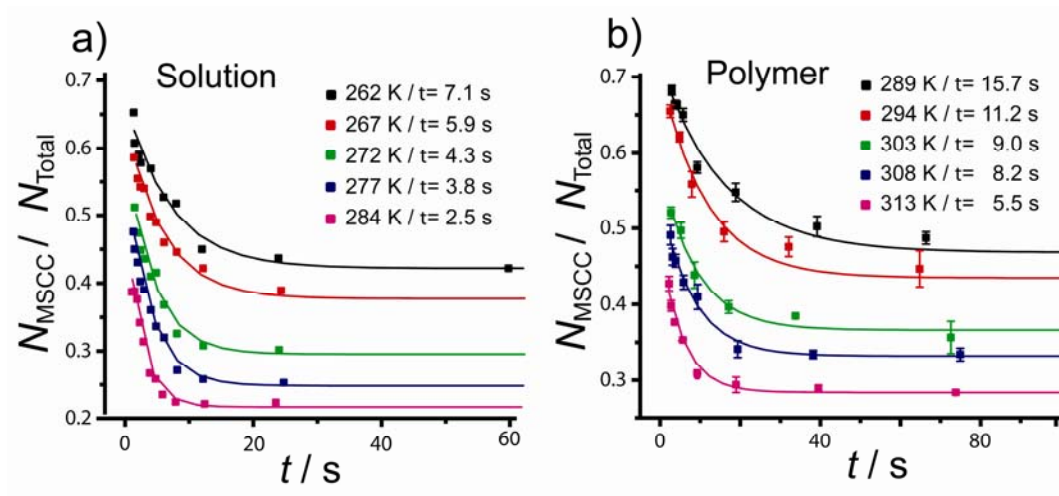
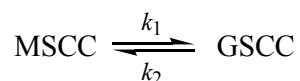


**Figure 2-7.** MSCC  $\rightarrow$  equilibrium kinetics of **RBPTTF**<sup>4+</sup> in solution and polymer phases. Fitted exponential decay curves and time constants ( $t$ ) obtained from the CV data for **RBPTTF**<sup>4+</sup> measured at various scan rates for each temperature in (a) solution and (b) polymer phases are presented.

It's instructive to notice that both the MSCC and GSCC are at significant concentrations under equilibrium conditions for **RBPTTF**<sup>4+</sup>, especially at lower temperatures. The implication is that the reverse reaction GSCC  $\rightarrow$  MSCC is occurring at a rate comparable to that of the forward reaction. In analyzing the relaxation kinetics, both processes should be taken into consideration. Thus, for the equilibrium reaction:



Eq. 1

the formula:

$$x_t = x_{eq} + (x_0 - x_{eq}) \exp\left(-\frac{k_1}{1-x_{eq}} t\right) \quad \text{Eq. 2}$$

is readily obtained, in which  $x_t = \frac{N_{\text{MSCC}}}{N_{\text{Total}}}$  is the MSCC population ratio at time  $t$ ,

$x_0 = x_{t=0}$ , and  $x_{eq} = x_{t \rightarrow \infty}$  is the MSCC population ratio at final equilibrium.

Experimental relaxation data were thus fitted with this formula to obtain the decay

time constant  $\tau$ , and accordingly the rate constant for the forward reaction

$k_1 = \frac{1-x_{eq}}{\tau}$ . Note that when  $x_{eq}$  is small (i.e., for the case of **R(A)TTF<sup>4+</sup>**), the

formula naturally reduces to the more familiar formula for a simple first-order

reaction.  $\Delta G^\ddagger$ ,  $\Delta H^\ddagger$ ,  $\Delta S^\ddagger$ , and  $E_a$  are then fitted from the temperature dependence of

$k_1$ .  $G^\ddagger$  at each temperature was calculated from the Eyring equation:

$$\Delta G^\ddagger = -RT \ln \left( \frac{hk}{k_B T} \right)$$

where  $R$ ,  $h$ ,  $k$  and  $k_B$  are the gas constant, Planck's constant, the first-order rate

constant and Boltzmann constant, respectively.  $k$  corresponds to  $(1 - x_{eq})/\tau$ , where  $x_{eq}$

is  $N_{\text{MSCC}}/N_{\text{Total}}$  at equilibrium and  $\tau$  is 1/e decay time constant.  $\Delta H^\ddagger$  and  $\Delta S^\ddagger$  were

obtained from the regression analysis of Gibbs-Helmholtz plot,  $\Delta G^\ddagger/T$  vs.  $1/T$ . The

activation barrier,  $E_a$  was calculated from the Arrhenius equation:

$$k = A \exp \left( \frac{-E_a}{RT} \right)$$

where  $A$  is the activation coefficient.  $E_a$  was obtained from a regression analysis of the Arrhenius plots,  $\ln k$  vs.  $1/T$ . The kinetic data are summarized in Table 2-2 alongside values for **R(A)TTF**<sup>4+</sup>. Note that the MSCC/GSCC population ratio for **RBPTTF**<sup>4+</sup>, as measured at long times (at equilibrium) shows (figure 2-7) significant sensitivity to temperature, consistent with the thermodynamic descriptions and data for the host-guest complexation. By contrast, **RATTF**<sup>4+</sup> displays only a small thermal sensitivity in both the polymer and solution phase environments.

## 2.4 Kinetics and Thermodynamics of Molecular Switch Tunnel Junctions

The MSTJs investigated here contained a monolayer of the amphiphilic bistable rotaxanes **RTTF**<sup>4+</sup> or **RBPTTF**<sup>4+</sup>, or the sterically-blocked metastable-like rotaxane **RBLOCK**<sup>4+</sup>, sandwiched between an n-type poly-silicon bottom electrode (passivated with the native oxide) and a metallic top electrode. The detailed procedures relating to the fabrication and operation of these devices have been reported (34-36). Briefly, the molecules are prepared as a Langmuir-Blodgett film and then transferred as a compressed Langmuir monolayer ( $\pi = 30$  mN/m) onto a substrate pre-patterned with poly-silicon electrodes. A thin 10 nm Ti adhesion layer, followed by a thicker 200 nm top Al layer is evaporated through a shadow mask using e-beam

evaporation to form the top electrodes. During this step, the substrate is held at room temperature at a source-sample distance of  $\sim 0.7$  m. This procedure ensures that little or no substrate heating from the e-beam evaporation source occurs. The e-beam evaporation was processed at the deposition rate of  $1 - 2 \text{ \AA/s}$  under high vacuum ( $\sim 5 \times 10^{-7}$  Torr). For all experiments reported here, the bottom electrodes were  $5 \text{ }\mu\text{m}$  wide, n-type (doping level  $\sim 5 \times 10^{19} \text{ cm}^{-3}$ ) poly-Si, while the top electrodes were  $10 \text{ }\mu\text{m}$  wide. Each fabrication run produced approximately 100 MSTJ devices, and the results presented here were consistently observed in multiple devices across multiple fabrication runs, with temperature-dependent data collected in random sequence. More than 90 % of MSTJ devices showed the similar temperature-dependence reproducibly. The operational characteristics of MSTJs containing bistable catenanes and rotaxanes, but patterned at both larger and also much smaller dimensions, have been reported (36, 37).

CV measurements are not possible for MSTJs, but there are other electronic measurements that can be carried out to assess both the thermodynamic and kinetic properties of the bistable rotaxanes within the devices. The hypothesis – for both bistable catenanes and bistable rotaxanes – has been refined such that the MSCC represents the high-conducting, switch-closed state of the device, while the MSCC/GSCC ratio at equilibrium represents the low-conducting, switch-open state.

For an MSCC-dominated system, regardless of environment, reduction of the CBPQT<sup>4+</sup> ring provides a rapid route towards recovering the equilibrium MSCC/GSCC distribution (35, 41). In the absence of such a reduction step, a device in the high-conductance state will relax to the equilibrium MSCC/GSCC ratio, according to a timescale described by  $\Delta G^\ddagger$  (figure 2-1b). From a practical point of view (i.e., for memory devices), this relaxation process correlates to the volatility, or memory-retention characteristics, of the device. The volatility can be quantified by measuring the temperature dependence of the decay of the switch-closed, high conductance state of a device back to the switch-open state.

The equilibrium thermodynamic properties of the devices can also be inferred within MSTJs by considering that the high- and low-conductance states of the devices correlate with different MSCC/GSCC ratios. Thus, the temperature-dependent switching amplitude, normalized against the temperature-dependent transport characteristics of an MSTJ, opens a window into the thermodynamics of the molecules within the junction. Such a measurement provides a qualitative picture that can be compared against quantitative VTTCV measurements of the MSCC/GSCC ratios in other environments.

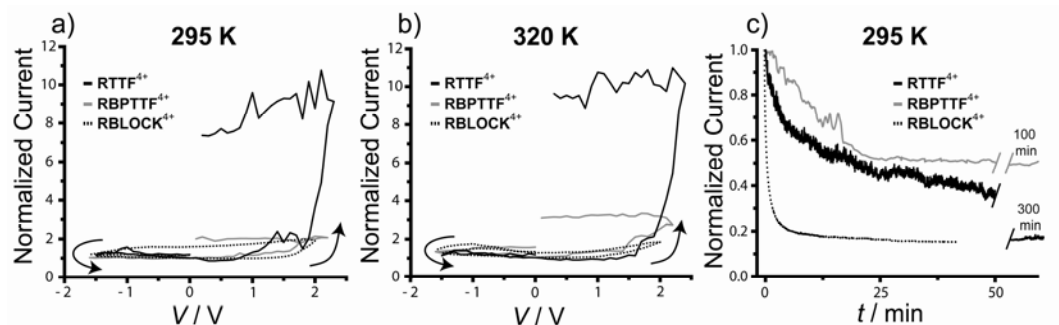


**Figure 2-8.** Switching responses of three rotaxanes within MSTJs. (a) and (b): Remnant molecular signature traces of the hysteretic switching responses. The arrows indicate the direction of the voltage sweep, and all currents were recorded at +0.1 V. The y-axis current was normalized by setting the initial (low-conductance state) current to 1. Note that the response of **RBPTTF**<sup>4+</sup> increases in amplitude at higher temperature, reflecting a decreasing MSCC/GSCC equilibrium ratio, while **RTTF**<sup>4+</sup> is relatively constant. There is a finite amount of field-induced polarization in **RBLOCK**<sup>4+</sup> that is almost undetectable at 320 K. (c) Relaxation of MSTJs from high- to-low conducting states recorded at 295 K. The characteristic relaxation times are: **RTTF**<sup>4+</sup> = 3450 s; **RBPTTF**<sup>4+</sup> = 660 s; **RBLOCK**<sup>4+</sup> = 60 s.

Measurements of the bistable character of MSTJs containing **RTTF**<sup>4+</sup>, **RBPTTF**<sup>4+</sup>, and the **RBLOCK**<sup>4+</sup> control rotaxane are shown in figures 2-8a and 2-8b. This type of data is called a remnant molecular signature (34-36), and represents a nearly capacitance-free map of the hysteretic response of an MSTJ. Briefly, the x-axis of a remnant molecular signature plot correlates to a value of a voltage pulse that is applied across the junction. A train of voltage pulses, starting at 0 V and following the direction of the arrows shown on the plots, is applied to the MSTJ, and, after each

voltage pulse, the current through the MSTJ is monitored at +0.1 V. The remnant molecular signature is a sequence of voltage pulses of 1 s that are applied to poly-Si electrodes with 100 mV step sizes and, in between each pulse, is a read voltage of +0.1 V held for 1.5 s to record the current. The metal top electrodes were connected to ground through a preamplifier. The resulting normalized current is represented on the y-axis. These hysteresis loops not only provide a key indicator that the MSTJs can be switched reversibly between the high- and low-conducting states, but they also qualitatively reflect the ground state MSCC/GSCC ratio, since the switching amplitude is sensitive to this ratio. For the high-conductance state, in which the entire population has been converted into the MSCC, the maximum current is controlled by the intrinsic conductance properties of this co-conformation. However, for the low-conductance state, the minimum conduction is not only controlled by the intrinsic properties of the GSCC but also by the MSCC/GSCC ratio – a factor under thermodynamic control. For instance, at 295 K **RBPTTF**<sup>4+</sup> and **RBLOCK**<sup>4+</sup> do not appear to be ‘good’ switches, while the switching amplitude of **RTTF**<sup>4+</sup> is about a factor of 8. At 320 K, the small hysteretic response for **RBLOCK**<sup>4+</sup> has further diminished, but the hysteresis loop of **RBPTTF**<sup>4+</sup> has opened up to yield a switching amplitude (i.e., the current measured in the high conductance state divided by the current measured in the low conductance state) of over 3. This enhanced switching

amplitude presumably reflects a smaller MSCC/GSCC equilibrium ratio at the higher temperature, and is consistent with what is observed for the solution and polymer phase measurements for **RBPTTF**<sup>4+</sup>. The switching amplitude of **RTTF**<sup>4+</sup> remains fairly constant across this temperature range, consistent again with measurements in the other environments. The MSCC → GSCC relaxation kinetics can be monitored by measuring the time-dependence of the decay of the high-conductance to the low-conductance state, and that data, for all three amphiphilic rotaxanes at 295 K, is presented in figure 2-8c.

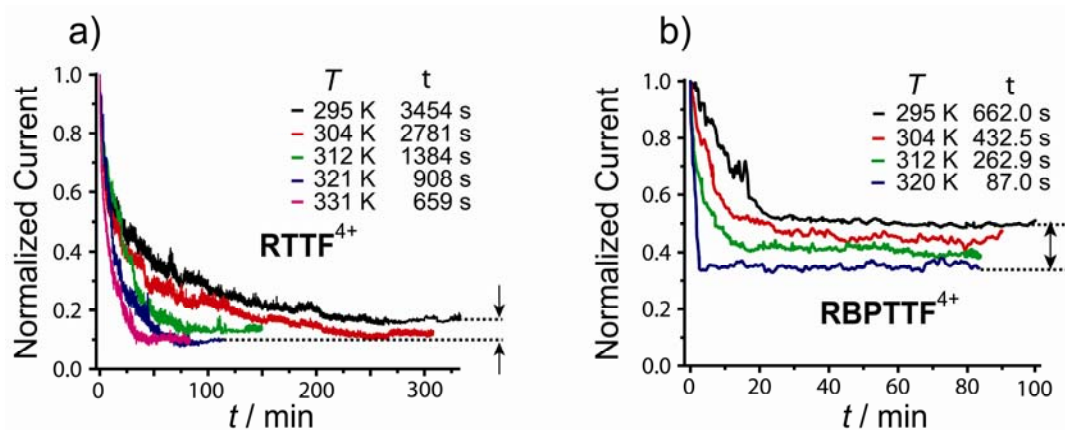


**Figure 2-9.** Decay curves of (a) **RTTF**<sup>4+</sup> and (b) **RBPTTF**<sup>4+</sup> MSTJs recorded as a function of temperature. Note that the normalized switching amplitude of **RBPTTF**<sup>4+</sup> exhibits a strong temperature dependence.

The high- to low-conductance decay of all three rotaxanes exhibited different temperature dependences. While MSTJs fabricated from **RBPTTF**<sup>4+</sup> and **RTTF**<sup>4+</sup> show strong temperature dependences – as the temperature was increased from 295 K

to 320 K, the  $1/e$  decay time decreased by factors of 6 – 7 for those rotaxanes (figure 2-9) – **RBLOCK**<sup>4+</sup> exhibited a much weaker temperature dependence. MSTJs fabricated from **RBLOCK**<sup>4+</sup> were investigated over a broader temperature range (295 – 383 K) and the characteristic relaxation time decreased by only a factor of 2 or so over this entire range. This decay-rate data fitted well to a  $1/T$  plot ( $R^2 > 0.99$ ), which is at least consistent with existing models for dielectric relaxation (70), although measurements over an even broader temperature range would be required to establish this relationship more firmly. In any case, MSTJs fabricated from **RBLOCK**<sup>4+</sup> were poor switches at all temperatures investigated, and the small switching response that could be recorded exhibited a very different and much less-pronounced temperature-dependence, in comparison to MSTJs fabricated from **RBPTTF**<sup>4+</sup> and **RTTF**<sup>4+</sup>. The switching amplitude can be recorded by either measuring the amplitude of the hysteresis loops from the remnant molecular signature data, or by measuring the time-dependent decay of the high- to the low-conductance state. Any molecular electronic junction for which charge transport is not strictly a quantum mechanical tunneling process will exhibit a strong temperature dependent conductance, i.e., charge transport is thermally activated, and the rate of transport increases with increasing temperature. This is the case for all three of the amphiphilic rotaxanes investigated here. However, this temperature-dependent component should depend only weakly upon molecular

structure – especially for molecules that are as similar as **RTTF**<sup>4+</sup>, **RBPTTF**<sup>4+</sup>, and **RBLOCK**<sup>4+</sup>, and should not be particularly sensitive to the MSCC/GSCC ratio within a device. Thus, I remove this component of the temperature dependence by normalizing the switching amplitude to the initial current value, measured at  $t = 0$  after placing the switch into the high conductance state. The hypothesis is that the (normalized) current at long times – i.e., when the system has reached equilibrium – divided by the  $t = 0$  current, should correlate qualitatively with the MSCC/GSCC ratio. To the first order, the normalized current at equilibrium defined by the  $I_{\text{OPEN}}/I_{\text{CLOSED}}$  ratio is approximately equal to  $N_{\text{MSCC}}/N_{\text{Total}}$  if the intrinsic conductance of the GSCC is smaller by more than two orders of magnitude.

Based on the refined hypothesis that, the high-conductance (switch-closed) state of an MSTJ corresponds to the MSCC but that the low-conductance (switch-open) state is related to the MSCC/GSCC ratio at equilibrium, the measured current,  $I$ , can be defined in terms of the intrinsic conductance properties of each co-conformation and the percentage of the co-conformations  $N_{\text{MSCC}}/N_{\text{Total}}$  and  $N_{\text{GSCC}}/N_{\text{Total}}$ .

Consequently,  $I_{\text{OPEN}}$  corresponds to a thermal equilibrium condition and is a mixture of the GSCC and MSCC, whereas  $I_{\text{CLOSED}}$  is 100% of the MSCC. This model influences the meaning of the ratio  $I_{\text{OPEN}}/I_{\text{CLOSED}}$ .

The conductance properties of these systems can be described as follows:

Firstly, the GSCC and MSCC have intrinsic current values  $I_{GSCC}$  and  $I_{MSCC}$ , which are constants at a certain temperature  $T$ . Therefore, at any time the current measured,  $I_t$ , is a summation of these two contributions. The magnitude of each contribution is scaled by the proportions of the GSCC ( $N_{GSCC}/N_{Total}$ ) and MSCC ( $N_{MSCC}/N_{Total}$ ) present in the mixture. This leads to the following general formula for the current  $I_t$ :

$$I_t = \left( \frac{N_{MSCC}}{N_{Total}} \right)_t * I_{MSCC} + \left( \frac{N_{GSCC}}{N_{Total}} \right)_t * I_{GSCC} \quad \text{Eq. 3}$$

Therefore, for the trivial situation when  $I_{CLOSED}$  is measured at  $t = 0$ , I assume that  $N_{GSCC} = 0$  and  $N_{MSCC}/N_{Total} = 1$  confirming that  $I_{CLOSED} = I_{MSCC}$  (see figure 2-10).

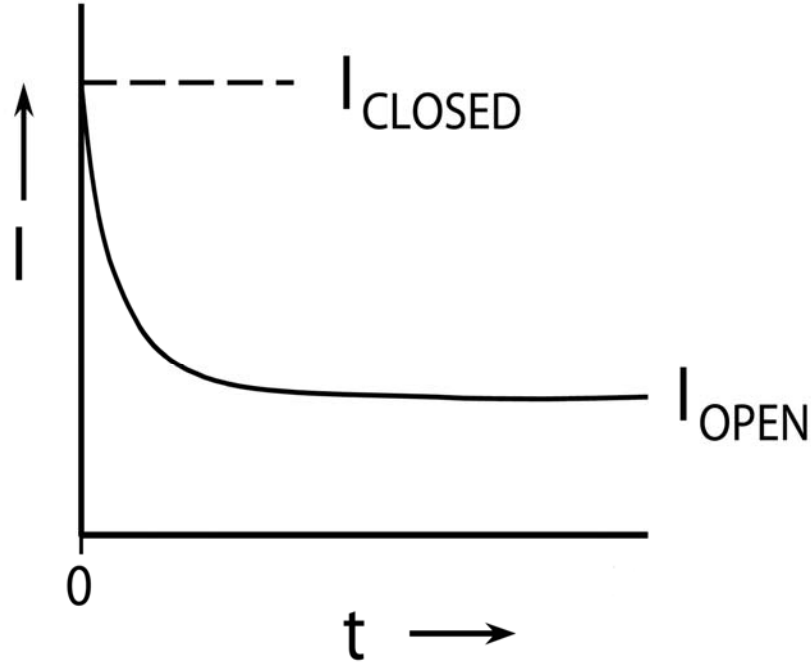


**Figure 2-10.** Schematic representation of a volatility curve defining  $I_{CLOSED}$  and  $I_{OPEN}$ .

Now consider what happens at thermal equilibrium ( $t = \infty$ ), defined as  $I_{OPEN}$ :

$$I_{OPEN} = \left( \frac{N_{MSCC}}{N_{Total}} \right)_{\infty} * I_{CLOSED} + \left( \frac{N_{GSCC}}{N_{Total}} \right)_{\infty} * I_{GSCC} \quad \text{Eq. 4}$$

Consequently, the ratio  $I_{OPEN}/I_{CLOSED}$ , which happens to be the inverse of the

switching amplitude, can be expressed as:

$$\frac{I_{OPEN}}{I_{CLOSED}} = \left( \frac{N_{MSCC}}{N_{Total}} \right)_{\infty} + \left( \frac{N_{GSCC}}{N_{Total}} \right)_{\infty} * \frac{I_{GSCC}}{I_{CLOSED}} \quad \text{Eq. 5}$$

If the intrinsic conductance of the GSCC is very small compared to  $I_{CLOSED}$ , the term

$I_{GSCC}/I_{CLOSED}$  goes to zero and therefore:

$$I_{OPEN}/I_{CLOSED} = N_{MSCC}/N_{Total} \quad \text{Eq. 6}$$

For example, in the case of **R(A)TTF**<sup>4+</sup>,  $N_{MSCC}/N_{Total} = 1/10$  and assuming an intrinsic

conductance of the GSCC that is 100 times smaller than the MSCC,  $I_{\text{GSCC}}/I_{\text{Closed}} = 1/100$  then the ratio at  $t = \infty$  becomes:

$$I_{\text{OPEN}}/I_{\text{CLOSED}} = 1/10 + (9/10 * 1/100) = 1/10 + 9/1000 = 0.1 + 0.009 = 0.109$$

Consider also how **RBPTTF**<sup>4+</sup> behaves at low temperatures (MSCC/GSCC = 3:4):

$$I_{\text{OPEN}}/I_{\text{CLOSED}} = 3/7 + (4/7 * 1/100) = 0.43 + 0.006 = 0.436$$

In other words, the ratio of  $N_{\text{MSCC}}/N_{\text{Total}}$  dominates the  $I_{\text{OPEN}}/I_{\text{CLOSED}}$  measured ratio at equilibrium and therefore the switching amplitude in the condition when the intrinsic conductance of the GSCC is small.

Whereas in the condition when the intrinsic conductance of the GSCC were higher such as if  $I_{\text{GSCC}}/I_{\text{CLOSED}} = 1/10$ , then for **R(A)TTF**<sup>4+</sup>:

$$I_{\text{OPEN}}/I_{\text{CLOSED}} = 1/10 + (9/10 * 1/10) = 1/10 + 9/100 = 0.1 + 0.09 = 0.19$$

and for **RBPTTF**<sup>4+</sup>:

$$I_{\text{OPEN}}/I_{\text{CLOSED}} = 3/7 + (4/7 * 1/10) = 0.43 + 0.06 = 0.49$$

Comparing between the two cases, where  $I_{\text{GSCC}}$  is comparatively smaller (1%) or larger (10%) leads to switching amplitudes for **R(A)TTF**<sup>4+</sup> of 9 and 5, respectively, whereas for **RBPTTF**<sup>4+</sup> they correspond to 2.3 and 2.0.

Small relative intrinsic conductances of the GSCC compared to the MSCC are not so unlikely and have been calculated (61, 62) for related TTF-containing bistable catenanes, based on the theory of coherent electron transport, to be approximately

1/10,000.

In figure 2-9, I present such normalized decay curves, for various temperatures, for both **RTTF**<sup>4+</sup> and **RBPTTF**<sup>4+</sup>. Note two things about the data of figure 2-9. First, the curves clearly represent activated processes, since, for both bistable rotaxanes, the relaxation times decrease rapidly with increasing temperature. Second, the switching amplitude for **RTTF**<sup>4+</sup> is relatively temperature independent, exhibiting almost an order-of-magnitude difference in the (normalized) current change between the high- and low-conductance states for all temperatures. By contrast, the switching amplitude for **RBPTTF**<sup>4+</sup> exhibits a strong temperature dependence over the same range. This observation is consistent with the remnant molecular signature data presented in figure 2-8. Also, it is consistent with the behavior of the corresponding bistable rotaxanes (**RATTF**<sup>4+</sup> and **RBPTTF**<sup>4+</sup>) in the other environments, as well as the ITC data obtained from host-guest complexation experiments.

## **2.5 A Summary of Kinetic and Thermodynamic Studies in All of Three Environments**

The temperature-dependent thermodynamic and relaxation kinetic data for all environments are presented in figures 2-11a and 2-11b, respectively. In figure 2-11a I have plotted the temperature-dependent ratios as  $N_{\text{MSCC}}/N_{\text{TOTAL}}$ , quantitatively

measured in the solution-phase and polymer environments. For the MSTJs, this ratio cannot be quantified, but the temperature-dependent switching amplitude  $I_{\text{OPEN}}/I_{\text{CLOSED}}$  provides for qualitative comparison with the other environments. For the relaxation kinetics, data for the two TTF-containing rotaxanes (**R(A)TTF**<sup>4+</sup>) and **RBPTTF**<sup>4+</sup> are plotted in the form of Eyring plots, in order to quantify (Table 2-2)  $\Delta G^\ddagger$ ,  $\Delta H^\ddagger$ , and  $\Delta S^\ddagger$  in all three environments.

**Table 2-2.** Kinetics data for the relaxation from the MSCC to the GSCC for **RBPTTF**<sup>4+</sup> and the free energy barriers for **RATTF**<sup>4+</sup> and **RTTF**<sup>4+</sup>. Data for solution, polymer and MSTJ were obtained from variable temperature CVs and from measurements of the relaxation of a MSTJ from the high to the low conductance state.

Environ.	$\tau_{298}$ [s]	$k_{298}$ [s <sup>-1</sup> ]	$\Delta G_{298}^{\ddagger}$ [kcal·mol <sup>-1</sup> ]	$\Delta H^{\ddagger}$ [kcal·mol <sup>-1</sup> ]	$\Delta S^{\ddagger}$ [cal·mol <sup>-1</sup> K <sup>-1</sup> ]	$E_a$ [kcal·mol <sup>-1</sup> ]	$\Delta G_{298}^{\ddagger}$ <b>RATTF</b> <sup>4+</sup>	$\Delta G_{298}^{\ddagger}$ <b>RTTF</b> <sup>4+</sup>
Solution <sup>[a]</sup>	1.26 ± 0.10	0.69 ± 0.05	17.69 ± 0.05	8.4 ± 0.5	-31.0 ± 1.7	9.0 ± 0.5	16.2 ± 0.3	–
Polymer <sup>[b]</sup>	10.2 ± 0.12	0.059 ± 0.001	19.15 ± 0.01	8.4 ± 1.1	-36.0 ± 3.4	9.0 ± 1.0	18.1 ± 0.2	–
MSTJ	624 ± 82	(8.4 ± 0.8) × 10 <sup>-4</sup>	21.7 ± 0.1	16.1 ± 1.4	-18.7 ± 4.1	16.7 ± 1.3	–	22.21 ± 0.04

[a] Solution-phase data was obtained for 1 mM samples dissolved in MeCN (0.1 M TBAPF<sub>6</sub>) using a glassy carbon working electrode. All potentials were referenced to a Ag/AgCl reference electrode (40). [b] Polymer-phase data was obtained in a polymer matrix - w:w:w:w ratios of 70:7:20:3 for MeCN:polymethylmethacrylate:propylene carbonate:LiClO<sub>4</sub>. The sample was spread onto three lithographically-patterned Pt electrodes (50 nm) on top of Ti (10 nm) (working, counter, reference)(39). The  $\Delta H^{\ddagger}$  and  $\Delta S^{\ddagger}$  were obtained from an average of many devices while the Eyring plot in figure 2-10 b represents just one device.

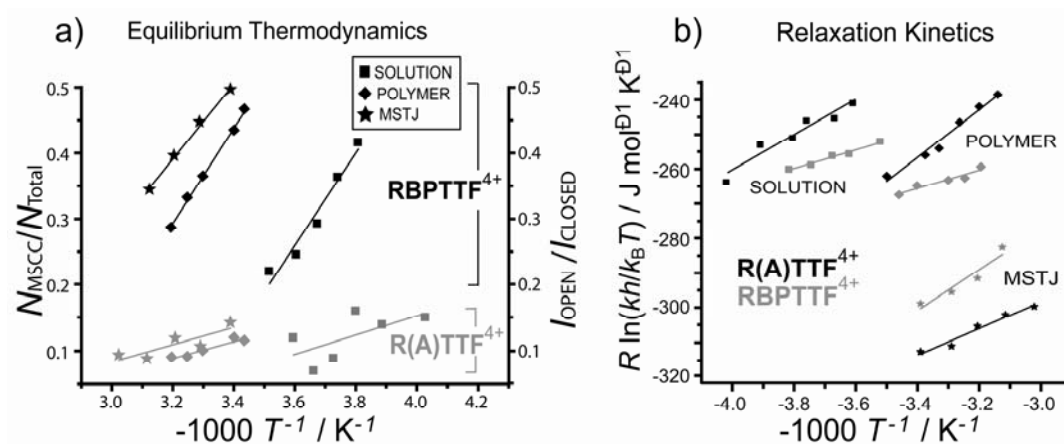


**Figure 2-11.** (a) The temperature-dependent GSCC/MSCC equilibria for all three environments are presented. Solution and polymer phase data ( $N_{\text{MSCC}}/N_{\text{Total}}$ ) were recorded for **RATTF<sup>4+</sup>** and **RBPTTF<sup>4+</sup>** and are based upon quantitative electrochemical measurements of the MSCC/GSCC ratios. The MSTJ data, which were recorded for **RTTF<sup>4+</sup>** and **RBPTTF<sup>4+</sup>**, show the temperature-dependent switching amplitude ( $I_{\text{OPEN}}/I_{\text{CLOSED}}$ ), and represent a qualitative measurement of the  $N_{\text{MSCC}}/N_{\text{Total}}$  ratio, based upon the proposed switching mechanism. Note that the large (enthalpically driven) temperature dependence for **RBPTTF<sup>4+</sup>**, and the relative temperature independence of **RATTF<sup>4+</sup>** and **RTTF<sup>4+</sup>** (**R(A)TTF<sup>4+</sup>**) is reflected in all environments. (b) Eyring plots of the MSCC  $\rightarrow$  GSCC (or high-conducting MSTJ  $\rightarrow$  low-conducting MSTJ) relaxation process, for all three environments.

I first consider the kinetic data of figure 2-11b and Table 2-2. For the case of **RBPTTF<sup>4+</sup>**, the free energy barrier ( $\Delta G^\ddagger$ ) to relaxation at 298 K increases from 17.7 to 19.2 to 21.7 kcal/mol upon moving from acetonitrile solution to polymer gels to MSTJs. For **R(A)TTF<sup>4+</sup>**, the situation is qualitatively similar. Both rotaxanes exhibit an increase in the energy barrier ( $\Delta G^\ddagger$ ) from the solution to polymer phase by between

1 and 2 kcal/mol. However, the  $\Delta G^\ddagger$  increase in moving from the polymer to the MSTJ is significantly larger for **R(A)TTF<sup>4+</sup>** than for **RBPTTF<sup>4+</sup>** (2.5 vs. 4.1 kcal/mol). This difference may be related to the differences in packing between the Langmuir monolayers of the amphiphilic rotaxanes. Both monolayers were transferred onto the electrode-patterned substrate at a pressure of 30 mN/m. However, the **RTTF<sup>4+</sup>** rotaxanes occupy  $92 \pm 3 \text{ \AA}^2/\text{molecule}$ , while the **RBPTTF<sup>4+</sup>** rotaxanes occupy  $122 \pm 5 \text{ \AA}^2/\text{molecule}$ . Thus, the packing of **RBPTTF<sup>4+</sup>** is influenced by a combination of the high MSCC/GSCC ratio and the bulkier hydrophilic stopper. These differences lead to a 30% increase in the area/molecule over a similarly compressed film of **RTTF<sup>4+</sup>**. Nevertheless, for both amphiphilic, bistable rotaxanes, the data in figures 2-8 and 2-9 indicate a qualitatively similar switching mechanism, regardless of physical environment.

The thermodynamic data of figure 2-10a are apparently more reflective of the structural differences between **R(A)TTF<sup>4+</sup>** and **RBPTTF<sup>4+</sup>**, rather than the physical environment of these molecules. In all environments, **RBPTTF<sup>4+</sup>** exhibits a strongly temperature-dependent switching amplitude that can be related back to the temperature-dependence of the MSCC/GSCC ratio. In turn, this behavior can be connected to the free energy difference between the two host-guest complexes, **BPTTF-DEG $\subset$ CBPQT<sup>4+</sup>** and **DNP-DEG $\subset$ CBPQT<sup>4+</sup>**, and the fact that the enthalpic

contribution to the free energy is very different for these two complexes. The temperature dependence of the MSCC/GSCC ratio of **RBPTTF**<sup>4+</sup> is slightly more pronounced for the solution and polymer environments than for the MSTJ. This is likely due to the fact that the MSTJ constitutes a more sterically crowded environment. Nevertheless, the degree to which the free energy landscape of the bistable **RBPTTF**<sup>4+</sup> is reflected in the properties of this molecule, regardless of environment, is striking.

In a similar way, the temperature independent switching of **R(A)TTF**<sup>4+</sup> can also be rationalized within a self-consistent picture that connects across all environments as well as to the free energy differences between the **TTF-DEG**⊂**CBPQT**<sup>4+</sup> and **DNP-DEG**⊂**CBPQT**<sup>4+</sup> host-guest complexes. From the point of view of an MSTJ-based memory device, **RTTF**<sup>4+</sup> constitutes a much superior switch than does **RBPTTF**<sup>4+</sup>. First, it exhibits a stable switching amplitude over a reasonably broad temperature range. Second, an **RTTF**<sup>4+</sup>-based MSTJ remains in the high-conducting (MSCC-dominated) state 5 times longer than an **RBPTTF**<sup>4+</sup>-based MSTJ at 295 K, and 10 times longer at 320 K, implying a less volatile (and more useful) switch.

## 2.6 Conclusion

I have investigated two classes of bistable rotaxanes – one containing a TTF unit and the other a BPTTF unit – across different environments. Quantifying the relaxation rates in one critical step of the switching cycle enables us, not only to validate the proposed switching mechanism and its universality, but also to correlate switching kinetic rates with the nature of the environment. The trend in the kinetics and the validity of the switching mechanism are consistent and similar for both classes of bistable rotaxanes. Nevertheless, temperature-dependent thermodynamic measurements can reflect subtle differences between the various switching molecules. By replacing the TTF unit in the bistable rotaxanes with a BPTTF unit, the equilibrium MSCC/GSCC population ratio, which influences the low-conductance state in MSTJs, and the temperature sensitivity of this ratio, was altered considerably. Correspondingly, the switching amplitude between the high-conductance state and the now thermally-sensitive low-conductance state, changes significantly with temperature. Binding constant measurements for the complexation of model guests with the **CBPQT**<sup>4+</sup> host verify that the population ratio and its temperature sensitivity are likely related to the different binding strengths of the DEG-disubstituted TTF and BPTTF units. Enthalpy is found to play a crucial role in determining these binding strengths. To summarize these results, it is evident that the kinetics rates of the

molecular mechanical switching process are strongly influenced by both environment and molecular structure, while the thermodynamics values that describe the bistable nature of these molecular switches are relatively independent of environment, but strongly dependent upon molecular structure. This realization represents a key element in the emerging paradigm of molecular electronics.

## 2.7 References

1. Heath, J. R. & Ratner, M. A. (2003) *Physics Today* 56, 43-49.
2. McCreery, R. L. (2004) *Chem. Mater.* 16, 4477-4496
3. Nitzan, A. (2001) *Ann. Rev. Phys. Chem.* 52, 681-750.
4. Allara, D. L., Dunbar, T. D., Weiss, P. S., Bumm, L. A., Cygan, M. T., Tour, J. M., Reinerth, W. A., Yao, Y., Kozaki, M. & Jones, L. (1998) in *Molecular Electronics: Science and Technology*, Vol. 852, pp. 349-370.
5. Chen, J., Reed, M. A., Rawlett, A. M. & Tour, J. M. (1999) *Science* 286, 1550-1552.
6. Chen, Y., Jung, G. Y., Ohlberg, D. A. A., Li, X. M., Stewart, D. R., Jeppesen, J. O., Nielsen, K. A., Stoddart, J. F. & Williams, R. S. (2003) *Nanotechnology* 14, 462-468.
7. Donhauser, Z. J., Mantooth, B. A., Kelly, K. F., Bumm, L. A., Monnell, J. D.,

- Stapleton, J. J., Price, D. W., Rawlett, A. M., Allara, D. L., Tour, J. M. & Weiss, P. S. (2001) *Science* 292, 2303-2307.
8. Dunbar, T. D., Cygan, M. T., Bumm, L. A., McCarty, G. S., Burgin, T. P., Reinerth, W. A., Jones, L., Jackiw, J. J., Tour, J. M., Weiss, P. S. & Allara, D. L. (2000) *J. Phys. Chem. B* 104, 4880-4893.
9. Kornilovitch, P. E., Bratkovsky, A. M. & Williams, R. S. (2002) *Phys. Rev. B* 66, 165436.
10. Lee, I. C. & Frank, C. W. (2004) *Langmuir* 20, 5809-5828.
11. McConnell, H. (1961) *J. Chem. Phys.* 35, 508-515.
12. Polymeropoulos, E. E. & Sagiv, J. (1978) *J. Chem. Phys.* 69, 1836-1847.
13. Richter, C. A., Stewart, D. R., Ohlberg, D. A. A. & Williams, R. S. (2005) *Appl. Phys. A - Mat. Sci. & Proc.* 80, 1355-1362.
14. Smalley, J. F., Sachs, S. B., Chidsey, C. E. D., Dudek, S. P., Sikes, H. D., Creager, S. E., Yu, C. J., Feldberg, S. W. & Newton, M. D. (2004) *J. Am. Chem. Soc.* 126, 14620-14630.
15. Vincett, P. S. & Roberts, G. G. (1980) *Thin Solid Films* 68, 135-171.
16. Aviram, A. & Ratner, M. A. (1974) *Chem. Phys. Lett.* 29, 277-283.
17. Ashwell, G. J. & Gandolfo, D. S. (2001) *J. Mat. Chem.* 11, 246-248.
18. Ashwell, G. J., Gandolfo, D. S. & Hamilton, R. (2002) *J. Mat. Chem.* 12, 416-

- 420.
19. Ashwell, G. J., Gandolfo, D. S. & Hamilton, R. (2002) *J. Mat. Chem.* 12, 416-420.
  20. Ashwell, G. J., Sambles, J. R., Martin, A. S., Parker, W. G. & Szablewski, M. (1990) *J. Chem.Soc.-Chem. Comm.* 1374-1376.
  21. Ashwell, G. J., Tyrrell, W. D. & Whittam, A. J. (2004) *J. Am. Chem. Soc.* 126, 7102-7110.
  22. Chang, S. C., Li, Z. Y., Lau, C. N., Larade, B. & Williams, R. S. (2003) *Appl. Phys. Lett.* 83, 3198-3200.
  23. Ho, G., Heath, J. R., Kondratenko, M., Perepichka, D. F., Arseneault, K., Pezolet, M. & Bryce, M. R. (2005) *Chem. Eur. J.* 11, 2914-2922.
  24. Krebs, F. C., Spanggaard, H., Rozlosnik, N., Larsen, N. B. & Jorgensen, M. (2003) *Langmuir* 19, 7873-7880.
  25. Lau, C. N., Stewart, D. R., Williams, R. S. & Bockrath, M. (2004) *Nano Lett.* 4, 569-572.
  26. Maruccio, G., Cingolani, R. & Rinaldi, R. (2004) *J. Mat. Chem.* 14, 542-554.
  27. Metzger, R. M. (1999) *Acc. Chem. Res.* 32, 950-957.
  28. Metzger, R. M. (2003) *Chem. Rev.* 103, 3803-3834.
  29. Metzger, R. M., Chen, B., Hopfner, U., Lakshmikantham, M. V., Vuillaume,

- D., Kawai, T., Wu, X. L., Tachibana, H., Hughes, T. V., Sakurai, H., Baldwin, J. W., Hosch, C., Cava, M. P., Brehmer, L. & Ashwell, G. J. (1997) *J. Am. Chem. Soc.* 119, 10455-10466.
30. Metzger, R. M., Xu, T. & Peterson, I. R. (2001) *J. Phys. Chem. B* 105, 7280-7290.
31. Ng, M. K. & Yu, L. P. (2002) *Angew. Chem. Int. Ed.* 41, 3598-3601.
32. Stewart, D. R., Ohlberg, D. A. A., Beck, P. A., Chen, Y., Williams, R. S., Jeppesen, J. O., Nielsen, K. A. & Stoddart, J. F. (2004) *Nano Lett.* 4, 133-136.
33. Shipway, A. N. & Willner, I. (2001) *Acc. Chem. Res.* 34, 421-432.
34. Collier, C. P., Jeppesen, J. O., Luo, Y., Perkins, J., Wong, E. W., Heath, J. R. & Stoddart, J. F. (2001) *J. Am. Chem. Soc.* 123, 12632-12641.
35. Collier, C. P., Mattersteig, G., Wong, E. W., Luo, Y., Beverly, K., Sampaio, J., Raymo, F. M., Stoddart, J. F. & Heath, J. R. (2000) *Science* 289, 1172-1175.
36. Luo, Y., Collier, C. P., Jeppesen, J. O., Nielsen, K. A., DeLonno, E., Ho, G., Perkins, J., Tseng, H. R., Yamamoto, T., Stoddart, J. F. & Heath, J. R. (2002) *Chemphyschem* 3, 519-525.
37. Diehl, M. R., Steurman, D. W., Tseng, H. R., Vignon, S. A., Star, A., Celestre, P. C., Stoddart, J. F. & Heath, J. R. (2003) *Chemphyschem* 4, 1335-1339.
38. Yu, H. B., Luo, Y., Beverly, K., Stoddart, J. F., Tseng, H. R. & Heath, J. R.

- (2003) *Angew. Chem. Int. Ed.* 42, 5706-5711.
39. Steuerman, D. W., Tseng, H. R., Peters, A. J., Flood, A. H., Jeppesen, J. O., Nielsen, K. A., Stoddart, J. F. & Heath, J. R. (2004) *Angew. Chem. Int. Ed.* 43, 6486-6491.
40. Flood, A. H., Peters, A. J., Vignon, S. A., Steuerman, D. W., Tseng, H. R., Kang, S., Heath, J. R. & Stoddart, J. F. (2004) *Chem. Eur. J.* 10, 6558-6564.
41. Tseng, H. R., Wu, D. M., Fang, N. X. L., Zhang, X. & Stoddart, J. F. (2004) *Chemphyschem* 5, 111-116.
42. Jeppesen, J. O., Nielsen, K. A., Perkins, J., Vignon, S. A., Di Fabio, A., Ballardini, R., Gandolfi, M. T., Venturi, M., Balzani, V., Becher, J. & Stoddart, J. F. (2003) *Chem. Eur. J.* 9, 2982-3007.
43. Jeppesen, J. O., Perkins, J., Becher, J. & Stoddart, J. F. (2001) *Angew. Chem. Int. Ed.* 40, 1216-1221.
44. Jeppesen, J. O., Takimiya, K., Jensen, F., Brimert, T., Nielsen, K., Thorup, N. & Becher, J. (2000) *J. Org. Chem.* 65, 5794-5805.
45. Kang, S. S., Vignon, S. A., Tseng, H. R. & Stoddart, J. F. (2004) *Chem. Eur. J.* 10, 2555-2564.
46. Tseng, H. R., Vignon, S. A., Celestre, P. C., Perkins, J., Jeppesen, J. O., Di Fabio, A., Ballardini, R., Gandolfi, M. T., Venturi, M., Balzani, V. & Stoddart,

- J. F. (2004) *Chem. Eur. J.* 10, 155-172.
47. Yamamoto, T., Tseng, H. R., Stoddart, J. F., Balzani, V., Credi, A., Marchioni, F. & Venturi, M. (2003) *Col. Czech. Chem. Comm.* 68, 1488-1514.
48. Katz, E., Lioubashevsky, O. & Willner, I. (2004) *J. Am. Chem. Soc.* 126, 15520-15532.
49. Long, B., Nikitin, K. & Fitzmaurice, D. (2003) *J. Am. Chem. Soc.* 125, 15490-15498.
50. Ryan, D., Rao, S. N., Rensmo, H., Fitzmaurice, D., Preece, J. A., Wenger, S., Stoddart, J. F. & Zaccheroni, N. (2000) *J. Am. Chem. Soc.* 122, 6252-6257.
51. Alteri, A., Gatti, F. G., Kay, E. R., Leigh, D. A., Martel, D., Paolucci, F., Slawin, A. M. Z. & Wong, J. K. Y. (2003) *J. Am. Chem. Soc.* 125, 8644-8654.
52. Altieri, A., Bottari, G., Dehez, F., Leigh, D. A., Wong, J. K. Y. & Zerbetto, F. (2003) *Angew. Chem. Int. Ed.* 42, 2296-2300.
53. Brouwer, A. M., Frochot, C., Gatti, F. G., Leigh, D. A., Mottier, L., Paolucci, F., Roffia, S. & Wurpel, G. W. H. (2001) *Science* 291, 2124-2128.
54. Cecchet, F., Rudolf, P., Rapino, S., Margotti, M., Paolucci, F., Baggerman, J., Brouwer, A. M., Kay, E. R., Wong, J. K. Y. & Leigh, D. A. (2004) *J. Phys. Chem. B* 108, 15192-15199.
55. Collin, J. P., Gavina, P. & Sauvage, J. P. (1997) *New J. Chem.* 21, 525-528.

56. Livoreil, A., Dietrichbuechecker, C. O. & Sauvage, J. P. (1994) *J. Am. Chem. Soc.* 116, 9399-9400.
57. Poleschak, I., Kern, J. M. & Sauvage, J. P. (2004) *Chem. Comm.*, 474-476.
58. Raehm, L., Kern, J. M. & Sauvage, J. P. (1999) *Chem. Eur. J.* 5, 3310-3317.
59. Norgaard, K., Jeppesen, J. O., Laursen, B. A., Simonsen, J. B., Weygand, M. J., Kjaer, K., Stoddart, J. F. & Bjornholm, T. (2005) *J. Phys. Chem. B* 109, 1063-1066.
60. Laursen, B. W., Nygaard, S., Jeppesen, J. O. & Stoddart, J. F. (2004) *Org. Lett.* 6, 4167-4170.
61. Deng, W. Q., Muller, R. P. & Goddard, W. A. (2004) *J. Am. Chem. Soc.* 126, 13562-13563.
62. Kim, Y. H., Jang, S. S., Jang, Y. H. & Goddard, W. A. (2005) *Phys. Rev. Lett.* 94, 156801.
63. Houk, K. N., Menzer, S., Newton, S. P., Raymo, F. M., Stoddart, J. F. & Williams, D. J. (1999) *J. Am. Chem. Soc.* 121, 1479-1487.
64. Raymo, F. M., Bartberger, M. D., Houk, K. N. & Stoddart, J. F. (2001) *J. Am. Chem. Soc.* 123, 9264-9267.
65. Blandamer, M. J., Cullis, P. M. & Engberts, J. (1998) *J. Chem. Soc. - Far. Trans.* 94, 2261-2267.

66. Ashton, P. R., Ballardini, R., Balzani, V., Boyd, S. E., Credi, A., Gandolfi, M. T., GomezLopez, M., Iqbal, S., Philp, D., Preece, J. A., Prodi, L., Ricketts, H. G., Stoddart, J. F., Tolley, M. S., Venturi, M., White, A. J. P. & Williams, D. J. (1997) *Chem. Eur. J.* 3, 152-170.
67. Ashton, P. R., Balzani, V., Becher, J., Credi, A., Fyfe, M. C. T., Mattersteig, G., Menzer, S., Nielsen, M. B., Raymo, F. M., Stoddart, J. F., Venturi, M. & Williams, D. J. (1999) *J. Am. Chem. Soc.* 121, 3951-3957.
68. Nielsen, M. B., Jeppesen, J. O., Lau, J., Lomholt, C., Damgaard, D., Jacobsen, J. P., Becher, J. & Stoddart, J. F. (2001) *J. Org. Chem.* 66, 3559-3563.
69. Castro, R., Nixon, K. R., Evanseck, J. D. & Kaifer, A. E. (1996) *J. Org. Chem.* 61, 7298-7303.
70. Iwamoto, M. & Wu, C. X. (1997) *Phys. Rev. E* 56, 3721-3724.

## Chapter 3

### Molecular Electronic Crossbar Memory Circuits

#### 3.1 Introduction

In chapter 2, I described the fabrication procedures for molecular switch tunnel junction (MSTJ) device at a single device level and also proved that bistable [2]rotaxane plays a crucial role in a decent conductance switching. The [2]rotaxane molecular switches hold several advantages over more traditional switching components such as ferroelectric (1) and ferromagnetic materials (2). However, a key application of these molecular switches is related to the extreme scaling of electronic circuitry to near molecular dimensions: since conductance switching within an MSTJ originates from the electrochemically driven molecular mechanical isomerization of the molecules, the switching relies purely on individual molecular properties. In both molecular dynamics (MD) and electrochemical investigations (3-5), the two molecular co-conformers are characterized by different HOMO-LUMO gaps, and therefore different tunneling probabilities (6, 7). By contrast, the switching of solid state materials such as ferroelectrics involves altering the polarization state of the crystallographic lattice upon the application of an external electric field. This polarization disappears for domains below a certain critical size. An analogous

phenomenon is the transition from ferromagnetic behavior to superparamagnetic behavior for magnetics, as the size of the ferromagnetic material is reduced. Therefore, these devices have a critical limitation in the scale-down. Second, solid state material switching depends upon a field-driven nucleation process and can be statistical in nature, especially for small crystallographic domain sizes. The molecular switches discussed in this thesis, by contrast, switch based upon electrochemical processes. These are current and voltage driven, and depend upon molecular properties such as redox potentials, molecular orbital energies, etc. Therefore, switching voltages for the ferroelectric device could vary from junction to junction, or during many cycles. In particular, at a smaller dimension, the reliability issues are expected to be more serious. When the solid state materials are integrated into a 2D crossbar circuit that is a main architecture of the memory devices described here, their irregular switching characteristic will cause an additional problem, that is, 'a half select issue' (8). In the crossbar memory circuit, a switching voltage,  $V_A$ , is split into two components,  $+\frac{1}{2}V_A$  and  $-\frac{1}{2}V_A$ , which are then applied to the top and bottom electrodes that define a designated cross-junction. As all of the junctions are interconnected in a crossbar circuit, every junction is subject to at least some field. For the case of the solid state materials, the field generated by  $\pm \frac{1}{2}V_A$  is occasionally sufficient to perturb the state

of the nucleation event. This half-select problem is considered as a generic problem for the field-poled devices that function within a 2D crossbar circuit.

Taking advantage of the switching molecules, the next challenge is to integrate those switching molecules and electrodes into fully functional circuits, patterned at nanometer dimensions. When such a memory circuit is combined with other nanoscale functional circuits such as logic and routing, computing at nanometer dimensions, which is currently unachievable with standard CMOS technology, could be realized. Entire circuits for nanoscale computing were proposed as conceptualized in figure 3-1. While efforts in my research group have focused on developing and integrating the various components of this nano-computer (8-11), this chapter will address fabrication and testing of crossbar memory circuits exclusively.

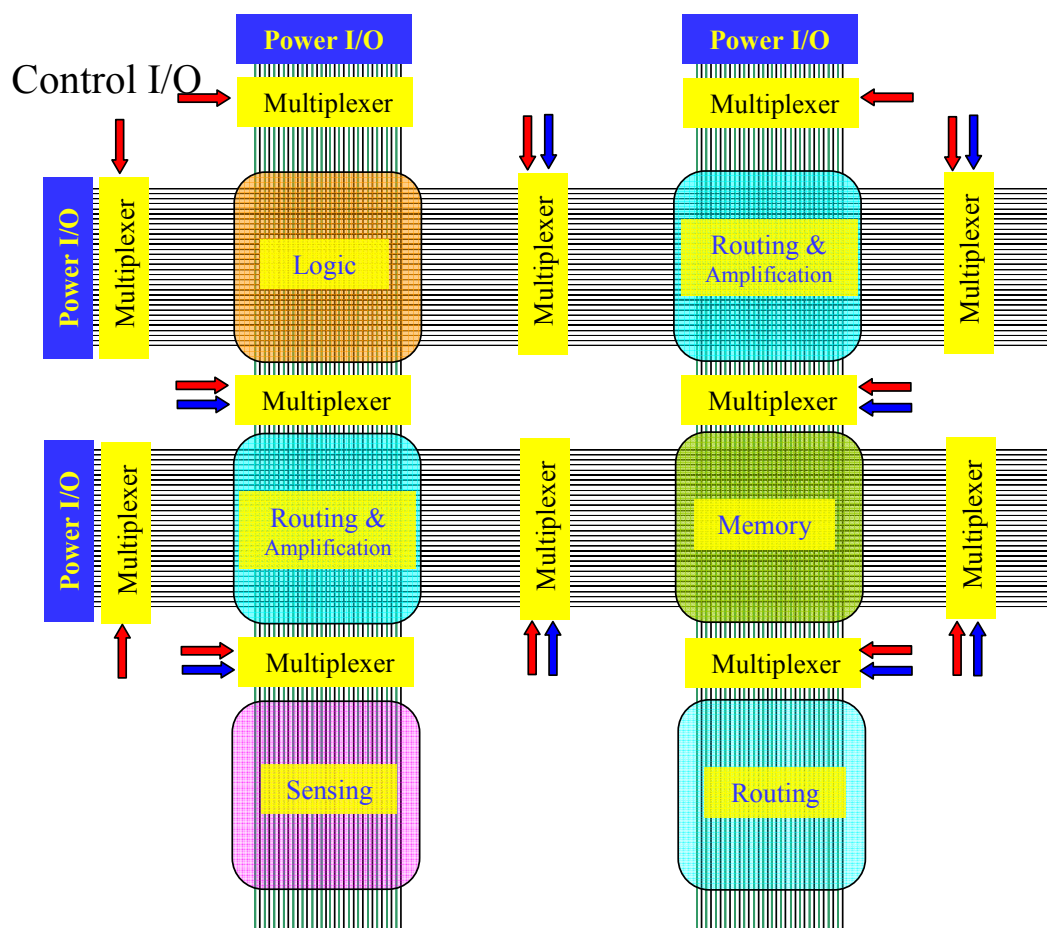


**Figure 3-1.** A nanoscale molecular computational platform. Traditional computing functions are coupled to non-traditional elements, including sensors, actuator, etc., and are illustrated as individual tiles in a mosaic-like architecture. Multiplexers and demultiplexers control communication between various functions and provide the user interfaces. Copyright 2006 Royal Society of Chemistry.

As presented in figure 3-1, the proposed computing platform is based on the crossbar architecture. The crossbar geometry (12) provides a promising architecture for nanoelectronic circuitry (13-17). The crossbar is tolerant of manufacturing defects – a trait that becomes increasingly important as devices approach macromolecular

dimensions and non-traditional (and imperfect) fabrication methods are employed. For example, Teramac had nearly a quarter million hardware defects and yet could be configured into a robust computing machine (12). The crossbar is a periodic array of crossed wires, similar to a two-dimensional crystal, implying that non-traditional methods can be employed for its construction (18-20). Finally, the crossbar is the highest density, two-dimensional digital circuit for which every device can be independently addressed (12). This attribute enables the circuit to be fully tested for manufacturing defects and to be subsequently configured into a working circuit.

For these reasons, my research group has tried to utilize the crossbar architecture for memory circuits. The progress in this crossbar memory project has been made both in the switching molecules and in the contacting electrodes: more robust [2]rotaxanes with higher on/off ratios have been rationally designed and synthesized (21). At the same time, as an attempt to constitute a circuit with higher density, various electrode-patterning techniques have been developed and tested. In practice, the total number of bits fabricated within a single crossbar circuit increased from 16 to 64 (8) to 4,500 to 160,000 bits as the main electrode patterning techniques were improved from photo-lithography to electron-beam lithography (EBL) to recently developed nanowire array technique (11) (figure 3-2) , and as methods to increase the compatibility of our nanofabrication procedures with the molecular

switch components were improved. Notably, the resolution of the nanowire array (11) that has been developed by my research group is far beyond that of the conventional EBL. Hence, the memory circuits utilizing this nanowire array technique set a remarkable landmark in memory bit density. In this chapter, I will first describe the nanowire array technique, so called superlattice nanowire pattern transfer (SNAP) method, and then focus on fabrication and testing of 160 kbit crossbar memory circuits based on the SNAP technique and [2]rotaxanes.

The fabrication of the 160 kbit memory circuits at a bit density of  $10^{11}$  bits/cm<sup>2</sup> was totally nontrivial. At this point, reviewing the history of molecular memory projects in my research group provides guidance for understanding our efforts toward device miniaturization, as well as understanding difficulties of the fabrication procedure. Until reaching this unexplored bit density, many scientists from several groups have contributed to different components of the circuits at each stage: In conjunction with Hewlett-Packard group, my research group initially proposed the concept of the defect-tolerant crossbar architecture. Since then, significant progresses in achieving the actual molecule-based devices were initiated by the former postdocs in my research group, Dr. Collier, Dr. Wong and Dr. Luo. They optimized conditions for many of the key fabrication steps, including monolayer deposition by the Langmuir-Blodgett technique and metal deposition to form the top electrical contact

to the molecules. They also established rational electrical measurement schemes such as the remnant molecular signature scan and the temperature-dependent volatility scan to test the switching and the activated nature of the molecular electronic switching mechanism. They also demonstrated relative robust molecular switches that could be cycled  $> 1,000$  times. Dr. Luo developed next-generation fabrication procedures for the memory circuits based on the EBL-defined electrodes. He demonstrated that the molecular switching in EBL-defined circuits is still very robust, and he developed a number of procedures for the integration of Si SNAP nanowire bottom electrode arrays with EBL defined top electrodes. For my part, I was teamed up with another group member, Jonathan Green, to achieve the large-scale (160,000 bit) SNAP nanowire-based memory circuits at extreme density ( $10^{11}$  bits $\text{cm}^{-2}$ ).

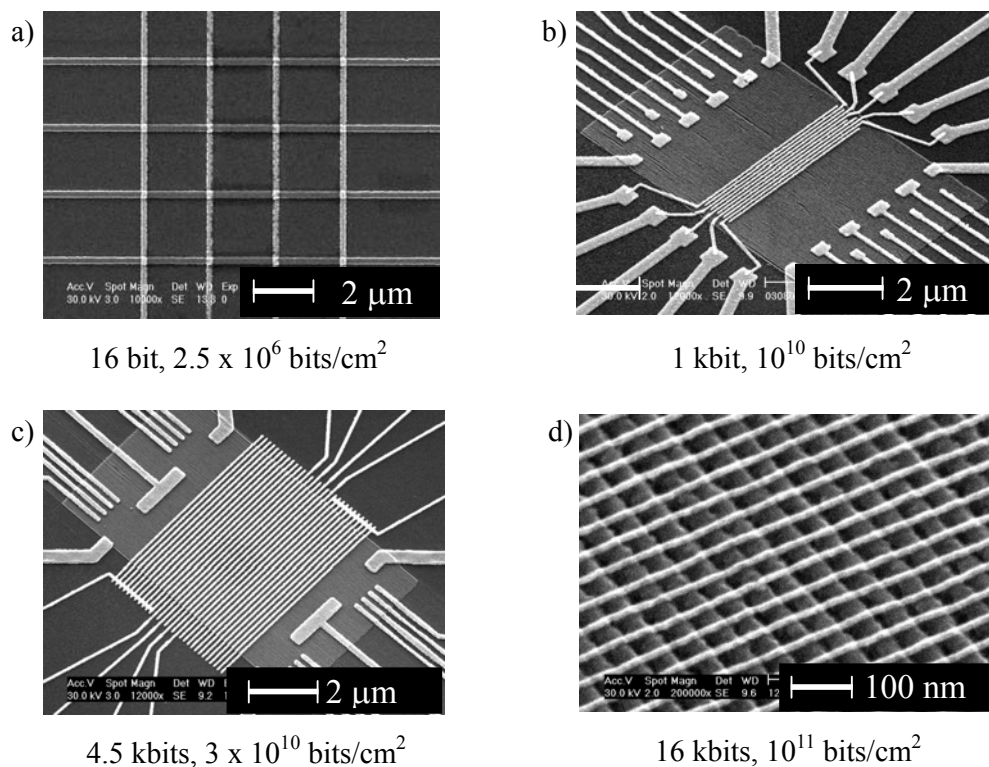


**Figure 3-2.** A series of crossbar molecular electronic memory circuits. These circuits are arranged a-d in accordance with the chronology of their fabrication. The total number of bits and the memory density of each memory circuit were denoted below scanning electron micrograph (SEM) pictures.

### 3.2 Superlattice Nanowire Pattern Transfer (SNAP) Method

As described in the previous subchapter, the scaling advantage of a [2]rotaxane molecular electronic switch would be best illustrated only when electrodes with molecular dimensions are integrated together to form the junction sandwiching the molecule. For this and other reasons, my research group has

developed unique nanowire array fabrication technique called superlattice nanowire pattern transfer (SNAP). For the SNAP method, the layer structure of a GaAl/Al<sub>x</sub>Ga<sub>(1-x)</sub>As superlattice in which each layer is grown under atomic-level control, is translated into a variety of metals or silicon. The width and pitch of final nanowire array made of metals and/or silicon are defined by the initial superlattice film widths and spacings. With the SNAP method, my research group has demonstrated the fabrication of silicon nanowire arrays in which each wire is about 8 nm wide and at a pitch of about 16 nm. Also, nanowire arrays containing up to 1,400 nanowires have been demonstrated (figure 3-3). Moreover, in comparison to other nanowire growth methods, such as the vapor-liquid-solid growth method most fully developed in the Lieber group (22), the SNAP method has no limitation in length of the nanowires within arrays. A few millimeter long nanowire arrays are routinely produced.

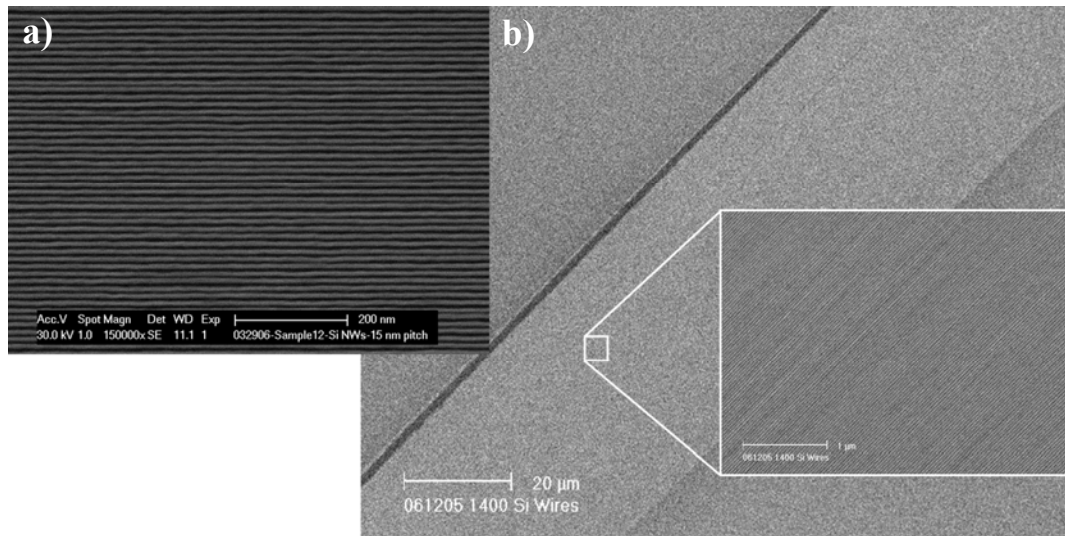


**Figure 3-3.** SEM images of Si nanowire arrays of (a) 15 nm pitch and (b) 1400 wires.

Here, I briefly go through the SNAP procedures (figure 3-4). More detailed procedures of the SNAP method are described in the thesis of Jonathan Green, who was also involved in the project as a leading member. First, a wafer containing the superlattice was diced into small pieces, which are referred to as masters. When turned on its side, a master is largely a GaAs wafer, with the top edge of the wafer containing the superlattice. When viewed from the edge, this superlattice structure is like a club sandwich, with alternating layers of GaAs and  $\text{Al}_x\text{Ga}_{(1-x)}\text{As}$  films substituting for the meat and bread layers in the sandwich. It is this superlattice edge that provides the initial template for the nanowires. This edge is first cleaned carefully in a class 1000 clean room using methanol and gentle swabbing, so that it is clean by eye when viewed under an optical microscope. Once the cross-section turns out to be

completely dust-free, a dilute mixture of buffered hydrofluoric acid (15 ml of 6:1 buffered oxide etchant, 50 ml of H<sub>2</sub>O) is used to selectively etch the Al<sub>x</sub>Ga<sub>(1-x)</sub>As, thus forming a comb-like structure as shown in figure 3-4b. Conversely, the GaAs could be selectively etched to form a complementary comb-like structure. Next, about 10 nm of Pt layer was deposited onto the superlattice side at about 45° tilted angle using electron beam evaporation of a Pt target. This angle could be varied to yield some control over the nanowire width. In preparing silicon substrates (using silicon-on-insulator wafers), the substrates were cleaned by rinsing with a series of solvents until the surface becomes completely dust-free. A mixture of epoxy and poly (methyl methacrylate) (PMMA) (10 drops of epoxy and 1 drop of curing agent, 0.18 g of 6 % (in weight) PMMA in chlorobenzene, additional 10 ml of chlorobenzene) was spincoated onto prepared substrates at 8000 rpm. Pt deposited masters were dropped onto the epoxy coated substrates so that the superlattice side contacted and adhered to the epoxy layer. The epoxy was cured around 130 °C for half an hour or so. The substrates were then dipped into an etching solution for removing GaAs masters, but leaving behind the Pt nanowires, which were epoxy-adhered to the substrate. After ~ 4 hr of wet-etching, the GaAs masters were peeled off and the Pt nanowire array structure remained on the substrate. Once the quality of the Pt nanowire array was confirmed by SEM, the Pt pattern was transferred into the underlying silicon-on-

insulator substrate by reactive ion etching (RIE) ( $\text{CF}_4:\text{He} = 20:30$  sccm, 5 mTorr, 40 W,  $\sim 4$  min for 33 nm Si layer). Upon removing Pt by aqua regia ( $\text{HCl}:\text{HNO}_3 = 2:1$  in volume), the Si nanowire array structure was complete.

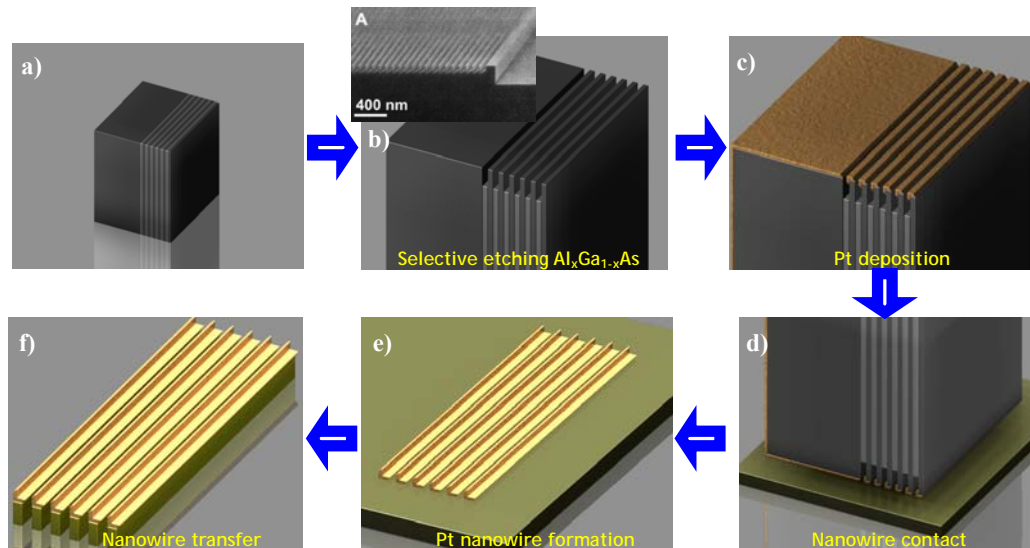


**Figure 3-4.** SNAP process flow. (a) The wafer containing the superlattice was diced into small pieces and the superlattice side was cleaned thoroughly. (b)  $\text{Al}_x\text{Ga}_{(1-x)}\text{As}$  was selectively wet-etched. (c) A Pt layer was deposited onto the superlattice side by electron beam evaporation. (d) Masters were dropped onto the epoxy coated substrates. (e) The superlattice was removed by a wet-etch, leaving the Pt nanowire-array structure on the substrates. (f) The Pt nanowire array structure was transferred to form an array of aligned and high aspect ratio silicon nanowires via RIE.

### 3.3 160 kbit Molecular Electronic Memory Circuits: Overview

The primary metric for gauging progress in the various semiconductor integrated circuit (IC) technologies is the spacing, or pitch, between the most closely spaced wires within a dynamic random access memory (DRAM) circuit (23). Modern DRAM circuits have 140 nanometer (nm) pitch wires and a memory cell size of 0.0408 square micrometers ( $\mu\text{m}^2$ ). Improving IC technology will require that these dimensions decrease over time. However, by year 2013 a large fraction of the patterning and materials requirements for constructing IC technologies are currently classified as having ‘no known solution’ (23). Nanowires (24), molecular electronics (25), and defect tolerant architectures (12) have been identified as materials, devices, and concepts that might assist in continuing IC advances. This belief has largely been bolstered by single device (26-28) or small circuit demonstrations (20, 29). The science of extending such demonstrations to large scale, high density circuitry is largely undeveloped. In this and following sections, I describe a 160,000 bit molecular electronic memory circuit, fabricated at a density of  $10^{11}$  bits/cm<sup>2</sup> (pitch = 33 nm; memory cell size =  $0.0011 \mu\text{m}^2$ ), which is roughly analogous to a projected year 2020 DRAM circuit. A monolayer of bistable, [2]rotaxane molecules (30) described in chapter 2 served as the data storage elements. Although the circuit had large numbers of defects, those defects could be readily identified through electronic

testing and isolated using software coding. The working bits were then configured to form a fully functional random access memory circuit for storing and retrieving information.

A few groups have reported on non-lithographic methods for fabricating crossbar circuits (18, 31), but most methods are not yet feasible for fabricating more than a handful of devices. Furthermore, the assembly of nanowires into narrow pitch crossbars without electrically shorting adjacent nanowires remains a challenge. Despite these challenges, my research group developed the SNAP method for producing ultra-dense, highly aligned arrays of high-aspect ratio metal or semiconductor NWs(11) containing up to 1400 NWs at a pitch as small as 15 nm (figure 3-3). The procedures for this SNAP method were described in the previous subchapter. For constituting ultra-dense memory circuits whose density is far beyond what is possible with current CMOS technology , I combined these patterning methods and extremely scalable [2]rotaxane switches, along with the defect-tolerance concepts learned from Teramac. I constructed and tested a memory circuit at extreme dimensions: the entire 160,000 bit crossbar is approximately the size of a white blood cell ( $\sim 13 \times 13 \mu\text{m}^2$ ). At each cross-point of nanowire array, only several hundreds of [2]rotaxanes were incorporated.

### **3.4 160 kbit Molecular Electronic Memory Circuits: Fabrication Flow**

A bottom-up approach was the key to the successful fabrication of this memory. This approach both minimized the number of processing steps following deposition of the molecular monolayer, as well as protected the molecules from remaining processing steps. In the following paragraphs, I describe the nanofabrication procedures utilized to construct the memory circuit.

Our 160,000 junction crossbar memory consists of 400 Si nanowire (NW) bottom electrodes of 16 nm width and 16.5 nm half-pitch, crossed with 400 Ti NW top electrodes of the same dimensions, and with a monolayer of bistable [2]rotaxane molecules sandwiched in between. My research group has previously reported on using the SNAP technique to fabricate highly ordered arrays of 150 metal and Si NWs (10). For this work, the SNAP technique was extended to create 400 element NW arrays of both the bottom and top electrode materials, and so was the primary patterning method for achieving the  $10^{11}$  cm<sup>-2</sup> bit density of the crossbar.

An overview of the process flow used to fabricate the memory is shown in figure 3-5.

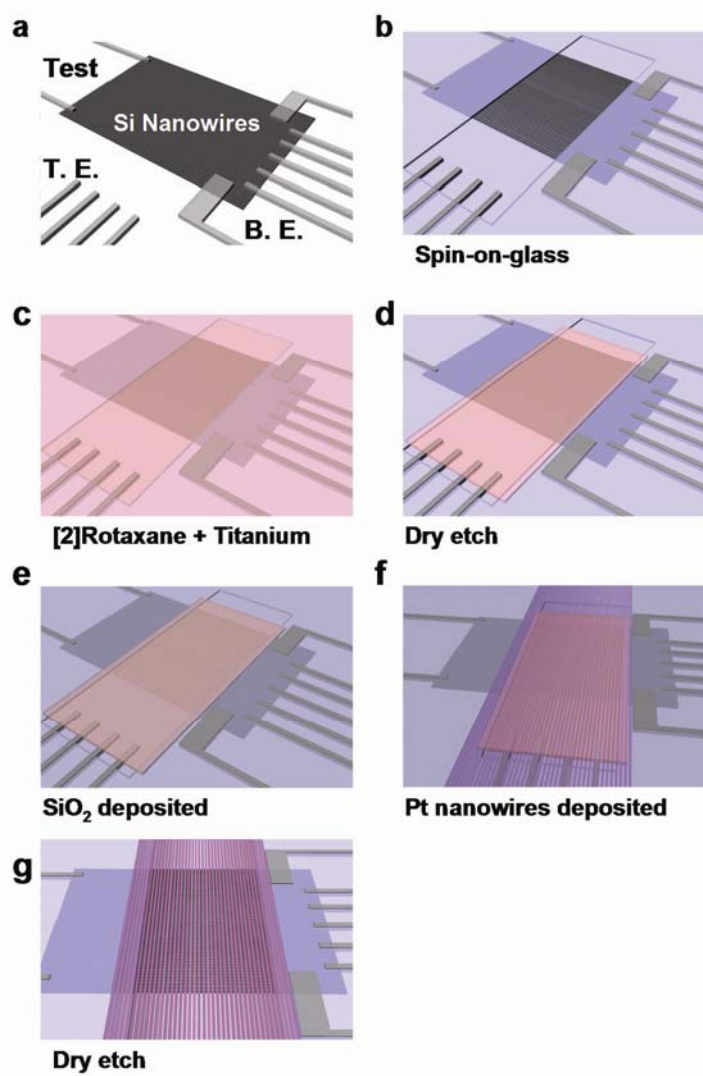


**Figure 3-5.** The process flow for preparing the 160 kbit molecular electronic memory circuit at  $10^{11}$  bits/cm<sup>2</sup>. (a) SNAP-patterned SiNW bottom electrodes are electrically contacted to metal electrodes. (b) The entire circuit is coated with SiO<sub>2</sub> (using spin-on-glass (SOG)) and the active memory region is exposed using lithographic patterning followed by dry etching. (c) The bistable [2] rotaxane Langmuir monolayer is deposited on top of the Si NWs and then protected via the deposition of a Ti layer. (d) The molecule/Ti layer is etched everywhere except for the active memory region. (e) A SiO<sub>2</sub> insulating layer is deposited on top of the Ti film. (f) An array of top Pt NWs is deposited at right angle to the bottom Si NWs using the SNAP method. (g) The Pt NW pattern is transferred, using dry etching, to the Ti layer to form an array of

top Ti NW electrodes, and the crossbar structure is complete.

***Preparation of and contact to the bottom Si nanowire electrodes*** The Si NW array was fabricated as described previously (10, 11). The starting wafer for the Si NWs was a 33 nm thick phosphorous doped ( $n=5 \times 10^{19} \text{ cm}^{-3}$ ) silicon-on-insulator (SOI) substrate with a 250 nm thick buried oxide (Simgui, Shanghai, China). An array of Pt NWs was transferred onto this substrate using the SNAP method, and reactive ion etching was used to transfer the Pt NW pattern to form a  $\sim 2$  millimeter long array of Si NWs. The Pt NWs were then removed, and the Si NW array was sectioned into a 30  $\mu\text{m}$  long region. Electrical contacts to these bottom Si NWs, as well as contacts that are intended for the top Ti NWs were defined at this point using standard electron-beam lithography (EBL) patterning and electron-beam evaporation to produce electrodes consisting of a 15 nm Ti adhesion layer followed by a 50 nm thick Pt electrode (figure 3-5a). Immediately prior to metal evaporation, the Si NWs were cleaned using a gentle  $\text{O}_2$  plasma (20 standard cubic centimeters per minute (sccm), 20 milli Torr, 10 Watts, 30 seconds) followed by a 5 second dip in an  $\text{NH}_4\text{F}/\text{HF}$  solution. After lift-off, the chip was annealed at 450  $^\circ\text{C}$  in  $\text{N}_2$  for 5 min to promote the formation of ohmic contacts.

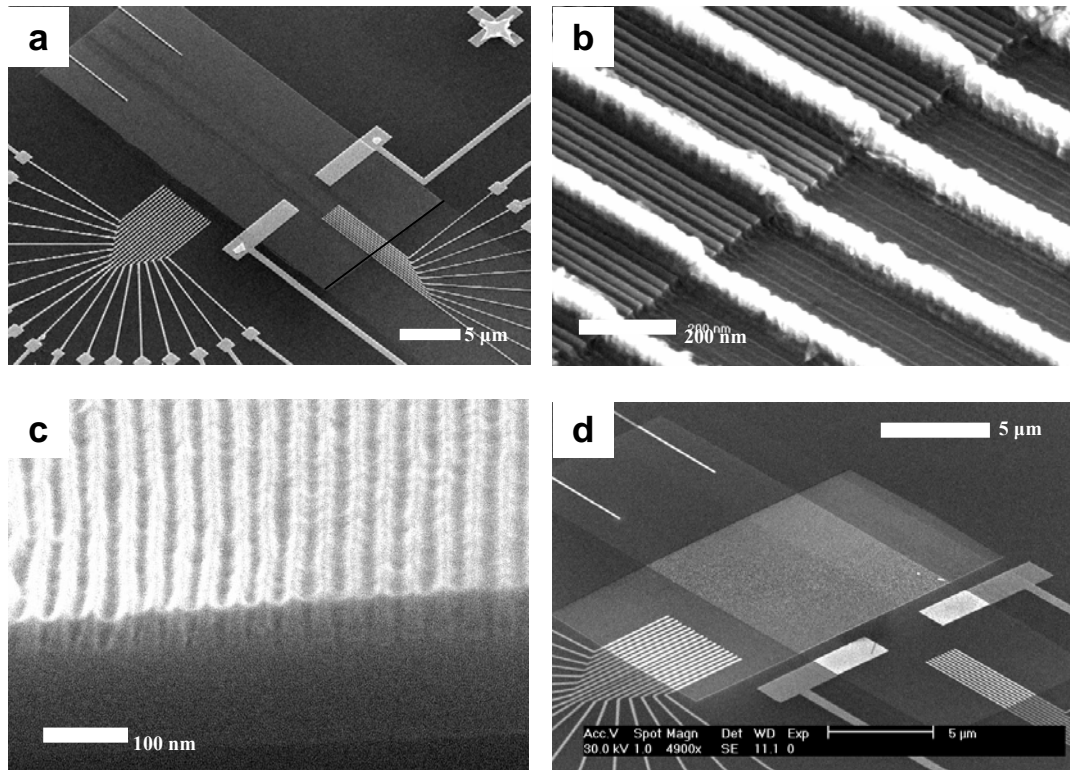


**Figure 3-6.** Scanning electron micrographs of the nanowire crossbar memory fabrication process. (a) A 30 micrometer long section of the SiNWs and its electrical contacts to metal leads were defined by electron-beam lithography (EBL). (b) Each electrode defined by EBL is about 70 nm wide contacting 2 ~ 4 NWs. This image illustrates that the intrinsic patterning of nanowire crossbar is beyond lithographic limits. (c) Progress-check of SOG window etching over the active memory region. This image verifies that SOG fills the gap of NWs and SEM is a valid tool for monitoring SOG etching. (d) SOG is etched by RIE over the active memory region. Detailed processes for monitoring this etching progress are described in the text.

Figure 3-6a shows an SEM image of the device at the stage in which the Si NWs and all of the external electrical contacts have been created. Note that there are four sets of EBL defined contacts. The 18 narrow contacts at the bottom left of the

image will eventually connect to the top Ti NW electrodes and are used for testing of the final memory circuit. The 10 narrow contacts to the Si NWs at the bottom right of the image are also used for testing of the memory circuit. Finally there are two narrow test electrodes at the top left and two wide electrodes at the bottom right. The wide electrodes contact about  $2/3$  of all the Si NWs and serve dual functions. First, they ground unused Si NWs during memory testing (this procedure approximates how a fully multiplexed crossbar circuit would be utilized). Second, when used in conjunction with the two narrow test-electrodes on the opposite side of Si NW array, they enable testing of the conductivity of the Si NWs throughout the fabrication processes. This testing procedure provided invaluable feedback for finely tuning and tracking many of the fabrication processes. Once these various contacts were established, robust Si NW conductivity was confirmed via current vs. voltage measurements. If the Si NWs were measured to be poor conductors (a very infrequent occurrence), the chip was discarded.

The device was then planarized using an optimized spin-on-glass (SOG) procedure (Accuglass 214, Honeywell Electronic Materials, Sunnyvale, CA). This planarization process was critical because the SOG not only protects Si NWs outside of the active memory region from damage that can arise during subsequent processing steps, but it also prevents evaporated Ti (explained below) from entering the gaps

between the Si NWs where it would be extremely difficult to remove (figure 3-6c). Due to the extremely narrow gap between the Si NWs, this SOG step was performed in a vacuum condition: For the first generation of the devices, the SOG was spin-coated at atmospheric pressure. However, the atmospheric spin-coating did not allow the gaps between the Si NWs to be filled completely with the SOG. The SOG penetrated only to the upper spacing of the trenches. For the complete filling, the process was done in a vacuum condition. The substrate containing the Si NWs was placed in a small glass container covered by a rubber stopper. A needle connected to a syringe and to a diffusion pump was plugged through the rubber stopper to employ a vacuum condition. During this vacuum process, the SOG was transferred to the container via another syringe. As soon as the SOG was sucked into the container by the vacuum and therefore the substrate was covered by the SOG, the substrate was taken out immediately for a spin-coating (~ 5000 rpm, 30 sec). Before starting the planarization steps described so far, all the glasswares including the container were cleaned very carefully because even a small dust particle could ruin the device. Especially, the top SNAP NWs process requires very clean and flat surfaces in a several millimeters range. In some cases, some dust particles appeared during the vacuum transfer despite the careful preparation. For that case, the SOG was stripped by methanol and then the substrates were cleaned intensively by spraying methanol

onto the substrates followed by blowing the dust particles off with nitrogen gas repeatedly. Upon confirming that the surface is completely dust-free, SOG was spin-coated again at an atmospheric condition. For this second SOG spin-coating, the vacuum condition was not necessary: As mentioned above, the trenches between Si NWs are not usually completely filled with the SOG if the substrate is spin-coated directly at atmospheric pressure. However, the second spin-coating performed at atmospheric pressure fills the trenches completely with the SOG, as indicated by figure 3-6c.

Next, SOG layer thinned down globally using a  $\text{CF}_4$  plasma (20 standard cubic centimeters per minute (sccm), 10 milliTorr, 40 Watts). This etching was monitored periodically by ellipsometer and continued until the SOG layer became about 50 nm thick according to the ellipsometer. This final thickness is very critical because it affects the ensuing top SNAP and Ti layer dry-etching steps significantly. The detailed reasons are described in the paragraphs dedicated to those steps.

After globally thinning the SOG layer, an opening in photo resist was lithographically defined over the Si NWs and the tips of the 18 EBL defined contacts. The SOG was then further etched until the tops of the underlying Si NWs were exposed (Fig. 3-5b, 3-6c, d). This step was monitored by periodically measuring the Si NW conductivity using the test electrodes. The majority of the dopant atoms in the

Si NWs lie within the top 10 nm of the NWs (10, 32). This feature means it is very straightforward to etch back the SOG without thinning the Si NWs, since the conductivity of the NWs is very sensitive to their thickness. At this stage the entire memory circuit is under SOG (and thus electrically isolated from any further top processing) except for the lithographically defined opening over the Si NWs and the 18 contacts. This opening defines the active memory region.

***Deposition of Molecules and Top Electrode Materials*** A monolayer of bistable [2]rotaxane switches (21) was prepared by Langmuir-Blodgett techniques and transferred onto the device as reported previously (8, 33). For the [2]rotaxane used herein, the Langmuir-monolayers were prepared on an aqueous (18 M $\Omega$  H<sub>2</sub>O) subphase of Langmuir-Blodgett (LB) trough (Type 611D, Nima Technology, Coventry, UK). Before the trough was filled with the subphase, all the parts in the trough including compression barriers were cleaned very carefully by wiping with chloroform soaked wipes. Once the parts in the trough were wiped thoroughly, the filtered water was poured until the water level reached the compression barrier. From this point, the quality of the subphase was monitored by a Brewster angle microscope (BAM). For further cleaning, the subphase was compressed to an area of about 50 cm<sup>2</sup> and then the surface of the subphase was sucked by a glass pipette connected to a pump to remove dust particles floating on the subphase surface. As the compression

and cleaning processes were repeated, the number of dust particles decreased and eventually, no dust particle was observed in the BAM image. Then, the barrier was moved back to the open position ( $\sim 245 \text{ cm}^2$ ) and the prepared [2]rotaxane solution was dropped onto the subphase via a syringe. The [2]rotaxanes were prepared in a chloroform solution right before the transfer. After about 30 minutes of the chloroform evaporation, the barrier compression began at a rate of  $5 \text{ cm}^2/\text{min}$ . Once the surface pressure reached the target pressure ( $\pi = 30 \text{ mN/m}$ ), the surface pressure was fixed and the substrate started to be pulled out at a rate of  $1 \text{ mm/min}$ . When the entire substrate was pulled out of the subphase, the step for the preparation of the Langmuir-monolayer was complete.

20 nm of Ti was then evaporated over the entire device (figure 3-5c). This Ti layer serves to protect the molecules from further top processing. Using photolithographic techniques and  $\text{BCl}_3$  plasma etching (10 sccm, 5 mTorr, 30 Watts), the molecule/Ti layer was then everywhere removed except for the memory active region where electrical contact to the underlying Si NWs is made (figure 3-5d). Next, a thin  $\text{SiO}_2$  layer ( $\sim 15 \text{ nm}$ ) was deposited over the entire substrate to isolate the EBL defined electrodes from the Pt NWs deposited in the next step (figure 3-5e). Remember that the SOG layer was about 50 nm thick after the SOG global etching

step as described in the previous paragraph so that the EBL defined electrodes as thick as 65 nm were exposed until the SiO<sub>2</sub> layer deposition.

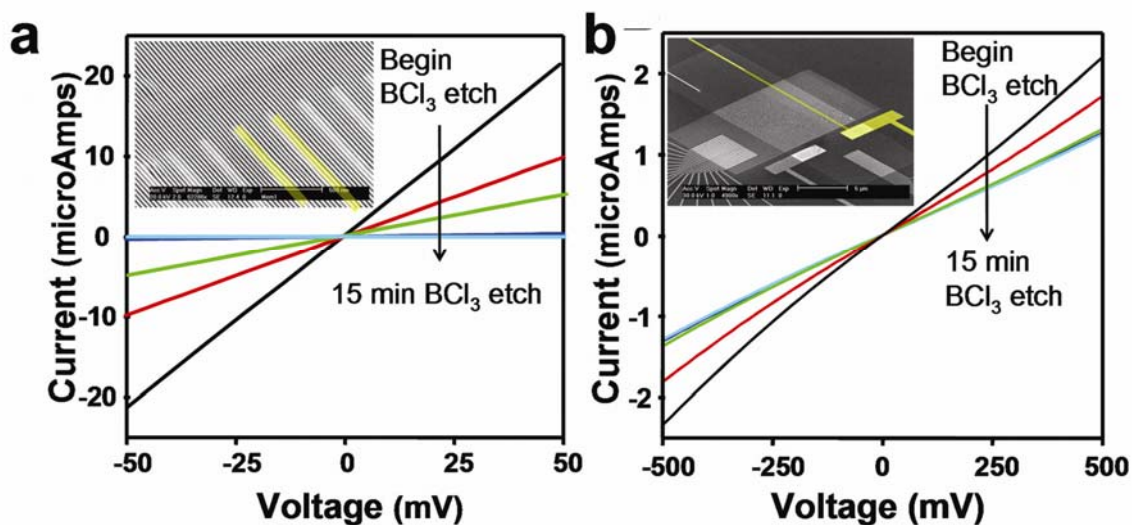


**Figure 3-7.** Conductance monitoring during the Ti layer etching. (a) Cross-conductance measurements between electrical contacts to the top nanowire array were performed to monitor the Ti layer etching. When the current drops to sub-10 nanoAmps, the top Ti electrodes are separated. The inset SEM image shows two representative contacts to the top Ti electrodes as highlighted in yellow. It is the cross-conductance between such contacts that was used for this measurement. (b) The conductivities of SiNWs were measured throughout the Ti layer etching to ensure that SiNWs were not damaged. The SEM image (inset) shows the current pathway that was measured.

Using the SNAP technique, an array of 400 Pt NWs was then deposited over the Ti/SiO<sub>2</sub> layer and perpendicular to the underlying Si NWs (figure 3-5f). For the

deposition of the Pt NWs, a different epoxy mixture (5 ml of THF, 5 drops of dibutylphthalate, 10 drops of epoxy and 1 drop of curing agent), compared to the one used for the Si NW generation, was used. A larger portion of epoxy in the new mixture enabled to hold the SNAP masters more firmly while the epoxy mixture was being cured on a hot plate and the GaAs masters were being wet-etched. Especially, the usage of the new epoxy mixture was essential for the deposition of the top SNAP nanowire array because the surface of the substrate became relatively rough throughout many previous steps. For the similar reason, the new mixture was less vulnerable to undercut in the following  $\text{BCl}_3$  plasma etching step. The prevention of the undercut was most challenging task in the project because it could arise from many factors correlating one another (recess depth, strength of cured epoxy, directionality of plasma etching etc.). Finally, careful  $\text{BCl}_3$  plasma etching (10 sccm, 5 mTorr, 30 W) was used to transfer the Pt NW pattern to the underlying  $\text{SiO}_2/\text{Ti}$  film, thus forming Ti NW top electrodes (figure 3-6 g). The global SOG etching down to  $\sim 50$  nm thickness was also critical for this top SNAP nanowire pattern transfer. In the devices that maintained a thick SOG layer, thus a deep recess over the active memory region, the epoxy was trapped in the recess to form its thick layer. The thick layer of epoxy was susceptible to undercut during the  $\text{BCl}_3$  plasma etching and thus to have shorting problems in the top SNAP nanowires. This shorting problem is very fatal in a

device performance because the yield of independent bits will decrease significantly. The etch endpoint was determined by monitoring the cross-conductance of the top Ti NWs (figure 3-7 a). Complete transfer of the Pt NW pattern to the underlying Ti film was indicated by a fall in the cross-conductance to about 10 nS. Note that the cross-conductance does not go to zero since the Ti electrodes, while physically separated, are still electrically coupled through the crossbar junctions and the underlying Si NWs. The health of the underlying Si NWs throughout the Ti-etching steps was also monitored as shown in figure 3-7b. In most cases, the devices that skipped the SOG planarization step lost the Si NW conductance completely before the cross-conductance fell down to a value corresponding to the complete NW pattern transfer, indicating that Si NWs were damaged significantly during the  $\text{BCl}_3$  plasma etching. Once  $\text{BCl}_3$  plasma etching is done, the device is ready for testing. SEM images for final devices are presented in figure 3-8 at different resolution.

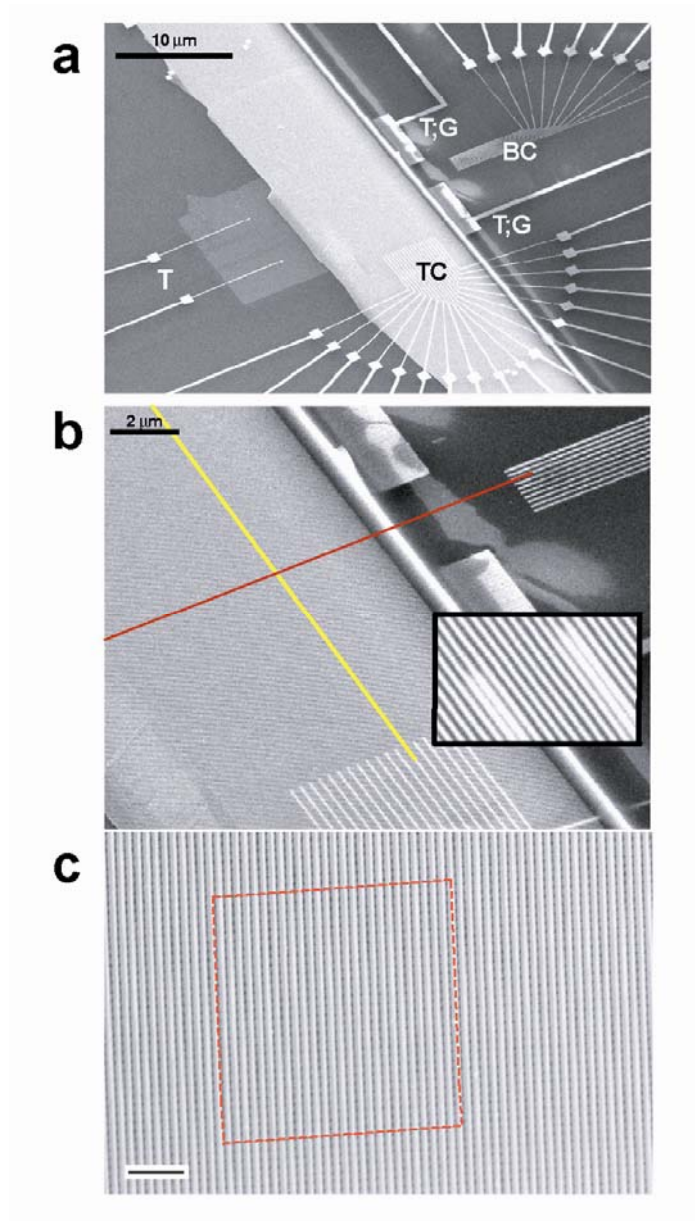


**Figure 3-8.** Scanning electron micrographs (SEMs) of the NW crossbar memory. (a) Image of the entire circuit. The array of 400 bottom Si NWs is seen as the light grey rectangular patch extending diagonally up from bottom left. The top array of 400 Ti NWs is covered by the SNAP template of 400 Pt NWs, and extends diagonally down from top left. Testing contacts (T) are for monitoring the electrical properties of the Si NWs during the fabrication steps. Two of those contacts are also grounding contacts (G), and are used for grounding most of the Si NWs during the memory evaluation,

writing, and reading steps. Electron beam lithography patterned 18 top (TC) and 10 bottom (BC) contacts are also visible. The scale bar is 10 micrometers. (b) An SEM image showing the cross-point of top and bottom NW electrodes. Each cross point corresponds to an ebit in memory testing. (inset) The electron-beam-lithography defined contacts bridged 2-4 nanowires each. The scale bar is 2 micrometers. (c) High resolution SEM of approximately 2500 junctions out of a 160,000 junction nanowire crossbar circuit. The red square highlights an area of the memory that is equivalent to the number of bits that were tested. The scale bar is 200 nanometers.

### **3.5 160 kbit Molecular Electronic Memory Circuits: Device Testing**

The memory circuit was tested using a custom-built probe card and a Keithley 707A switching matrix for off-chip demultiplexing. Because SNAP NWs are patterned beyond the resolution of lithographic methods (34), each test electrode contacted between 2 and 4 NWs so that individual effective bit (ebit) contains between 4 and 16 crossbar junctions, but mostly 9 crossbar junctions. All ebits were electrically addressed within the 2D crosspoint array by the intersection of one Si NW bottom electrode and one Ti NW top electrode. Individual molecular junctions were set to their low resistance or “1” state through the application of a positive 1.5 – 2.3 V pulse (voltages are referenced to the bottom Si NW electrode) of 0.2 s duration. A junction was set to its “0” or high resistance state through application of a -1.5 V pulse, also of 0.2 s duration. To avoid switching an entire column or row of bits, the

switching voltage was split between the two electrodes defining the ebit. Thus, to write a “1” with +2 V, a single Si NW electrode is charged to +1 V, while a single Ti NW electrode is set to -1V, and only where they cross does the junction feel the full +2 V switching voltage. Half-selected bits, that is, bits receiving only half the switching voltage, were never observed to switch. This half-select issue, though being a clear drawback of crossbar architecture, is overcome by distinctive characteristic of [2]rotaxane: As introduced in the subchapter 3-1, the voltages required to switch on/off MSTJs were uniform over broad junctions such that a half of the voltage did not perturb the junctions. Individual ebits were read by applying a small, non-perturbing +0.2 V bias to the bottom Si NW electrode and grounding the top Ti NW electrode through a Stanford Research Systems SR-570 current pre-amplifier. Bits not being read were held at ground to reduce parasitic current through the crossbar array. Note that all the electrical writing and reading operations described herein were done sequentially. Schematic illustrations describing the device testing procedures composed of writing and reading bits are presented in figure 3-9. A LabWindow code used for the entire measurement procedures is also attached in Appendix B.

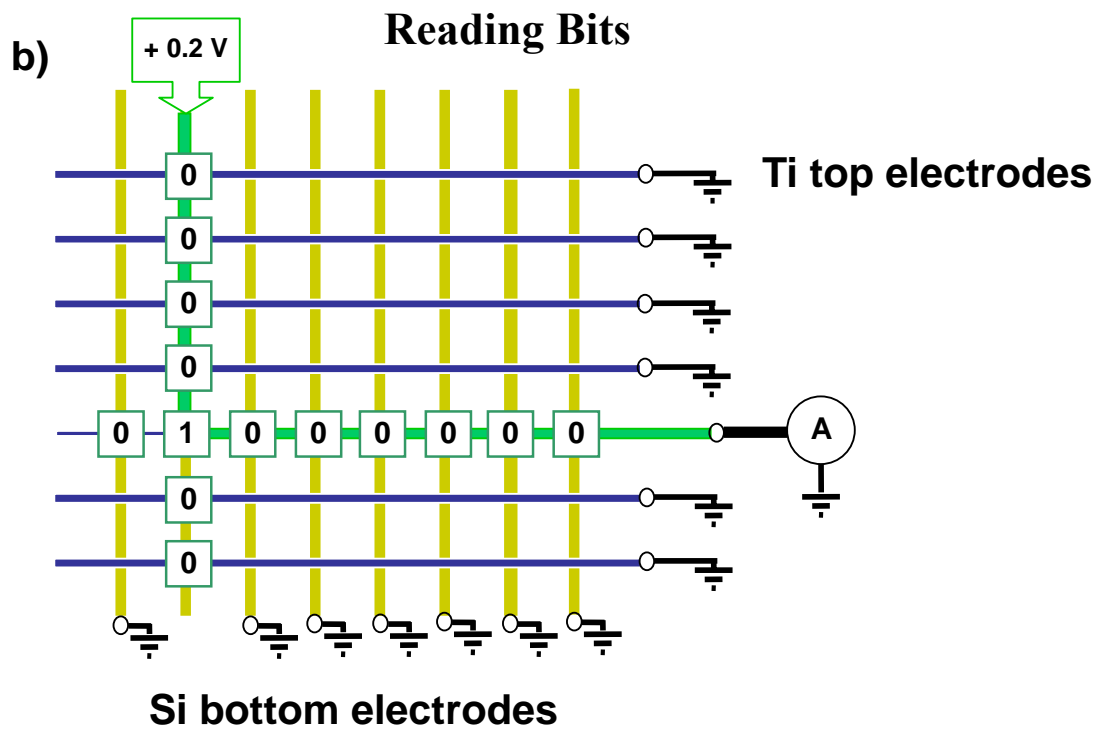
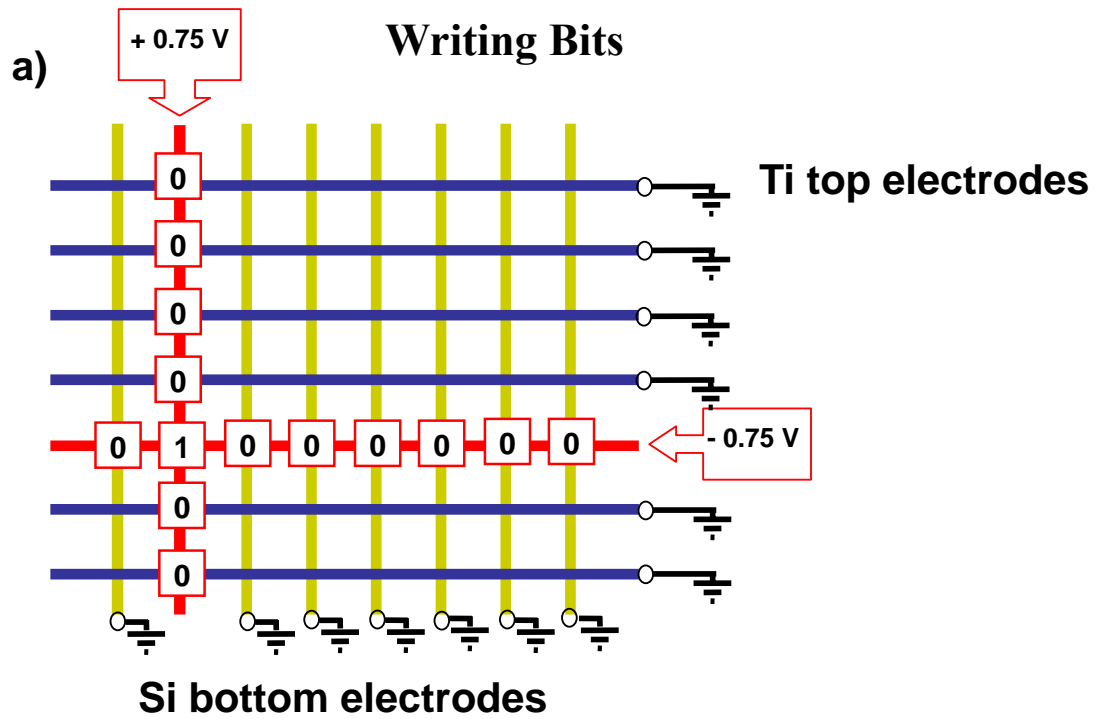


**Figure 3-9.** Writing and reading procedures in crossbar memory measurements. (a)

Due to the half select issue, the writing bias was split into two halves of opposite

polarity and each half was applied to both top and bottom electrodes, respectively, defining a designated cross-point. Other bits along these top and bottom electrodes are not perturbed due to the sharp switch-on/off bias characteristic of [2]rotaxanes. (b) Before and after applying the writing voltages, the resistances of all bits are read at small non-perturbing reading bias to monitor the resistance change. Note that all other electrodes not involved in the switching of the designated cross junction stay grounded to minimize the parasitic current pathways.

By scanning electron microscopy inspection, the crossbar appeared to be structurally defect-free, with no evidence of broken, wandering, or electrically shorted NWs. Nevertheless, electrical testing identified a large number of defective bits and the nature of those defects. This testing was done by first applying a +1.5 V pulse relative to the Si NW bottom electrodes to set all bits to '1', and then reading each ebit sequentially using a non-perturbing +0.2 V bias. A -1.5 V pulse was then applied to set all bits to '0'. The status of each of the ebits was again read. The raw data throughout these procedures and the 1/0 current ratios are presented in figure 3-10.

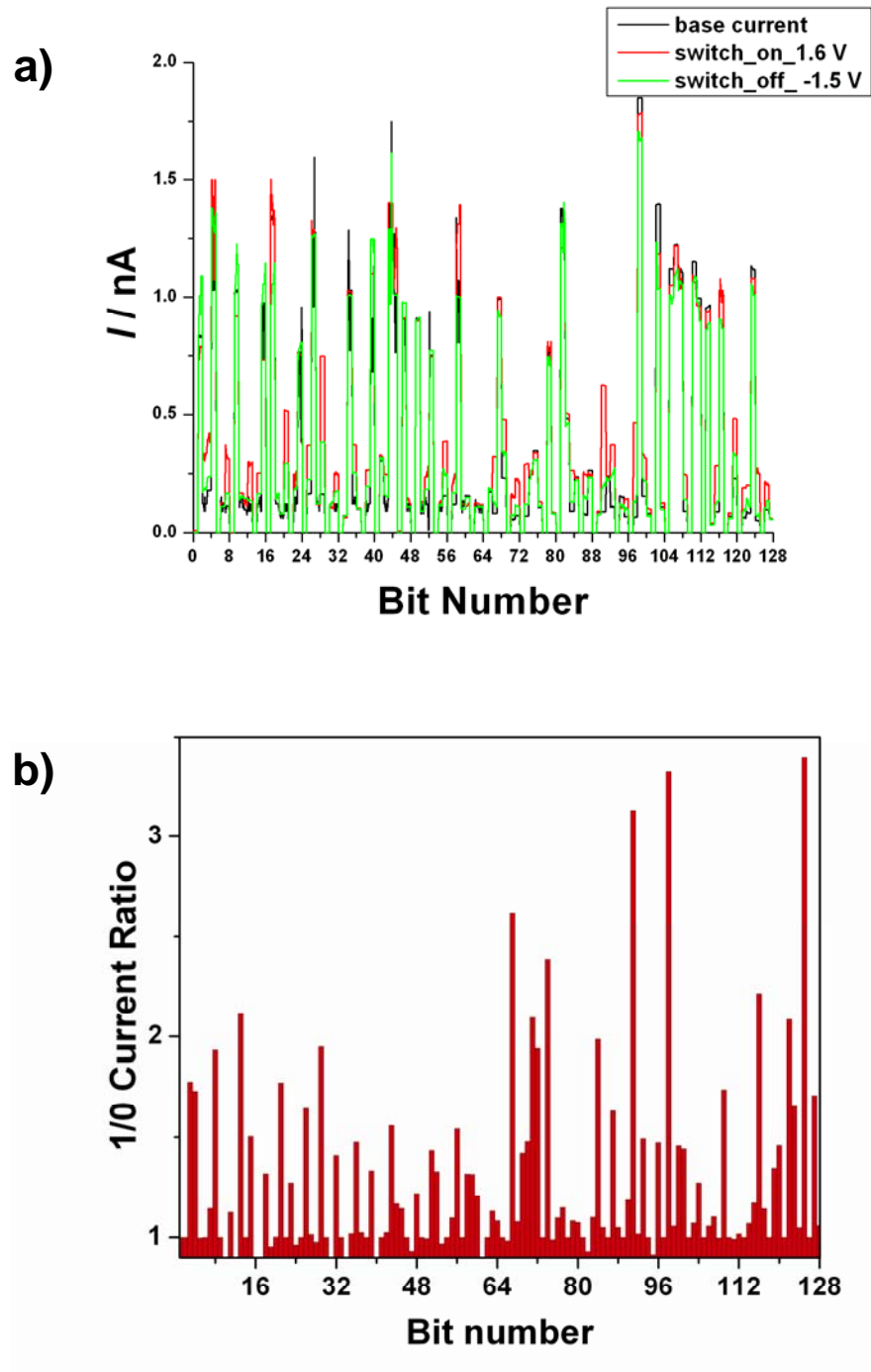


**Figure 3-10.** Data from evaluating the performance of the 128 ebits within the crossbar memory circuit. (a) raw current data when monitored at +0.2 V at the stage of before-switch on, after-switch-on and after-switch-off. (b) The current ratio of the

'1' state divided by the '0' state of the tested ebits. Note that many of the ebits exhibit little to no switching response. Those ebits are defective.

About 50% of the bits yielded some sort of switching response. Some of that response, however, may have originated from parasitic current pathways through the crossbar array. This is an inherent drawback of crossbar architectures wherein each junction is electrically connected to every other junction. The standard remedy is to incorporate diodes at each crosspoint (35), and although the molecule/Ti interface yields some rectification (36), we additionally grounded all NW electrodes not being used during a read or write step. By the way, the amount of rectification is dependent upon the amount of titanium oxidation that occurs at the molecule/Ti interface which, in turn, depends upon the vacuum level of the metal deposition system. For the devices reported here, the Ti was deposited at a pressure of approximately  $5e-7$  Torr. For isolated devices, but constructed in a fashion similar to what was done here, this typically produces a rectification of about 10:1 at 1 V. We established a threshold for a 'good' bit based upon a minimum 1/0 current ratio of  $\sim 1.5$ . About 25% of the ebits passed this threshold.

Electrical testing revealed several types of defects (figure 3-11). Bad ebits fell into a few classes, with the two most common groups being ebits that were either poor

switches with little or no switching response or open circuits. Adjacent, shorted Ti top electrodes were identified when the ebits addressed by those electrodes were not independently addressable. Even though that type of defect is not completely fatal (i.e. two rows of fabricated ebits could still be utilized as a single row), we did not use ebits associated with shorted top electrode defects. The defects classified as ‘switch defects’ likely arose from sub-nanometer variations in the reactive ion etching process that was employed to define the top Ti crossbar NWs. Isolated devices, or crossbar memories patterned at substantially lower densities and with larger wires, can typically be prepared with a nearly 100% yield. The switch defects led to only a proportional loss in the yield of functional bits, while bad contacts or shorted nanowires removed an entire row of bits from operation. An important result from the defect map (figure 3-11) is that the good and bad bits are randomly dispersed, implying that the crossbar junctions are operationally independent of one another.

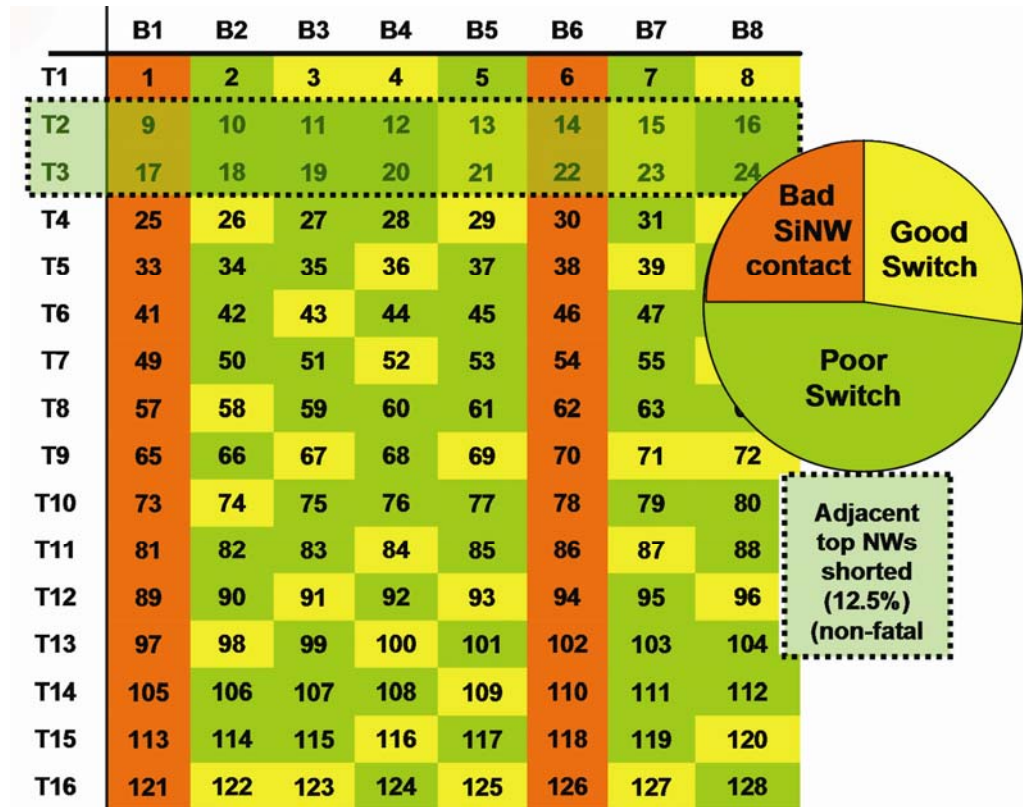


**Figure 3-11.** A map of the defective and useable ebits, along with a pie-chart giving the testing statistics. Note that, except for the bad Si NW contacts on bottom electrodes B1 and B6, and the shorted top electrodes T2 and T3, the defective and good bits are randomly distributed. Type I defects (26% of the 128 tested) are ebits that exhibited an open-circuit conductance and a low or zero amplitude switching response when tested. Type II defects (22%) are non-switchable bits that exhibited a conductance similar to that of a closed bit.

However, the ultimate test of any memory is whether it can be used to store and retrieve information. Based upon the defect map, we identified the addresses of the usable ebits, and from those addresses configured an operational memory (figure 3-12): the usable bits were used to store and read out small strings of information

written in standard ASCII code. The maximum number of ebits that could be tested was 180, but our electronics were configured to test 128 ebits (< 1% of the actual crossbar), and that was sufficient to demonstrate the key concepts of this memory.

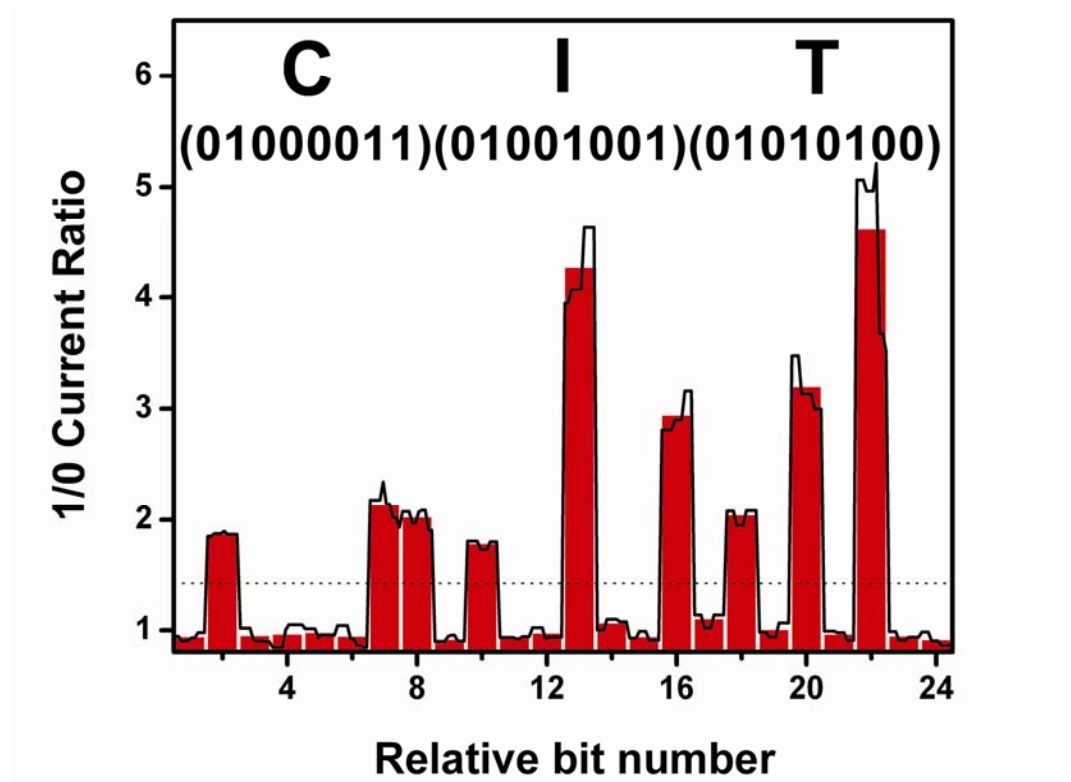


**Figure 3-12.** A demonstration of point-addressability within the crossbar. Good ebits were selected from the defect mapping of the tested portion of the crossbar. A string of '0's and '1's corresponding to ASCII characters for 'CIT' (abbreviation for California Institute of Technology) were stored and read out sequentially. The dotted line indicates the separation between a '0' and '1' state of the individual ebits. The black trace is raw data showing ten sequential readings of each bit while the red bars represent the average of those ten readings. Note that deviations of individual readings from their average are well separated from the threshold 1/0 line.

The solid-state switching signature of the bistable [2]rotaxanes that were used here has been shown to originate from electrochemically addressable, molecular mechanical switching for certain device structures (8, 30), but not for metal wire / molecule/metal wire junctions (37). In fact, our desire to utilize molecular mechanical bistable switches as the storage elements is what dictated our choice of the silicon NW / molecule / Ti NW crossbar structure. This switching signature should be effectively size-invariant, meaning that it should scale to the macromolecular dimensions of these crossbar junctions. Solid-state-based switching materials (1, 2) will likely not exhibit similar scaling since they arise from inherently bulk properties. The thermodynamic and kinetic parameters describing both the bistability and switching mechanism of the [2]rotaxane switch (and similar molecular mechanical switches (38)) have been quantified in a variety of environments(30), as described in chapter 2. Those measurements required robust switching devices that could be cycled many times and at various temperatures. The memory bits measured here were much more delicate – while all good ebits could be cycled multiple times (as evidenced by the testing and writing steps), most ebits failed after a half-dozen or so cycles, and none lasted longer than ten cycles. However, we measured the rate of relaxation from the 1→0 state for many of the ebits (figure 3-13). From a device perspective, this represents the volatility, or memory retention time, of the bits. With respect to the

bistable [2]rotaxane switching cycle, this represents a measurement of the rate limiting kinetic step within the switching cycle (30). Our measured rate ( $90 \pm 40$  minutes; median decay = 75 minutes) was statistically equivalent to that reported for much larger (and more fully characterized) devices ( $58 \pm 5$  minutes) (30). Thus, our results are consistent with a molecular mechanism for the switching operation (8, 30). The volatility measurements were carried out by switching selected bits to the “1” or low resistance state, and then reading the current through those bits as a function of time.

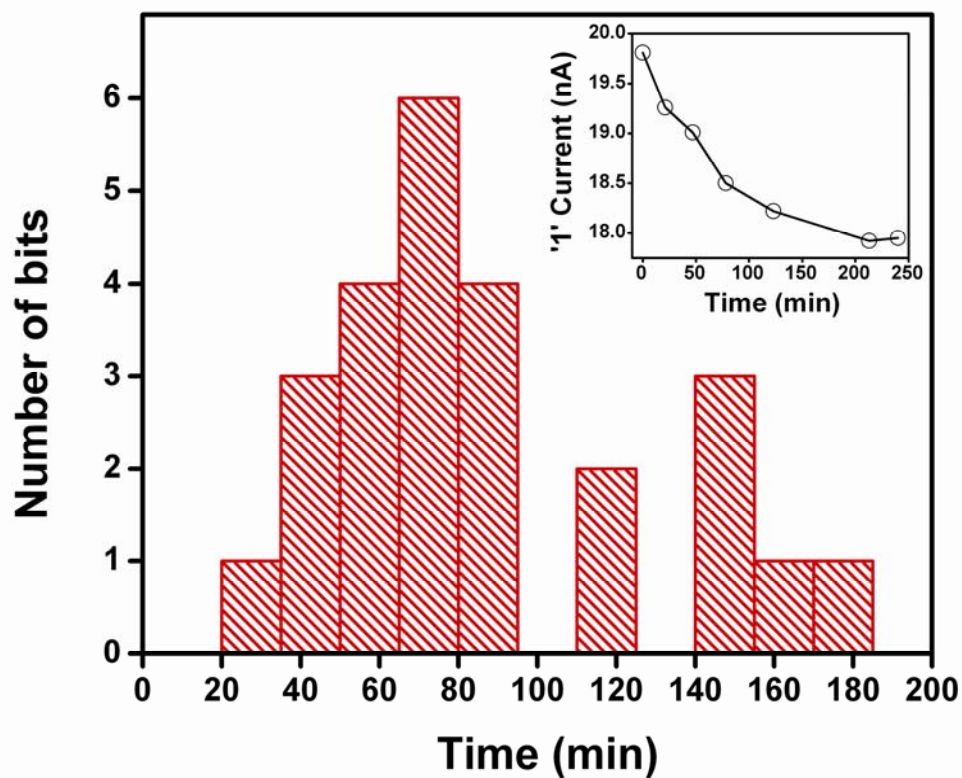


**Figure 3-13.** A histogram representing the  $1/e$  decay time of the ‘1’ state to the ‘0’ state. The 25 ebits represented in the data were each ‘large’ ebits, comprised of approximately 100 junctions, to increase the measurement signal to noise. Raw data from a single large ebit is shown in the inset.

### **3.6 Limitations of the SNAP Process for Crossbar Memory Formation**

The nanofabrication methods described in this chapter for creating the 160 kilobit crossbar memory circuit can be significantly extended in terms of both memory size and bit density. For our memories, the crossbar electrode materials choices have proven to be very important for successful memory operation. In other words, Si bottom electrodes and metallic top electrodes with a Ti adhesion layer were keys. Metal NWs at 8 nm half-pitch have been reported previously (11). Such NWs, formed by the SNAP process, only serve as templates for forming the crossbar electrodes. To be used in a crossbar memory, the SNAP NW pattern must be transferred to Si or Ti NWs for the bottom and top electrodes, respectively. Thus, it is not just the SNAP process, but the ability to translate the initially deposited SNAP NWs to form other NWs that ultimately limits the size and density of the circuitry that can be fabricated. In figure 3-3a, I present an array of 7 nm wide, 15 nm tall single crystal Si NWs patterned at 6.5 nm half-pitch. This corresponds to a crossbar that

would contain approximately  $6 \times 10^{11}$  bits  $\text{cm}^{-2}$ . While this array may not represent the density limit of what could be achieved, densities in excess of  $10^{12}$   $\text{cm}^{-2}$  will be very hard to obtain using these patterning methods.

Similarly, the 160,000 junction crossbar also doesn't represent any sort of limitation. In figure 3-3b, we present SEM images of 1400 Si NWs formed using the SNAP method. Such an array size permits the formation of a 2 million bit crossbar, and it is certainly possible to further expand the concept to substantially larger structures. As mentioned in the subchapter 3-2, the primary limitation is that the SNAP process is that, while it is a parallel patterning method – since all nanowires within an array are created simultaneously, each array must be fabricated one at a time using a labor intensive process. A single worker, for example, can fabricate only about 20 arrays of Si NWs in a single day. However, recent advances in using nanoimprinting (39) to replicate SNAP nanowires and to form crossbar structures indicate that high-throughput, parallel fabrication methods can be developed, even at the near molecular-densities described in this chapter.

### **3.7 Conclusion**

This chapter focuses on molecular electronic memory circuits. The various generations of memory devices described in this chapter hold such common features

that the devices are based on the crossbar circuit and utilize [2]rotaxanes as information storage components. Through many generations, however, total number of bits within a single crossbar circuit and a bit density increased significantly. This scaling was possible due to the development of the fabrication procedures that allowed the integration of more delicate and higher density of electrodes with the [2]rotaxane molecular monolayer. Despite more complicated fabrication procedures, the devices containing higher bit densities still showed the molecular switching signature. Especially, the final generation devices fabricated based upon the ultra-dense SNAP nanowire arrays also retained the molecular switching signature and exhibited a point addressability within a crossbar circuitry. Although about 75 % of the tested bits in the SNAP nanowire-based device turned out to be defective, the functional part was identified through an electrical testing and configured to write and read specific information. Notably, due to the extremely small pitch ( $\sim 33$  nm) of the SNAP nanowire array, the resultant 160 kbit crossbar memory circuits set a remarkable record in a bit density ( $10^{11}$  bits/cm<sup>2</sup>).

Many scientific and engineering challenges, including device robustness, improved etching tools, and improved switching speed, remain to be addressed before this ultra-dense crossbar memory described here can be practical. Nevertheless, this 160,000 bit molecular memory does provide evidence that at least some of the most

challenging scientific issues associated with integrating nanowires, molecular materials, and defect tolerant circuit architectures at extreme dimensions are solvable.

While it is unlikely that these digital circuits will scale to a density that is only limited by the size of the molecular switches, it should be possible to significantly increase the bit density over what is described here. Recent nanoimprinting results suggest that high-throughput manufacturing of these types of circuits may be possible (39). Finally, these results provide a compelling demonstration of many of the nanotechnology concepts that were introduced by the Teramac supercomputer several years ago, albeit using a circuit that contained a significantly higher fraction of defective components relative to the Teramac machine (12).

### 3.8 References

1. Waser, R. & Rudiger, A. (2004) *Nat. Mater.* 3, 81-82.
2. Allwood, D. A., Xiong, G., Faulkner, C. C., Atkinson, D., Petit, D. & Cowburn, R. P. (2005) *Science* 309, 1688-1692.
3. Flood, A. H., Peters, A. J., Vignon, S. A., Steurman, D. W., Tseng, H. R., Kang, S., Heath, J. R. & Stoddart, J. F. (2004) *Chem. Eur. J.* 10, 6558-6564.
4. Steurman, D. W., Tseng, H. R., Peters, A. J., Flood, A. H., Jeppesen, J. O., Nielsen, K. A., Stoddart, J. F. & Heath, J. R. (2004) *Angew. Chem. Int. Ed.* 43,

- 6486-91.
5. Tseng, H. R., Wu, D., Fang, N. X., Zhang, X. & Stoddart, J. F. (2005) *Chemphyschem* 5, 111-6.
  6. Deng, W. Q., Muller, R. P. & Goddard, W. A. (2004) *J. Am. Chem. Soc.* 126, 13562-13563.
  7. Kim, Y. H., Jang, S. S., Jang, Y. H. & Goddard, W. A. (2005) *Phys. Rev. Lett.* 94.
  8. Luo, Y., Collier, C. P., Jeppesen, J. O., Nielsen, K. A., Delonno, E., Ho, G., Perkins, J., Tseng, H. R., Yamamoto, T., Stoddart, J. F. & Heath, J. R. (2002) *Chemphyschem* 3, 519-525.
  9. Beckman, R., Johnston-Halperin, E., Luo, Y., Green, J. E. & Heath, J. R. (2005) *Science* 310, 465-468.
  10. Beckman, R. A., Johnston-Halperin, E., Melosh, N. A., Luo, Y., Green, J. E. & Heath, J. R. (2004) *J. Appl. Phys.* 96, 5921-5923.
  11. Melosh, N. A., Boukai, A., Diana, F., Gerardot, B., Badolato, A., Petroff, P. M. & Heath, J. R. (2003) *Science* 300, 112-115.
  12. Heath, J. R., Kuekes, P. J., Snider, G. S. & Williams, R. S. (1998) *Science* 280, 1716-1721.
  13. DeHon, A., Goldstein, S. C., Kuekes, P. J. & Lincoln, P. (2005) *IEEE Trans.*

*Nanotechnol.* 4, 215-228.

14. DeHon, A. & Naeimi, H. (2005) *IEEE Des. Test Comput.* 22, 306-315.
15. Lee, M. H., Kim, Y. K. & Choi, Y. H. (2004) *IEEE Trans. Nanotechnol.* 3, 152-157.
16. Snider, G., Kuekes, P., Hogg, T. & Williams, R. S. (2005) *Appl. Phys. A* 80, 1183-1195.
17. Stan, M. R., Franzon, P. D., Goldstein, S. C., Lach, J. C. & Ziegler, M. M. (2003) *Proc. IEEE* 91, 1940-1957.
18. Diehl, M., Beckman, R., Yaliraki, S., and Heath, J. R. (2002) *Angew. Chem. Int. Ed.* 41, 353-356.
19. Wu, W., Jung, G. Y., Olynick, D. L., Straznicky, J., Li, Z., Li, X., Ohlberg, D. A. A., Chen, Y., Wang, S. Y., Liddle, J. A., Tong, W. M. & Williams, R. S. (2005) *Appl. Phys. A-Mater. Sci. Process.* 80, 1173-1178.
20. Zhong, Z. H., Wang, D. L., Cui, Y., Bockrath, M. W. & Lieber, C. M. (2003) *Science* 302, 1377-1379.
21. Tseng, H. R., Vignon, S. A., Celestre, P. C., Perkins, J., Jeppesen, J. O., Di Fabio, A., Ballardini, R., Gandolfi, M. T., Venturi, M., Balzani, V. & Stoddart, J. F. (2004) *Chem. Eur. J.* 10, 155-172.
22. Duan, X. F. & Lieber, C. M. (2000) *Adv. Mat.* 12, 298-302.

23. Fan, R., Yue, M., Karnik, R., Majumdar, A. & Yang, P. D. (2005) *Phys. Rev. Lett.* 95.
24. Yang, P. & Kim, F. (2002) *Chemphyschem* 3, 503-6.
25. Heath, J. R. & Ratner, M. A. (2003) *Physics Today* 56, 43-49.
26. Pop, E., Mann, D., Cao, J., Wang, Q., Goodson, K. & Dai, H. (2005) *Phys. Rev. Lett.* 95, 155505.
27. Xiang, J., Lu, W., Hu, Y., Wu, Y., Yan, H. & Lieber, C. M. (2006) *Nature* 441, 489-93.
28. Zhou, X., Park, J. Y., Huang, S., Liu, J. & McEuen, P. L. (2005) *Phys. Rev. Lett.* 95, 146805.
29. Chen, Z., Appenzeller, J., Lin, Y. M., Sippel-Oakley, J., Rinzler, A. G., Tang, J., Wind, S. J., Solomon, P. M. & Avouris, P. (2006) *Science* 311, 1735.
30. Choi, J. W., Flood, A. H., Steuerman, D. W., Nygaard, S., Braunschweig, A. B., Moonen, N. N. P., Laursen, B. W., Luo, Y., DeIonno, E., Peters, A. J., Jeppesen, J. O., Xu, K., Stoddart, J. F. & Heath, J. R. (2006) *Chem. Eur. J.* 12, 261-279.
31. Huang, Y., Duan, X. F., Wei, Q. Q. & Lieber, C. M. (2001) *Science* 291, 630-633.
32. Wang, D., Sheriff, B. A. & Heath, J. R. (2006) *Nano Lett.* 6, 1096-100.
33. DeIonno, E., Tseng, H. R., Harvey, D. D., Stoddart, J. F. & Heath, J. R. (2006)

- J. Phys. Chem. B* 110, 7609-12.
34. View, C., Carcenac, F., Pepin, A., Chen, Y., Mejias, M., Lebib, A., Manin-Ferlazzo, L., Couraud, L., Launois, H. (2000) *Appl. Surf. Sci.* 164, 111-117
  35. Parkin, S. S. P., Roche, K. P., Samant, M. G., Rice, P. M., Beyers, R. B., Scheuerlein, R. E., O'Sullivan, E. J., Brown, S. L., Bucchigano, J., Abraham, D. W., Lu, Y., Rooks, M., Trouilloud, P. L., Wanner, R. A. & Gallagher, W. J. (1999) *J. Appl. Phys.* 85, 5828-5833.
  36. McCreery, R. L. (2004) *Chem. Mater.* 16, 4477-4496
  37. Chen, Y., Jung, G. Y., Ohlberg, D. A. A., Li, X. M., Stewart, D. R., Jeppesen, J. O., Nielsen, K. A., Stoddart, J. F., Williams, R. S. (2003) *Nanotechnology* 14, 462-468
  38. Katz, E., Baron, R., Willner, I., Richke, N. & Levine, R. D. (2005) *Chemphyschem* 6, 2179-2189.
  39. Jung, G. Y., Johnston-Halperin, E., Wu, W., Yu, Z. N., Wang, S. Y., Tong, W. M., Li, Z. Y., Green, J. E., Sheriff, B. A., Boukai, A., Bunimovich, Y., Heath, J. R. & Williams, R. S. (2006) *Nano Lett.* 6, 351-354.

## Chapter 4

### Nanofluidics

#### 4.1 Introduction

Research on nanofluidics has expanded rapidly because it enables one to observe novel scientific phenomena in fluid dynamics occurring in unexplored dimensions, and also covers some features that can be utilized for various applications.

Nanofluidic channels in the form of cell membrane ion channels, such as  $\alpha$ -hemolysin, were first used in the 1990s to detect DNA and RNA (1). By applying a voltage across these channels, DNA and RNA molecules were drawn through as extended linear chains. Their presence detectably reduced normal ionic flow through the nanochannels, and it was possible to characterize the length of the polymers and even small portions of their sequences (2). Recently, fabricated inorganic nanochannels have gained preference over the biological membrane channels due to better control over channel dimensions and surface characteristics (3-6).

Most of these conduits have been made of silica, a material which has allowed nanochannels to exhibit interesting phenomena in the presence of aqueous solutions. In aqueous solutions, water reacts with silica to form silanol groups, as shown in following reaction:



In most cases, water is a little acidic at  $\text{pH} \sim 6$ , whereas the  $\text{pK}_a$  of silica is between 2 and 4.5. Therefore, when exposed to water, the silanol groups become deprotonated, resulting

in the formation of negative charges on the surface of the silica. In the presence of ionic solutions, positively-charged counter-ions accumulate next to the channel surface, effectively shielding the negative surface charge over a distance called the Debye length (7). The dimensions of conventional microfluidic channel devices far exceed this characteristic length, therefore the surface charge has a negligible effect upon the distribution of ions in solutions flowing inside. However, the width and height of nanofluidic channels can be on the order of the Debye length, allowing the surface charge to have a dominating effect on ion distributions within the nanochannels (6, 8).

Advantages of nanofluidic devices are multifold. First, nanofluidic devices enable electrical and optical detection at the same time. The movement of the target molecules attached to a fluorescent dye may be tracked optically. Even without optical monitoring, binding of the target molecule on the surface of the channel or transport of relatively large molecules may be detected electrically. Because surface charge dominates ionic conductance when the Debye length exceeds the channel dimensions (9, 10), reactions or other molecular events that change the channel surface charge can be detected electrically. Also, as the size of target molecules is comparable to the channel dimensions, transport of the target molecules could be electrically detected due to excluded volume effect (3). Second, nanofluidic devices can be used to separate molecules, as an alternative to gel methods, but with better resolution. Obviously, the nanofluidic devices will block molecules larger than the channel dimensions, allowing only smaller molecules to pass through. Furthermore, by utilizing electrostatic interactions between the molecules and the nanofluidic channel surface, the nanofluidic devices can distinguish molecules based on their charges. Han and colleagues developed 2-D nanofluidic arrays to separate DNA

and proteins based upon their lengths and isoelectric points (11). They reported on the anisotropic nanofilter array (ANA), which is a unique filtering platform that incorporates various sieving mechanisms such as Ogston sieving, entropic trapping and electrostatic sieving. Third, one-dimensional geometry with a cross-section that is on the order of macromolecular dimensions provides for a unique environment. Most polymers whose radius of gyration is larger than channel diameter could be stretched out along the channel. This stretching can be a useful tool for studying the importance of molecular structure in various reactions. Austin and his colleagues delivered lambda-DNA and restriction enzymes to the nanochannels, and then observed site-specific positions where nucleotides were digested by these restriction enzymes at single molecule resolution. Finally, confined environments mimic real intracellular conditions where only nanometer-size pores, supported in a matrix of between impermeable molecules, are available for molecular transport. Investigating biological reactions in such cell-like conditions might be helpful for predicting their kinetics and equilibrium in real cell environments.

Taking advantage of the capability of fabricating nanowire arrays, I have initiated a nanofluidic project starting in the summer of 2006. The near-term goal of the project is to detect and separate peptides based on their isoelectric points. Although the project is still in the development stage, many promising results have been produced and I expect that the device will find a host of applications in biomolecule sensing. In this chapter, I will introduce the device fabrication procedures, progresses to date and future directions.

## 4.2 Device Fabrication

The first step in building nanochannels was to generate a nanowire template. The SNAP method (12) and standard electron beam lithography (EBL) were used to make an array of silicon nanowires on a transparent quartz substrates. The detailed procedures of the SNAP method are described in subchapter 3-2. In the silicon nanowire array generated by the SNAP method, each wire was about 15 - 20nm wide and 50 nm apart from adjacent wires. The wires were sectioned into regions about 25  $\mu\text{m}$  in length and 5  $\mu\text{m}$  in width by standard electron beam lithography (EBL). The standard EBL procedures used here were the same as in the fabrication of 160 kbit molecular electronic memory devices (see subchapter 3-4). Low Pressure Chemical Vapor Deposition (LPCVD) was then used to deposit a 5  $\mu\text{m}$  thick silicon dioxide layer on top of and between the wires according to the reaction:  $\text{SiH}_4 + \text{O}_2 \rightarrow \text{SiO}_2 + 2\text{H}_2$ . Photoresist was spun onto the low temperature oxide (LTO) layer and a microchannel pattern was made by photolithography. The pattern was etched down via an Active Oxide Etching (AOE) process ( $\text{CHF}_3:\text{C}_4\text{F}_8:\text{Ar} = 33 \text{ sccm}:7 \text{ sccm}:10 \text{ sccm}$ , 200 W, 10 mTorr, 15 minutes) to expose the ends of the SNAP wires (figure 4-1a). This gave a set of microchannels connecting either end of the SNAP wires. The microchannel depth that was about 5.5  $\mu\text{m}$  was confirmed by a surface profiler (Dektak 150), and then the photoresist was striped by acetone. The substrate was further cleaned by a piranha solution ( $\text{H}_2\text{SO}_4:\text{H}_2\text{O}_2 = 3:1$  by volume). At this point,  $\text{XeF}_2$  was used to selectively and isotropically etch the silicon wires to form hollow channels within the glass according to the reaction:  $2\text{XeF}_2 + \text{Si} \rightarrow \text{SiF}_4(\text{g}) + 2\text{Xe}(\text{g})$ , as shown in figure 4-1b. Before loading substrates into the  $\text{XeF}_2$  etching chamber, the substrates were dipped into a buffered oxide etching (BOE:

$\text{NH}_4\text{F}/\text{HF}= 6:1$  by volume) solution very quickly to remove native oxide layers on the channel entrances. The pressure of  $\text{XeF}_2$  gas was maintained at about 2800 mTorr during the etching procedures. In most cases, the etching progress was confirmed by a color change in optical microscope images.

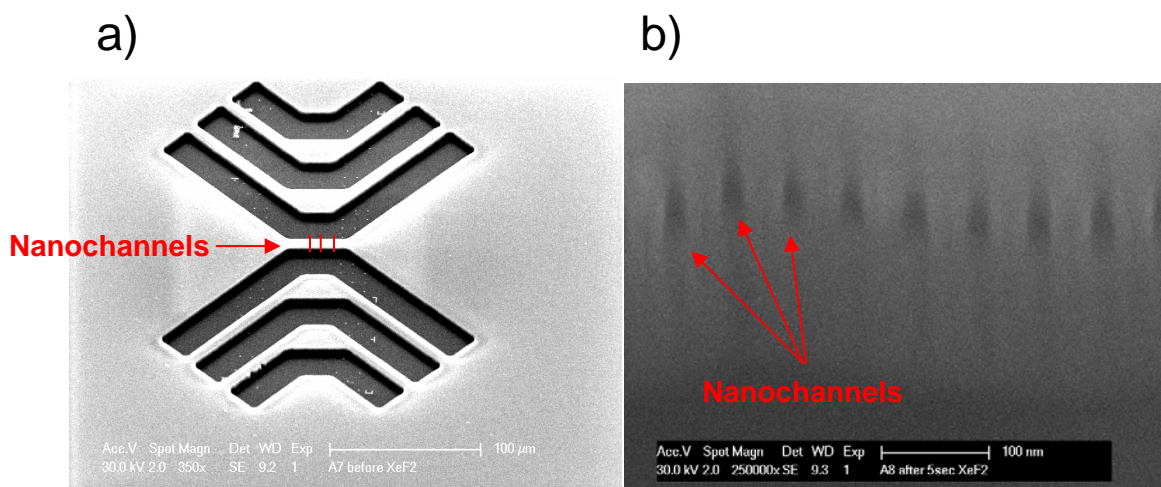


**Figure 4-1.** Scanning electron micrograph (SEM) images of nanofluidic devices. (a) Microchannels are anisotropically etched into the LTO layer, exposing the ends of the SNAP wires. As indicated by the arrow, the nanochannels bridge both sides of the microchannels (b)  $\text{XeF}_2$  etches away the SNAP wires to create nanochannels. The nanochannel entrances are indicated. The channel height appeared to wander due to imaging artifacts.

Finally, PDMS with drilled input/output holes was bonded to the device by using an oxygen plasma technique to create a watertight seal between the microchannels. This seal ensures that the only connection between the microchannels is via the nanochannels. Ionic and biological solutions were inserted through the input holes in the PDMS, and the ionic current measurements were done with the use of a source/preamplifier unit (Keithley 2400) (figure 4-2a). Commercially available Ag/AgCl electrode assemblies (E. W. Wright) were used as electrodes. The ensuing electrophoretic current can be read,

thereby allowing the characterization of ionic and biological transport through the nanochannels.

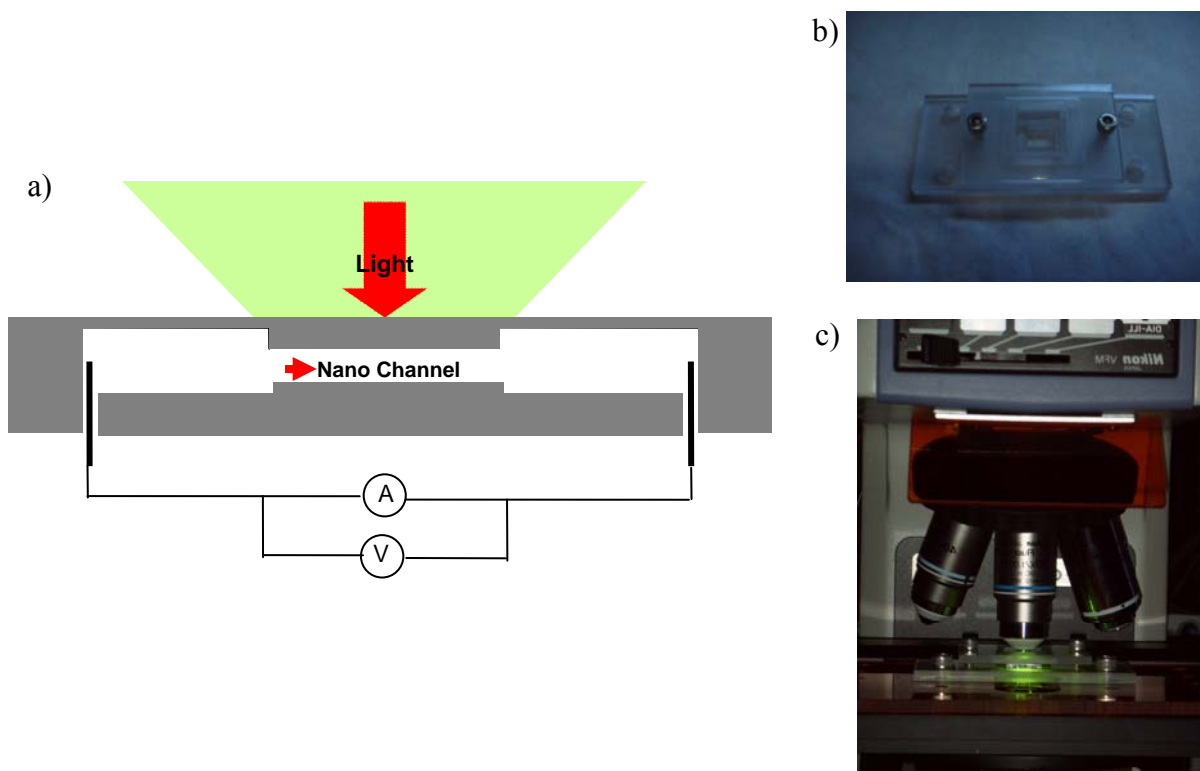


**Figure 4-2.** Nanofluidic device and characterization set-up. (a) Schematic illustration of the nanofluidic device and the measurement set-up. Optical and electrical measurements are carried out simultaneously. (b) A device holder was designed to flip the device over for microscope imaging and to prevent leakage between glass substrate and PDMS cover. (c) Fluorescence microscope used for optical characterization. A nanofluidic device located in the holder is visualized by fluorescence microscopy.

### 4.3 Toward Single-Molecule Chemical Filters

As introduced in the previous subchapters, delicate fabrication techniques allow one to routinely generate the nanochannels whose dimensions are smaller than the Debye screening length. Within this regime, target molecules delivered to the nanochannels are under electrostatic interaction with the nanochannel wall. Therefore, molecules with

different charges might produce different diffusivities, and thus the devices could function as novel type of columns separating molecules based on their charges. Obviously, the idea could be expanded to a variety of molecules such as peptides, polymers and even small molecules.

At low ionic strength, counter-ions are electrostatically attracted by the nanochannel wall, whereas co-ions are repelled because electroneutrality should be satisfied in the nanochannel. Therefore, the nanochannel could be filled with unipolar ions. The unipolar environment makes the nanofluidic system deviate from a bulk solution system where bipolar ionic transport is general at all ionic strengths. In the bipolar regime, the resistance of ionic transport relies on the channel geometry being inversely proportional to the channel cross-section. In case of the unipolar regime, however, the surface charge has an additional effect to attract the counter-ions. Therefore, the ionic transport in the nanochannel should be analyzed separately for co-ions and counter-ions. For clarity, I assign co-ions and counter-ions to negative and positive ions, respectively, because silica is the most common channel material and is negatively charged in contact with aqueous solution.

Now the case where bias is applied through the nanochannel is considered. The negative ions are depleted from the nanochannel region due to the electrostatic repulsion until a bias larger than the nanochannel potential barrier is applied. On the other hand, for the positive ions, a voltage drop along the nanochannel is still valid. But, the density of positive ions in this unipolar regime turns out to increase by order of magnitudes (13, 14). Consequently, the net effect of the nanochannel is a significant increase in ionic flux compared to the bipolar ionic transport where the channel cross-section is the only

parameter contributing to the ion flux. In summary, at low ionic concentration, the channel surface charge dominates the ionic flux in the nanochannel and thereby breaks down the continuity of electric potential for ions of each polarity.

Using fluorescent dyes, the experiment was performed to test the unipolar characteristic of the nanochannel. It was confirmed that with the dyes used herein, fluorescence intensity is linearly proportional to their concentration. Hence, diffusion characteristics for these dyes could be obtained by measuring the fluorescence intensity with respect to time. The fluorescence images were obtained by a fluorescence microscope with a 60x objective (Nikon Fluor) and a 1.0 numerical aperture. The excitation of the fluorophore was performed with a mercury lamp (Nikon super high pressure, C-SHG1) and images were taken with a cooled CCD camera (Hamamatsu, ORCA-ER).

For clear dye tracking, nanochannels about 4  $\mu\text{m}$  wide were defined by EBL. Before the dye loading, potassium chloride (KCl) solution at low ionic strength (10  $\mu\text{M}$ ) was inserted into both sides of the microchannel. Under this background ionic strength in conjunction with concentration of target molecules ( $\sim 10 \mu\text{M}$  in most cases), the Debye screening length is expected to be  $\sim 60 \text{ nm}$ . Therefore the nanochannel thickness ( $\sim 35 \text{ nm}$ ) is smaller than the Debye screening length. The nanochannel wets mainly by the capillary phenomenon and the wetting progress was monitored optically and electrically (figure 4-3). Once the nanochannels are filled with the KCl solution completely, the ionic conductance increases significantly from a noise level to a substantial level, forming linear ohmic IV traces (figure 4-3a). At this point, a drop of dye was located in the inlet of the PDMS and diffusion was monitored thereafter.

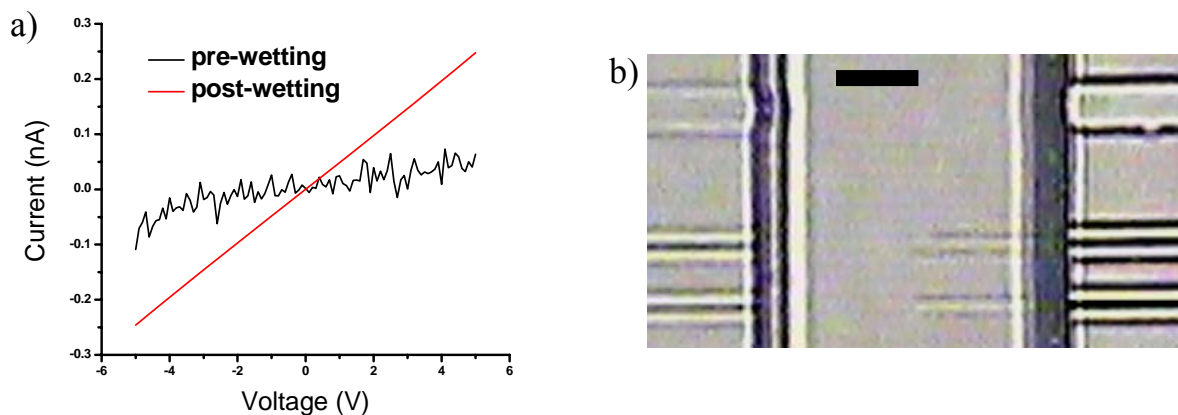


**Figure 4-3.** Nanochannel wetting progress. (a) Conductance across the nanochannel was monitored throughout the wetting process. Once the nanochannels wetted, the current increased significantly. (b) A bright-field image of the nanochannels during the wetting progress. The uppermost wide channel wets completely, whereas two bottom channels wet halfway. Scale bar is 5  $\mu\text{m}$ .

### ***Result and Discussion***

First, cationic and anionic dyes were tested for transport through the nanochannels. Sulforhodamine 101 cadaverine (Anaspec) and fluorescein isothiocyanate (FITC) (Sigma-Aldrich) were used as cationic and anionic dyes, respectively. Fluorescence images of those dyes at different time are presented in figures 4-4 and 4-5, alongside their molecular structures and fluorescence intensity data.

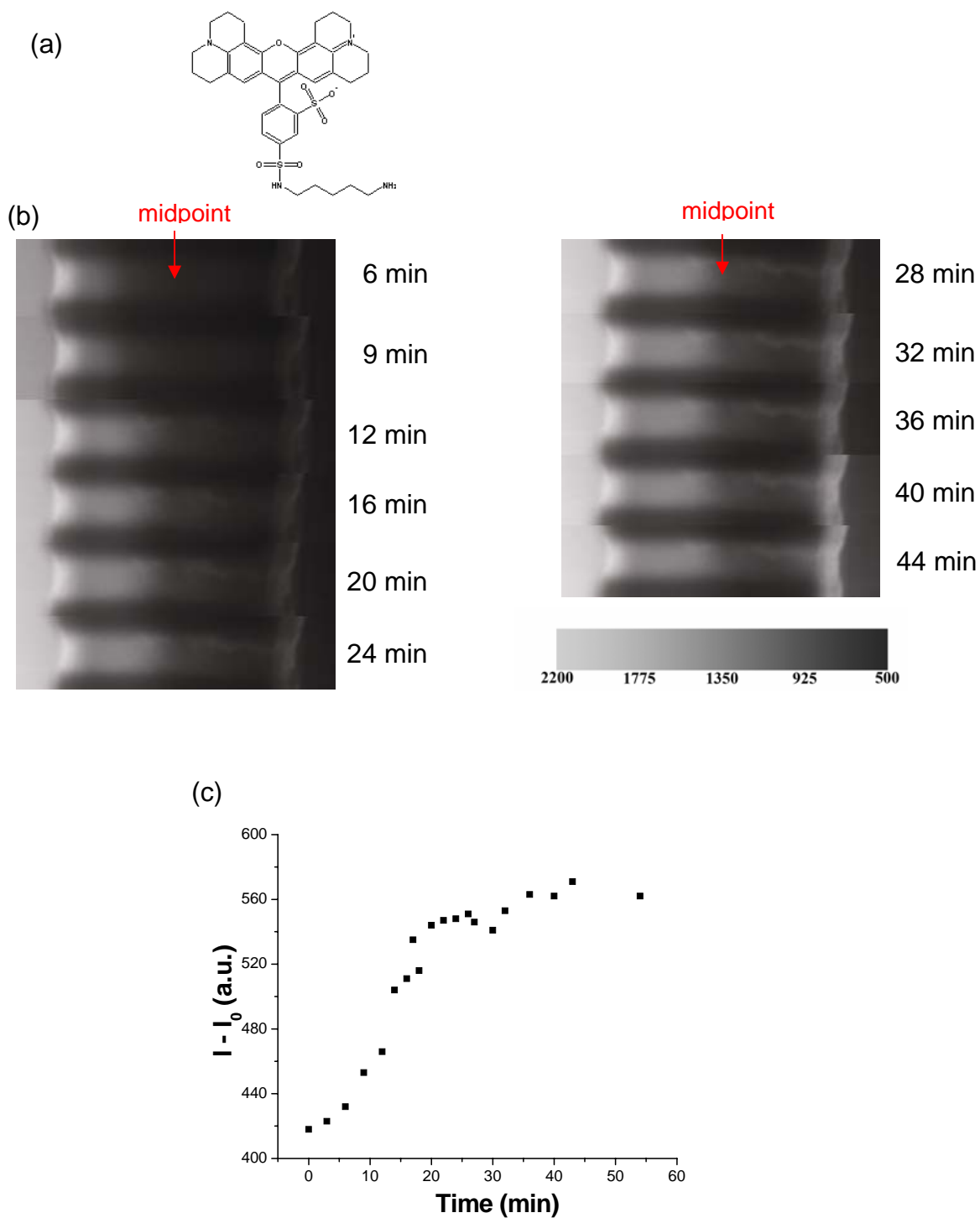
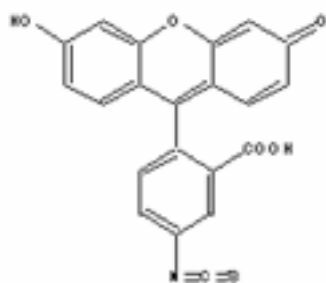


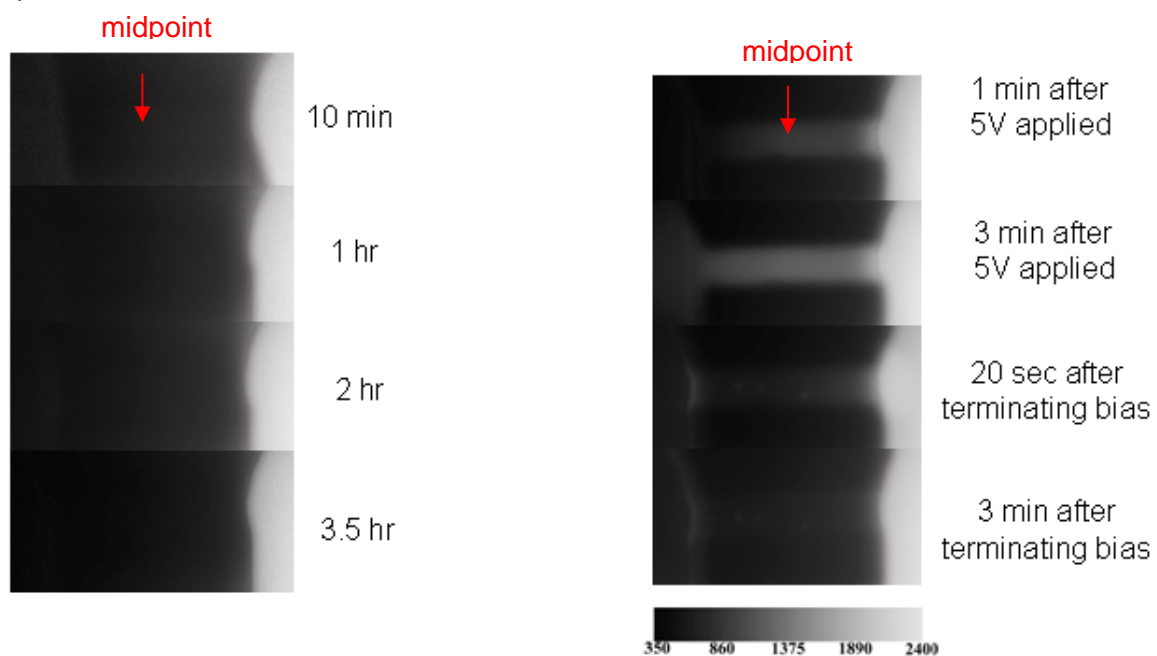
**Figure 4-4.** Diffusion of a cationic dye. (a) Molecular structure of Sulforhodamine 101 cadaverine used as a cationic dye. (b) Fluorescence images over the nanochannel regions taken during the diffusion of the cationic dye. The channel width is about 4  $\mu\text{m}$ . (c)

Background subtracted fluorescence intensity at the midpoint of the nanochannel shown in (b).

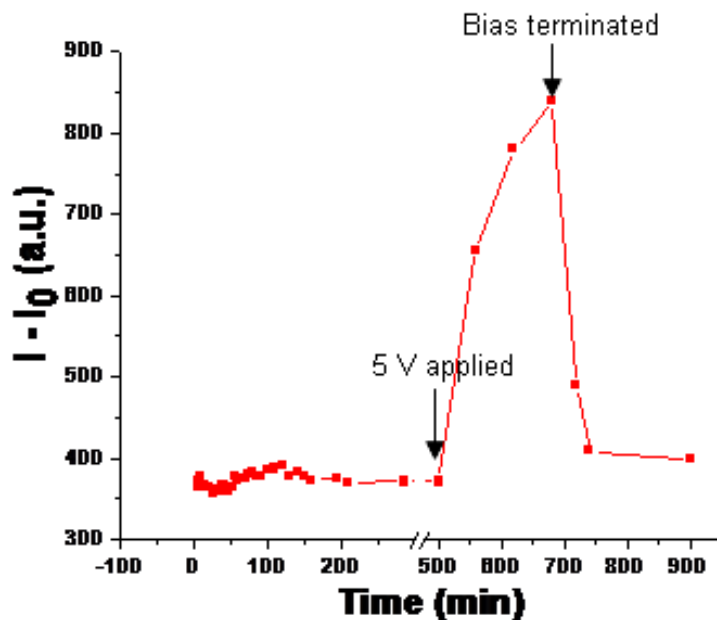
(a)



(b)



(c)



(d)

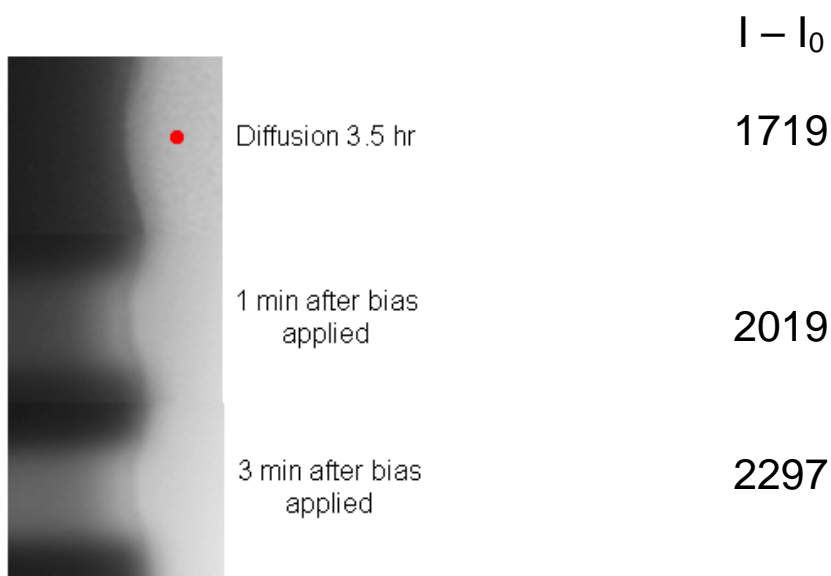


**Figure 4-5.** Diffusion of an anionic dye. (a) Molecular structure of fluorescein isothiocyanate (FITC) used as an anionic dye. (b) Fluorescence images over the nanochannel regions taken during the diffusion and bias application. The channel width is about 4  $\mu\text{m}$ . (c) Background subtracted fluorescence intensity at the midpoint of the nanochannel shown in (b). (d) High-resolution fluorescence images at the interface

between the nanochannel and the right microchannel. Background subtracted fluorescence intensities measured at the indicated point in the fluorescence image are also presented. Increased fluorescence intensity at the interface indicates a local dye accumulation due to the potential energy barrier.

Several things are noticeable from these diffusion data for the dyes carrying different charges.

First, as expected from the electrostatic interactions, the cationic and anionic dyes showed apparent difference in the diffusion efficiency. The fluorescence intensity by the cationic dye increased gradually with time, whereas little or no diffusion was observed for the anionic dye, though measured over a longer period ( $> 3$  hours). Again, the opposite diffusion trends between these dyes are indicative of the unipolar condition inside the nanochannel where the positive ions are dominant. In particular, the impaired diffusion of the anionic dye suggests significant potential barrier originated from the negative surface charge.

Second, in the case of anionic dye, the external bias could modulate the ionic transport. As +5 V was applied to the left microchannel, the ionic transport of the anionic dye was enabled and clear fluorescence intensity appeared in the nanochannel. This phenomenon is illustrated in the image taken at one minute after the bias was held to the left microchannel (figure 4-5b). At this moment, it was likely that the front end of the dye was passing the 4/5 point of the nanochannel and continuously moving toward the left microchannel. The image taken after 3 minutes of the bias application shows clearly that the dye diffused through the nanochannel. The source of the electrophoretic ionic flux lies in the fact that the external bias can overcome the electric potential barrier generated by the nanochannel surface charges. Fluorescence images were taken even after the

external bias was terminated, and interestingly, the anionic dyes were drained from the nanochannel immediately (two lowermost images in the right panel of figure 4-5b). The image taken 20 seconds after terminating the bias shows a slightly higher fluorescence intensity at the interface between the nanochannel and the right microchannel due to the dye molecule draining. The immediate draining of the dye from the nanochannel also reflects the potential barrier inside the nanochannel. The fact that the nanochannel looks brighter than before the bias was applied might be due to adsorbed dyes during the bias-driven electrophoretic transport. A similar bias application measurement was performed for the cationic dye as a subsequent experiment to what is shown in figure 4-4. After the cationic dye diffused through to the right microchannel (same orientation as figure 4-4), -5 V was applied to the left channel with the intention of attracting the cationic dye back toward the left side. An apparent fluorescence intensity decrease was observed on the right microchannel suggesting the electrophoretic movement of the cationic dye in the opposite direction to the diffusion (data not shown). However, the intensity decrease during the bias application was not as steep as with the anionic dye, perhaps due to low fluorescence intensity at the initial point of the bias application.

Third, in case of the anionic dye, a dye accumulation related to the local potential barrier was observed at the interface between the nanochannel and the right microchannel upon the bias application. High-resolution fluorescence images focusing on the interface are presented in figure 4-5d. As indicated by the background subtracted fluorescence intensity, the fluorescence intensity at the interface increased upon the bias application. This increase suggests that while the dyes are electrophoretically driven toward the left

microchannel, they are accumulated locally at the interface due to the potential barrier related to the nanochannel surface charge.

Finally, diffusivity ( $D$ ) of the cationic dye may be approximately estimated by  $D \sim l^2/t = (20 \text{ }\mu\text{m})^2/(10 \text{ min}) = 6.7 \times 10^{-13} \text{ m}^2/\text{s}$ . This value is roughly two orders of magnitude smaller than a typical small molecule diffusivity in dilute solution, thus suggesting that the interaction with the nanochannel wall decreases the diffusivity of the dye significantly.

The diffusion data of the oppositely charged dyes suggest that the nanochannel device could serve as a charge identifier for molecules whose charge status is unknown in certain conditions. In order to verify the idea, a zwitterion was tested. Texas red sulfonyl chloride (Molecular Probes) was chosen as the zwitterion counterpart to the sulforhodamine 101 cadaverine, allowing us to test the charge effect exclusively while maintaining other intrinsic properties. As shown in figure 4-6a, Texas red sulfonyl chloride has amine and sulfo functional groups as positive and negative charge sites, respectively. At this point, it proved to be very interesting to monitor the diffusion of the zwitterions through the nanochannel because both positive and negative sites must be strongly charged around neutral pH. The diffusion data for the zwitterion is presented in figure 4-6.

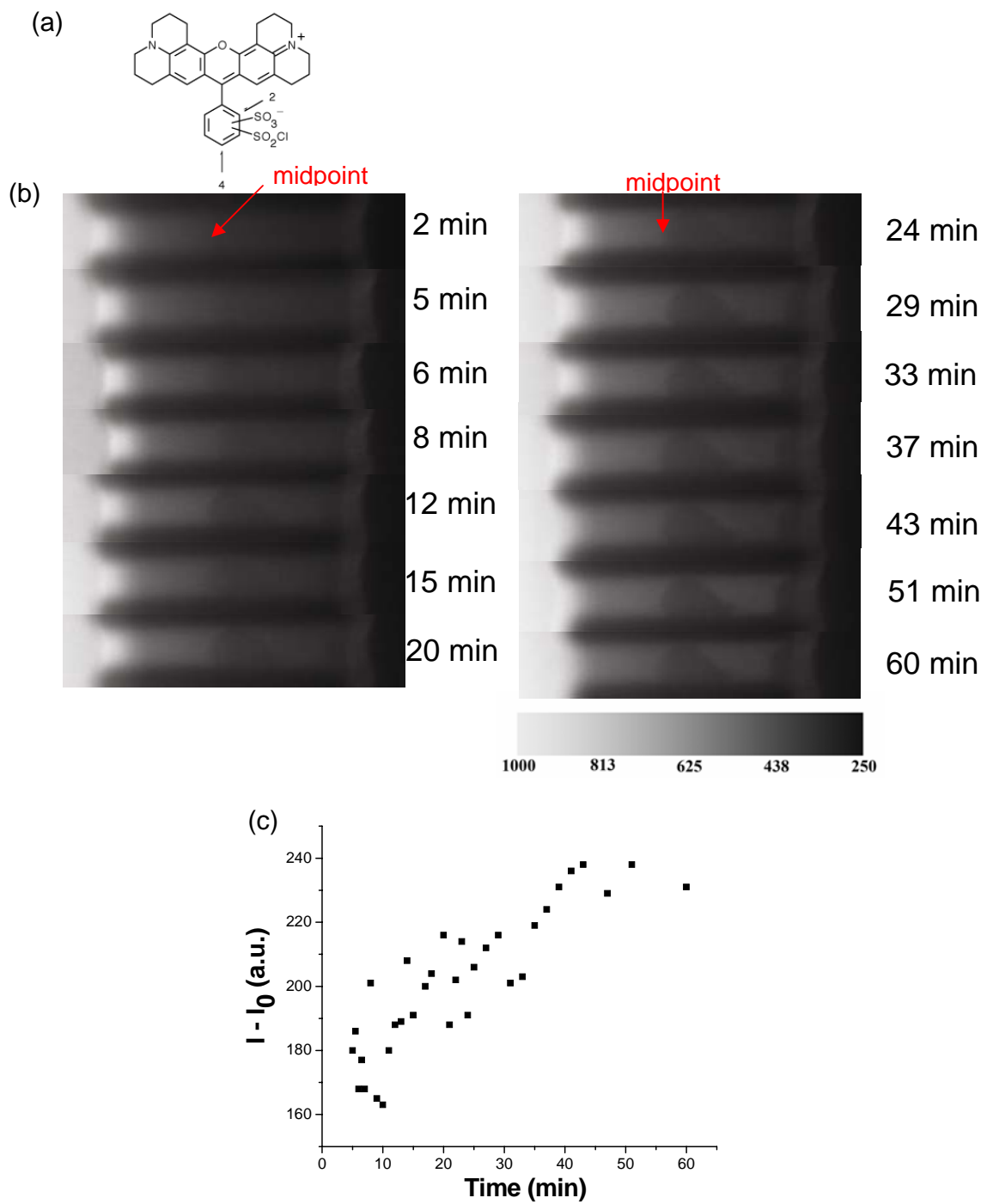


**Figure 4-6.** Diffusion of a zwitterionic dye. (a) Molecular structure of Texas red sulfonyle chloride used as a zwitterionic dye. (b) Fluorescence images over the nanochannel

regions taken during the diffusion. The dark spot in the middle of the nanochannel is believed to be a residue from the previous measurements. The channel width is about 4  $\mu\text{m}$ . (c) Background subtracted fluorescence intensity measured at the midpoint of two different nanochannels.

The devices had to be recycled repeatedly for clear comparisons over the various dyes. In characterizing the zwitterionic dyes, in particular, the nanochannel appeared to have residues on the channel surface from the previous measurements, occurring as a dark spot in the middle of the channel (figure 4-6). Nevertheless, apparent diffusion was observed in the nanochannel, which suggests that the zwitterionic dye tested is not at least negatively charged. Because the zwitterionic dyes have two ionized sites of opposite polarities, it is expected that the dyes are more likely charged with either polarity rather than existing exactly neutral. From the observed diffusion, therefore, the net charge of the dye is expected to be positive. In order to test the hypothesis, biases of opposite polarities ( $\pm 5$  V) were applied sequentially while fluorescence images were taken periodically. Figure 4-7 presents those images and fluorescence intensity differences between both sides of microchannel. As shown in the figure, the dyes were driven toward lower potential sides at both bias applications. This electrophoretic transport validates the initial hypothesis that the dye is partially positively charged. Although further analysis is required to understand the origin of the partial charge, it could be presumed that the observed behavior is reflective of the fluidic environment inside the nanochannel where positive ions are dominant.

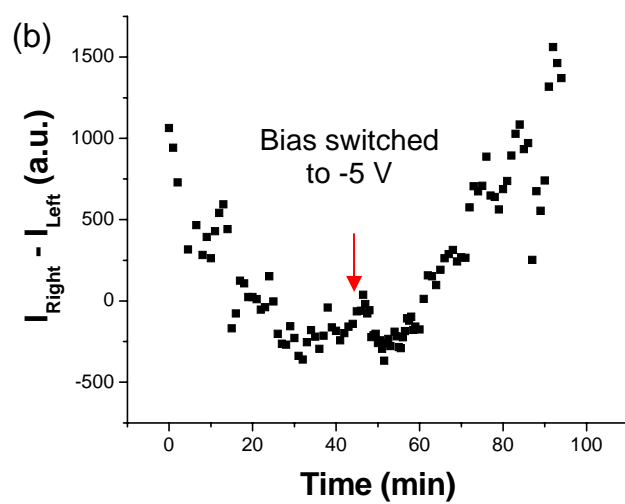
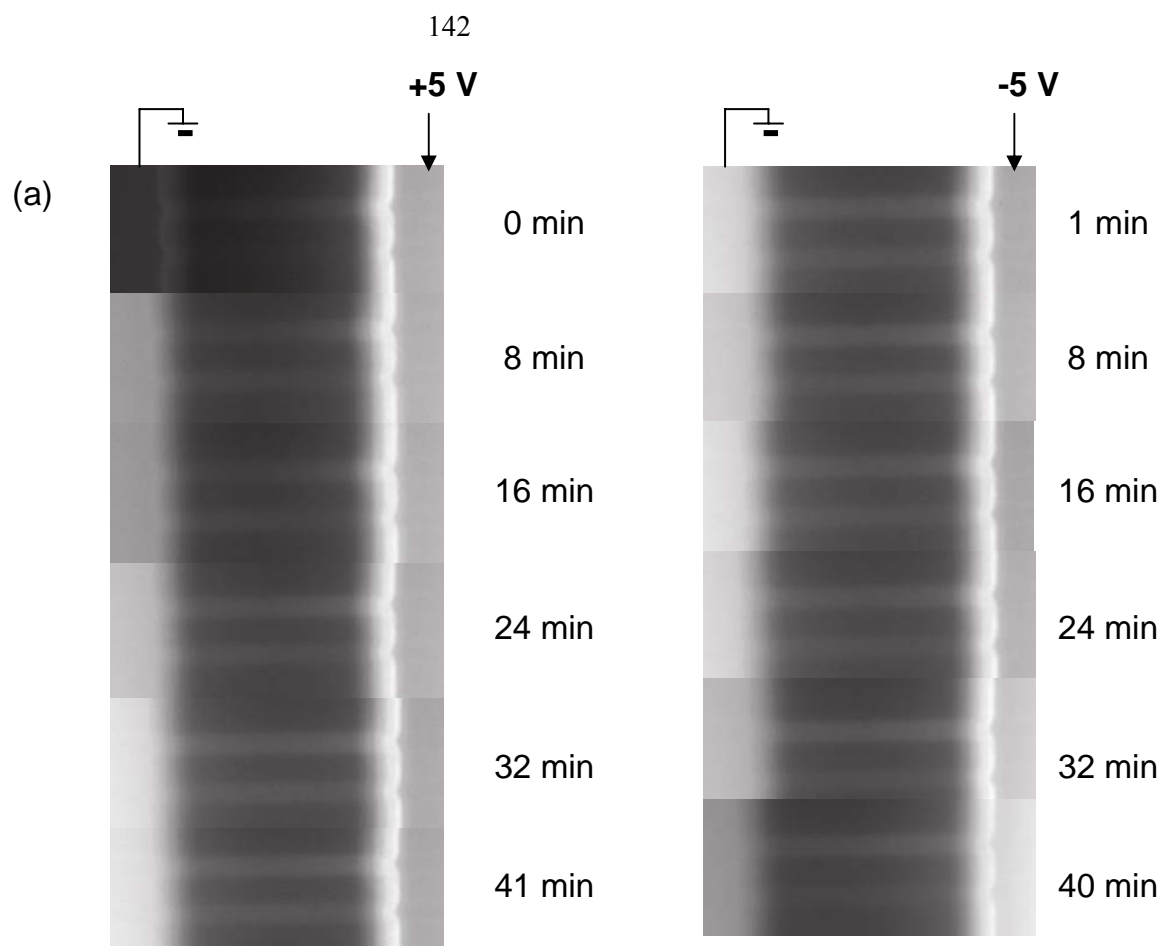


**Figure 4-7.** Bias measurements for the charge determination of the zwitterionic dye. (a) Positive (left panel) and then negative biases (right panel) are applied continuously to the right microchannel. It was visualized that the left microchannel becomes brighter

compared to the right one upon +5V application, whereas the brightness was switched upon -5 V application. (b) Fluorescence intensity difference between both sides of the microchannel. The point where the bias was switched to -5 V is indicated.

With nanoporous membranes, it is known that neutral molecules do not interact electrostatically with the surface of the membrane, thereby resulting in a larger flux across the membrane than charged molecules (15-18). In our measurements, the concentration difference between two specific points with regard to time should give diffusivity. Due to fabrication problems from the repeated device recycles, such as a minor leaking on the left side in figure 4-4, we require further measurements for a complete diffusivity analysis. The diffusivity analysis would provide better idea on the charge state of the zwitterionic dye by comparing its diffusivity against that of the cationic dye.

The charge-dependent diffusion not only indicates the unipolar characteristic of the nanochannel, but also implies that this platform could serve as a molecular separator or a charge identifier. The similar separation could be realized in a lower concentration of target molecules. Especially, by implementing a more sophisticated optical set-up, such as dark-field microscope that can image the target molecules attached to nanoparticles, the resolution of detecting the passage of the target molecules could be improved further. In summary, this technology suggests the possibility of a new type of column at a level close to single molecule resolution.

## **4.4 Conclusion and Future Work: Toward Quantification of Peptide Isoelectric Point via Gating Bias**

Due to channel dimensions smaller than the Debye screening length, nanofluidics depicts interesting fundamental phenomena on ionic transport. Among those, the unipolar condition is most representative. Under the unipolar condition, the ions with different polarities should be considered separately because the surface charges on the nanochannel wall exert an opposite effect on those ions. To understand the system clearly, various parameters such as surface charge, ionic strength, external bias and charge-valency of carrying ions should be considered simultaneously because they are correlated to one another. The charge-dependent ionic diffusion has been observed via fluorescent dye molecules. The charge accumulation and depletion has been also observed upon external bias applicaiton. All results thus far can be explained within a consistent picture of a unipolar environment. Furthermore, the unipolar characteristic could be applied to separate molecules based on the charges as well as to identify the charge state of unknown molecules. Also, those applications should be possible for extremely small amounts of sample.

The project will be further expanded to detect a variety of target molecules including polymers, DNA and peptides. In device optimization, on the other hand, gating electrodes will be integrated over the nanochannel region to obtain a fine control over the surface charge. Among many candidates, the primary focus will be on quantification of peptide isoelectric points by adjusting the gating bias. About 5-mer length peptides, tagged with fluorescent dyes at the last residue, have been already synthesized by a manual coupling method. Fluorescence intensity will be obtained while the gating bias is

varied. The fluorescence intensity is expected to change most abruptly when the nanochannel surface charge, which is modulated by the gating bias, is close to the charge of target molecules. In other words, when half of the peptide population is positively charged and the other half is negatively charged, the change in fluorescence intensity would be most significant. Currently, two oppositely-charged polypeptides, such as polyaspartate and polylysine are being tested.

Once the idea is experimentally realized, its application would be multifold. One could separate a particular peptide from mixture by adjusting the gating bias. In addition, as a detection tool, the nanofluidic device could identify peptides based on the isoelectric points at a level close to a single molecule. Finally, its usage could be further extended to sequence proteins. Placing an unknown protein into solution within the nanochannels could allow the determination of its isoelectric point. The next step would be to enzymatically cleave the protein and flow the digested fragments through nanochannels, thereby determining the isoelectric points of the digested fragments. Repeating this procedure a few times would result in ascertaining the isoelectric points of many small peptides. Combining the knowledge of the amino-acid specific cleavage sites, in conjunction with the isoelectric point of the peptide fragments, the nanofluidic device should provide sufficient information to enable identification of the original protein. This would be an alternative to the more common mass spectrometry based method of peptide sequencing (19). The advantages of nanofluidics are that these devices could be operated in parallel and would require very little quantities of proteins, thus perhaps enabling protein discovery.

## 4.5 References

1. Kasianowicz, J. J., Brandin, E., Branton, D. & Deamer, D. W. (1996) *Proc. Nat. Acad. Sci.* 93, 13770-13773.
2. Howorka, S., Cheley, S. & Bayley, H. (2001) *Nat. Biotechnol.* 19, 636-639.
3. Fan, R., Karnik, R., Yue, M., Li, D. Y., Majumdar, A. & Yang, P. D. (2005) *Nano Lett.* 5, 1633-1637.
4. Karnik, R., Castelino, K., Fan, R., Yang, P. & Majumdar, A. (2005) *Nano Lett.* 5, 1638-1642.
5. Karnik, R., Fan, R., Yue, M., Li, D. Y., Yang, P. D. & Majumdar, A. (2005) *Nano Lett.* 5, 943-948.
6. Stein, D., Kruithof, M. & Dekker, C. (2004) *Phys. Rev. Lett.* 93.
7. Israelachvili, J. (2003) *Intermolecular and surface forces*, Academic Press.
8. Fan, R., Yue, M., Karnik, R., Majumdar, A. & Yang, P. D. (2005) *Phys. Rev. Lett.* 95.
9. Stein, D., Kruithof, M. & Dekker, C. (2004) *Phys. Rev. Lett.* 93.
10. Karnik, R., Castelino, K., Fan, R., Yang, P. & Majumdar, A. (2005) *Nano Lett.* 5, 1638-1642.
11. Fu, J., Schoch, R. B., Stevens, A. L., Tannenbaum, S. R. & Han, J. (2007) *Nature Nanotechnol.* 2, 121-128.
12. Melosh, N. A., Boukai, A., Diana, F., Gerardot, B., Badolato, A., Petroff, P. M. & Heath, J. R. (2003) *Science* 300, 112-115.
13. Daiguji, H., Yang, P. D., Szeri, A. J. & Majumdar, A. (2004) *Nano Lett.* 4, 2315-2321.

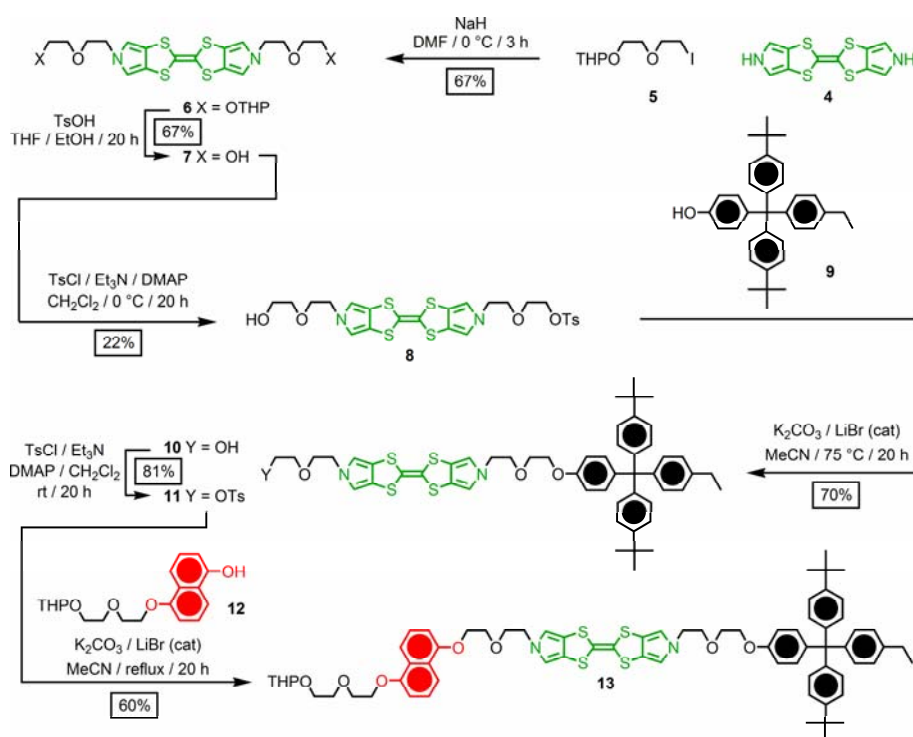
14. Daiguji, H., Yang, P. D. & Majumdar, A. (2004) *Nano Lett.* 4, 137-142.
15. Burns, D. B. & Zydney, A. L. (1999) *Biotech. & Bioeng.* 64, 27-37.
16. Chun, K. Y. & Stroeve, P. (2002) *Langmuir* 18, 4653-4658.
17. Ku, J. R. & Stroeve, P. (2004) *Langmuir* 20, 2030-2032.
18. Lee, S. B. & Martin, C. R. (2001) *Anal. Chem.* 73, 768-775.
19. Wilm, M., Shevchenko, A., Houthaeve, T., Breit, S., Schweigerer, L., Fotsis, T. & Mann, M. (1996) *Nature* 379, 466-469.

## Appendix A

### Syntheses of the [2]rotaxanes **RBPTTF•4PF<sub>6</sub>** and **RBLOCK•4PF<sub>6</sub>**

#### A-1. Synthesis of the Amphiphilic [2]Rotaxane **RBPTTF•4PF<sub>6</sub>**

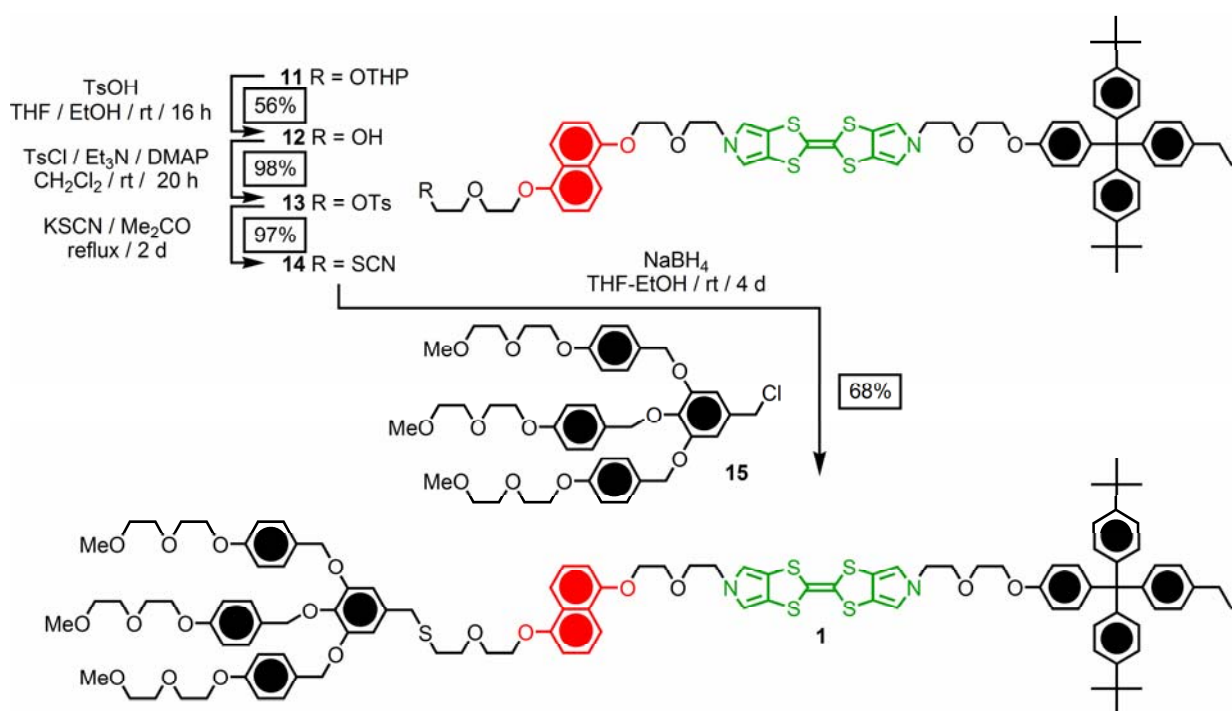
The [2]rotaxane **RBPTTF•4PF<sub>6</sub>** was synthesized according to the routes outlined sequentially in Schemes A1–A3. Alkylation of BPTTF<sup>i</sup> **4** with 2-[2-(2-iodoethoxy)ethoxy]tetrahydropyran<sup>ii</sup> (**5**) in DMF gave (Scheme A1) the BPTTF derivative **6** in 67% yield. Removal of the



**Scheme A1.** Synthesis of the semi-dumbbell compound **13**.

THP-protecting groups with *p*-toluenesulfonic acid (TsOH) gave the diol **7** in 67% yield. The monotosylate **8** was obtained in 22% yield by reaction of the diol **7** with one equivalent of *p*-toluenesulfonyl chloride (TsCl). Alkylation of the hydrophobic

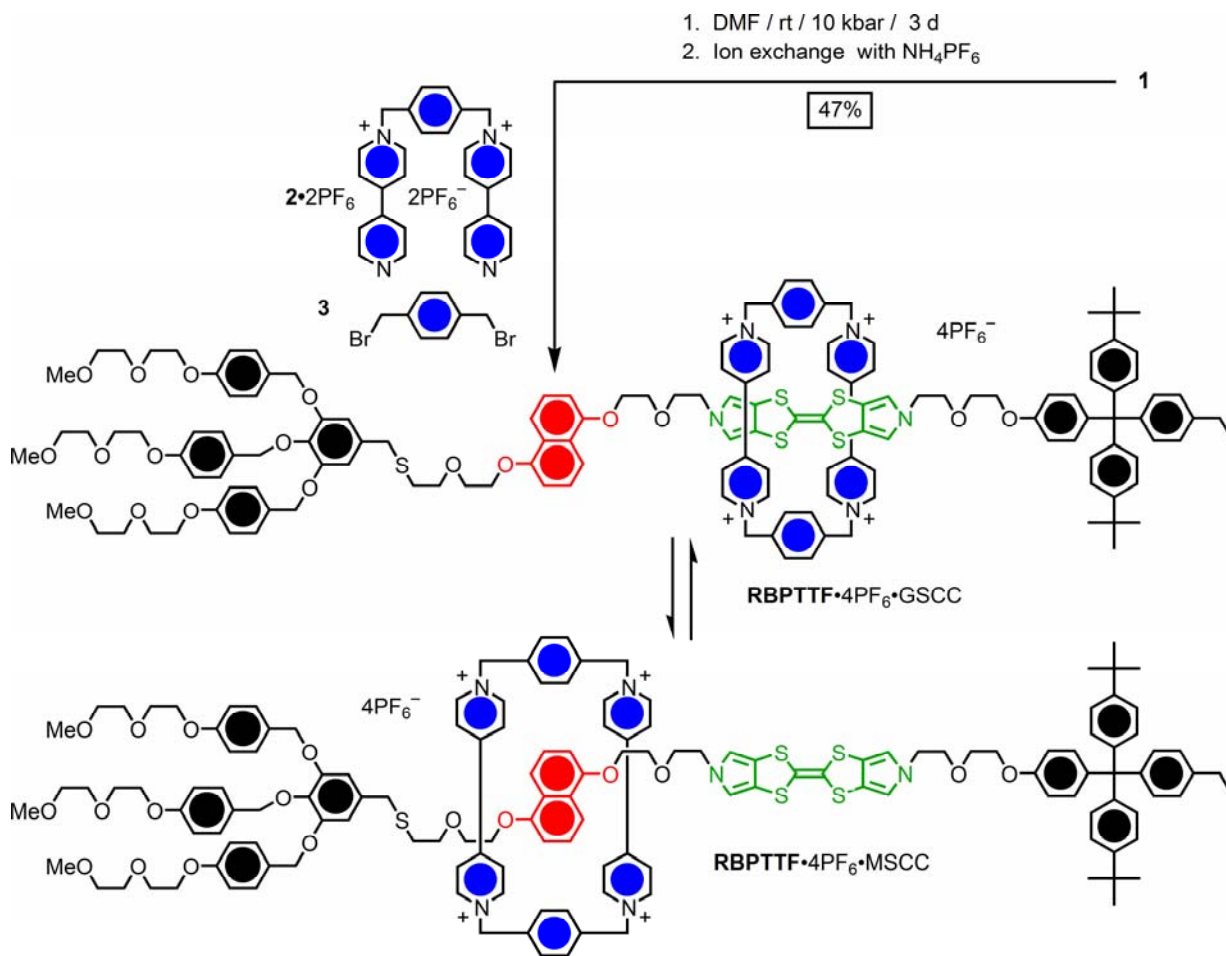
tetraarylmethane-based stopper<sup>iii</sup> **9** with **8** in MeCN in the presence of K<sub>2</sub>CO<sub>3</sub> gave (70%) the alcohol **10**, which was tosylated using TsCl in CH<sub>2</sub>Cl<sub>2</sub> affording **11** in 81% yield. Subsequently, **11** was reacted with the DNP derivative<sup>iv</sup> **12** under alkylation conditions (K<sub>2</sub>CO<sub>3</sub> / LiBr / MeCN) affording the BPTTF derivative **13** in 60% yield, which on treatment with TsOH in THF/EtOH, gave (Scheme A2) the alcohol **14** in 56% yield. The free hydroxyl function in compound **14** was thereafter converted to a tosylate group in 98% yield (**14**→**15**) and then to a thiocyanate group in 97% yield (**15**→**16**). The thiocyanate group was reduced in situ with NaBH<sub>4</sub>, and the resulting thiolate was subsequently coupled with the hydrophilic chloride<sup>iii</sup> **17** in THF/EtOH to



**Scheme A2.** Synthesis of the dumbbell compound **1**.

give the dumbbell **1** in 68% yield. Finally, the [2]rotaxane **RBPTTF**•4PF<sub>6</sub> was self-assembled (Scheme A3) under high pressure conditions by using the dumbbell

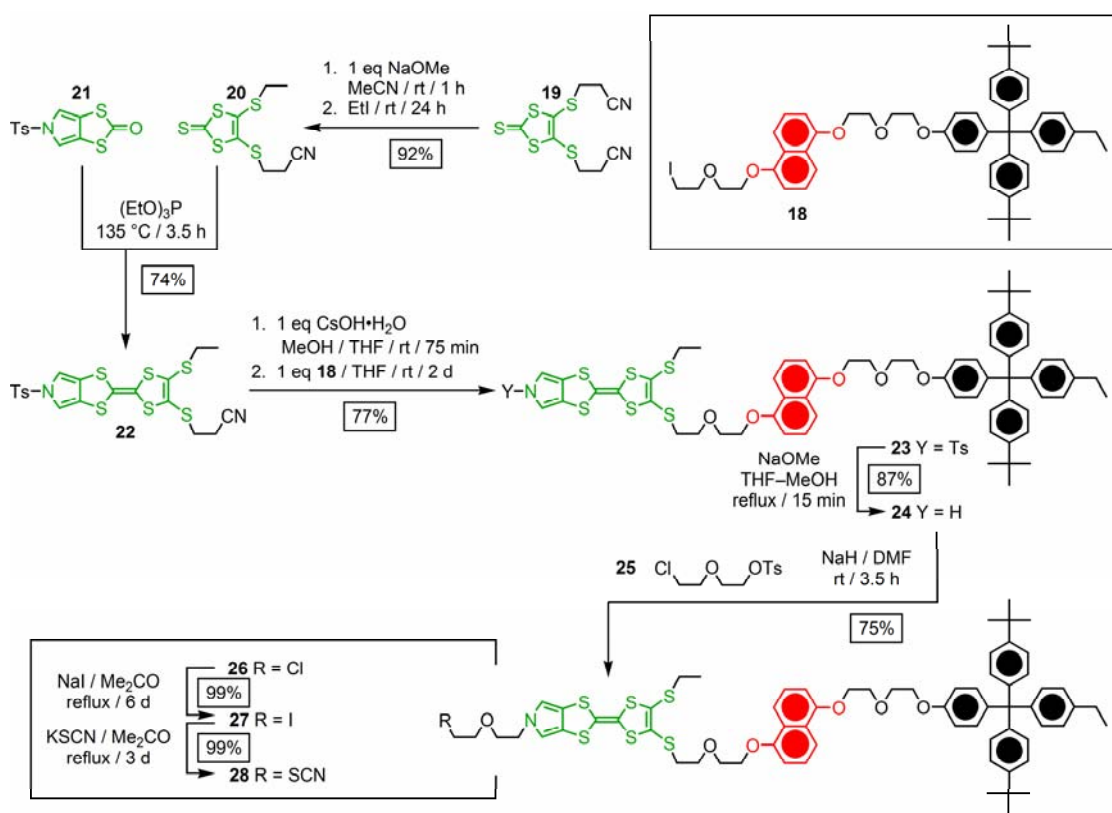
compound **1** as the template for the formation of the encircling CBPQT<sup>4+</sup> tetracation and the [2]rotaxane **RBPTTF**•4PF<sub>6</sub> was isolated in 47% yield from a mixture of the dumbbell compound **1**, the dicationic precursor<sup>v</sup> **2**•2PF<sub>6</sub>, and the dibromide **3** after they had been subjected to a 10 kbar pressure in DMF at room temperature for 3 days.



**Scheme A3.** Synthesis of the bistable [2]rotaxane **RBPTTF**•4PF<sub>6</sub>.

## A-2. Synthesis of the Amphiphilic [2]Rotaxane RBLOCK•4PF<sub>6</sub>

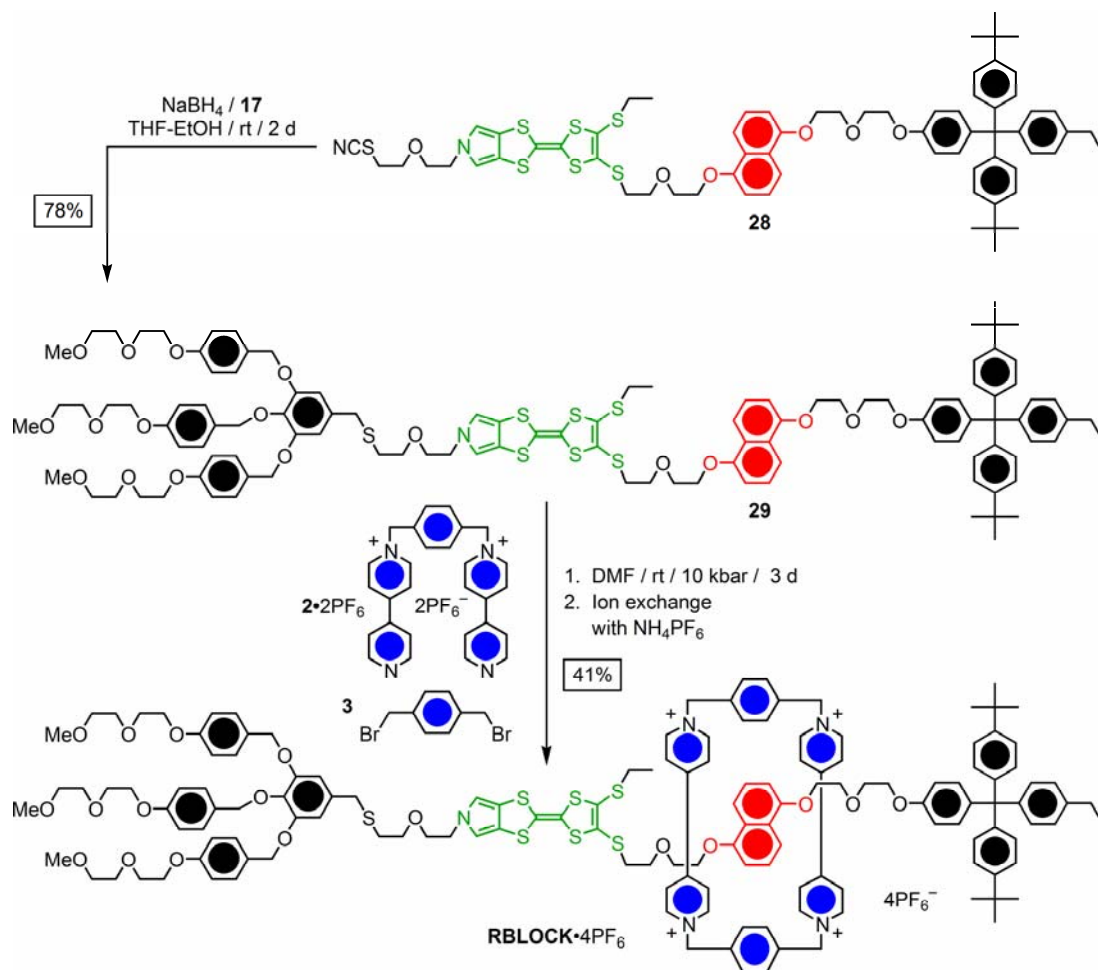
The [2]rotaxane **RBLOCK•4PF<sub>6</sub>** was synthesized according to the routes outlined sequentially in Schemes A4 and A5. A THF solution of 4,5-bis(2-cyanoethylthio)-1,3-dithiole-2-thione<sup>vi</sup> (**19**) was treated with one equivalent of NaOMe. This procedure generated the monothiolate, which was alkylated with EtI affording compound **20** in 92% yield. Cross-coupling of 5-tosyl-(1,3)-dithiolo[4,5-*c*]pyrrole-2-one<sup>i</sup> (**21**) with three equivalents of the thione **20** in neat (EtO)<sub>3</sub>P gave



**Scheme A4.** Synthesis of the semi-dumbbell compound **28**.

(Scheme A4) the MPTTF derivative **22** (74%) in gram quantities after column chromatography. The iodide<sup>vii</sup> **18** was coupled with the MPTTF building block **22**, following its in situ deprotection with one equivalent of CsOH•H<sub>2</sub>O to give **23** in 87%

yield. The tosyl protecting group on the MPTTF unit was removed in good yield (87%) using NaOMe in a THF/MeOH mixture. The resultant pyrrole nitrogen in **24** was alkylated with compound<sup>viii</sup> **25**, affording the chloride **26** in 75% yield. The chloride in compound **26** was initially converted to (**26**→**27**) an iodide in 99% yield and then to (**27**→**28**) a thiocyanate group in 99% yield. The thiocyanate group was reduced in situ with NaBH<sub>4</sub>, and the resulting thiolate was subsequently coupled with the hydrophilic chloride<sup>iii</sup> **17** in THF to give the dumbbell **29** in 78% yield. Finally, the [2]rotaxane **RBLOCK**•4PF<sub>6</sub> was self-assembled (Scheme A5) under high pressure conditions by using the dumbbell compound **29** as the template for the formation of the encircling CBPQT<sup>4+</sup> tetracation and the [2]rotaxane **RBLOCK**•4PF<sub>6</sub> was isolated in 41% yield from a



**Scheme A5.** Synthesis of the [2]rotaxane **RBLOCK**•4PF<sub>6</sub>.

mixture of the dumbbell compound **29**, the dicationic precursor<sup>v</sup> **2**•2PF<sub>6</sub>, and the dibromide **3** after they had been subjected to a 10 kbar pressure in DMF at room temperature for 3 days.

### A-3. Experimental Details for the Synthesis of the [2]Rotaxanes

**General methods:** Chemicals were purchased from Aldrich and were used as received, unless indicated otherwise. Bis(pyrrolo[3,4-*d*])tetrathiafulvalene<sup>i</sup> (**4**) (Scheme

A1), 2-(2-iododethoxy)-ethyl-*p*-toluenesulfonate<sup>ii</sup> (**5**) (Scheme A1), 4-[bis(4-*tert*-butylphenyl)(4-ethylphenyl)methyl]-phenol<sup>iii</sup> (**9**) (Scheme A1), compound<sup>iv</sup> **12** (Scheme A1), the chloride<sup>iii</sup> **17** (Schemes A2 and A4), 1,1''-[1,4-phenylenebis(methylene)]bis(4,4'-bipyridin-1-ium) bis(hexafluorophosphate)<sup>v</sup> (**16**•2PF<sub>6</sub>) (Schemes A3 and A5), the iodide<sup>vii</sup> **18** (Scheme A4), 4,5-bis(2-cyanoethylthio)-1,3-dithiole-2-thione<sup>vi</sup> (**19**) (Scheme A4), 5-tosyl-(1,3)-dithiolo-[4,5-*c*]pyrrole-2-one<sup>i</sup> (**21**) (Scheme A4), and 2-(2-chloroethoxy)-ethyl-*p*-toluenesulfonate<sup>viii</sup> (**25**) (Scheme A4) were all prepared according to literature procedures. Solvents were dried according to literature procedures.<sup>ix</sup> All reactions were carried out under an anhydrous nitrogen atmosphere. High pressure experiments were carried out in a teflon-tube on a Psika high pressure apparatus. Thin-layer chromatography (TLC) was carried out using aluminium sheets pre-coated with silica gel 60F (Merck 5554). The plates were inspected under UV light and, if required, developed in I<sub>2</sub> vapor. Column chromatography was carried out using silica gel 60F (Merck 9385, 0.040–0.063 mm). Deactivated SiO<sub>2</sub> was prepared by stirring the silica gel in CH<sub>2</sub>Cl<sub>2</sub> containing 2% Et<sub>3</sub>N for 10 min before it was filtered, washed with CH<sub>2</sub>Cl<sub>2</sub> and dried. Melting points were determined on a Büchi melting point apparatus and are uncorrected. <sup>1</sup>H NMR spectra were recorded at room temperature on a Bruker ARX500 spectrometer (500 MHz), Bruker ARX400 spectrometer (400 MHz), or on a Gemini-300BB instrument (300 MHz), using residual solvent as the internal standard. <sup>13</sup>C NMR spectra were recorded at room temperature on a Gemini-300BB instrument (75 MHz), using residual solvent as the internal standard. <sup>19</sup>F NMR spectra were recorded at room temperature on a Bruker ARX400 spectrometer (376 MHz), while <sup>31</sup>P NMR spectra were recorded at room temperature on Bruker ARX400 instrument (161 MHz).

All chemical shifts are quoted on a  $\delta$  scale, and all coupling constants ( $J$ ) are expressed in Hertz (Hz). The following abbreviations are used in listing the NMR spectra: s = singlet, d = doublet, t = triplet, q = quartet, and bs = broad singlet, and m = multiplet. Samples were prepared using  $\text{CDCl}_3$ ,  $\text{CD}_3\text{COCD}_3$ , or  $\text{CD}_3\text{SOCD}_3$  purchased from Cambridge Isotope Labs. Electron impact ionization mass spectrometry (EI-MS) was performed on a Varian MAT 311A instrument and matrix-assisted laser-desorption/ionization time-of-flight mass spectrometry (MALDI-TOF-MS) was performed on a Kratos Kompact MALDI-TOF instrument, utilizing a 2,5-dihydroxybenzoic acid matrix, high resolution Fourier Transform matrix-assisted laser-desorption/ionisation mass spectrometry (HiRes-FT-MALDI-MS) was performed on an IonSpec 4.7 tesla Ultima Fourier Transform mass spectrometer, utilizing a 2,5-dihydroxybenzoic acid (DHP) matrix, while electrospray mass spectra (ES-MS) were obtained from a from a Sciex API III<sup>+</sup> mass spectrometer. Infrared (IR) spectra were recorded on a Perkin-Elmer 580 spectrophotometer. UV-vis spectra were recorded at room temperature on a Shimadzu UV-160 instrument. Microanalyses were performed by the Atlantic Microlab, Inc., Atlanta, Georgia.

**Compound 6.** Compound **4** (0.80 g, 2.83 mmol) was dissolved in anhydrous DMF (30 mL), cooled to 0 °C, and degassed ( $\text{N}_2$ , 10 min) before the iodide **5** (2.50 g, 8.33 mmol) followed by NaH (0.80 g of a 60% suspension in mineral oil, 20.0 mmol) was added to the yellow solution. The reaction mixture was stirred for 3 h at 0 °C, whereupon the reaction mixture was diluted with  $\text{CH}_2\text{Cl}_2$  (500 mL), washed with brine (10  $\times$  150 mL) and dried ( $\text{MgSO}_4$ ). Removal of the solvent gave a brown oil which was purified by column chromatography (deactivated  $\text{SiO}_2$ :  $\text{CH}_2\text{Cl}_2/\text{MeOH}$  19:1). The broad yellow band ( $R_f = 0.6$ ) was collected and concentrated, affording 1.19 g (67%) of the title

compound **6** as a yellow oil. Data for **6**:  $^1\text{H}$  NMR ( $\text{CD}_3\text{SOCD}_3$ , 300 MHz)  $\delta$  1.40–1.80 (m, 12H), 3.40–4.00 (m, 20H), 4.54 (bs, 2H), 6.82 (s, 4H);  $^{13}\text{C}$  NMR ( $\text{CD}_3\text{SOCD}_3$ , 75 MHz)  $\delta$  19.6, 25.6, 30.8, 50.3, 61.7, 66.4, 70.1, 70.7, 98.5, 114.2, 117.2, 119.5; MS(EI)  $m/z$  626 ( $\text{M}^+$ , 24), 542 (18), 458 (10). Anal. Calcd for  $\text{C}_{28}\text{H}_{38}\text{N}_2\text{O}_6\text{S}_4$ : C, 53.65; H, 6.11; N, 4.47. Found: C, 53.78; H, 6.09; N, 4.43.

**Compound 7.** A solution of compound **6** (1.14 g, 1.82 mmol) in THF–EtOH (50 mL, 1:1 v/v) was degassed ( $\text{N}_2$ , 10 min) before  $\text{TsOH}\cdot\text{H}_2\text{O}$  (~10 mg, cat) was added. The yellow solution was stirred for 20 h at room temperature, whereupon it was diluted with  $\text{CH}_2\text{Cl}_2$  (100 mL). The combined organic phase was washed with a saturated aqueous  $\text{NaHCO}_3$  solution (200 mL),  $\text{H}_2\text{O}$  (300 mL) and dried ( $\text{MgSO}_4$ ). Concentration in vacuo gave a yellow powder, which was subjected to column chromatography (deactivated  $\text{SiO}_2$ :  $\text{CH}_2\text{Cl}_2/\text{MeOH}$  24:1). The greenish yellow band ( $R_f = 0.3$ ) was collected and the solvent evaporated to give 0.56 g (67%) of the title compound **7** as a yellow powder. Data for **7**: mp 138–139 °C;  $^1\text{H}$  NMR ( $\text{CD}_3\text{SOCD}_3$ , 300 MHz)  $\delta$  3.39–3.42 (m, 8H), 3.64 (t,  $J = 5.2$  Hz, 4H), 4.00 (t,  $J = 5.2$  Hz, 4H), 4.59 (t,  $J = 5.2$  Hz, 2H), 6.82 (s, 4H);  $^{13}\text{C}$  NMR ( $\text{CD}_3\text{SOCD}_3$ , 75 MHz)  $\delta$  49.8, 60.2, 70.2, 72.2, 113.7, 116.7, 118.9; MS(MALDI–TOF)  $m/z$  458 ( $\text{M}^+$ , 100). Anal. Calcd for  $\text{C}_{18}\text{H}_{22}\text{N}_2\text{O}_4\text{S}_4$ : C, 47.14; H, 4.83; N, 6.11; S, 27.97. Found: C, 47.04; H, 4.83; N, 6.08; S, 27.73.

**Compound 8.**  $\text{TsCl}$  (0.57 g, 2.99 mmol) dissolved in anhydrous  $\text{CH}_2\text{Cl}_2$  (30 mL) was added dropwise over 20–30 min to an ice-cooled solution of the diol **7** (1.30 g, 2.83 mmol),  $\text{Et}_3\text{N}$  (2 mL, 1.5 g, 14 mmol), and DMAP (~10 mg, cat) in anhydrous  $\text{CH}_2\text{Cl}_2$  (90 mL). The reaction mixture was stirred for 20 h (0 °C to rt), whereupon  $\text{Al}_2\text{O}_3$  (10 g,

Brockmann 1, neutral) was added and the solvent removed. The resulting green powder was directly subjected to column chromatography (deactivated SiO<sub>2</sub>) and 0.90 g (41%) of the bistosylate was eluted with CH<sub>2</sub>Cl<sub>2</sub>, whereupon the eluent was changed to CH<sub>2</sub>Cl<sub>2</sub>/MeOH (99:1) and the yellow band (*R<sub>f</sub>* = 0.5) containing the desired monotosylate was collected and concentrated to give 0.38 g (22%) of the title compound **8** as a yellow solid. Finally, 0.45 g (34%) of the starting material **7** was eluted CH<sub>2</sub>Cl<sub>2</sub>/MeOH (23:2). Data for **8**: <sup>1</sup>H NMR (CD<sub>3</sub>SOCD<sub>3</sub>, 300 MHz) δ 2.42 (s, 3H), 3.36–3.66 (m, 10H), 3.93–4.11 (m, 6H), 4.59 (t, *J* = 5.2 Hz, 1H), 6.74 (s, 2H), 6.83 (s, 2H), 7.46 (d, *J* = 8.0 Hz, 2H), 7.75 (d, *J* = 8.0 Hz, 2H); <sup>13</sup>C NMR (CD<sub>3</sub>SOCD<sub>3</sub>, 75 MHz) δ 21.1, 49.5, 49.7, 60.2, 67.7, 69.8, 70.1, 70.2, 72.1, 113.6, 113.7, 116.7, 116.8, 118.9, 127.6, 130.1, 132.5, 144.9 (one line is missing/overlapping); MS(MALDI–TOF) *m/z* 612 (M<sup>+</sup>, 100). Anal. Calcd for C<sub>25</sub>H<sub>28</sub>N<sub>2</sub>O<sub>6</sub>S<sub>5</sub>: C, 49.00; H, 4.61; N, 4.57; S, 26.16. Found: C, 48.83; H, 4.66; N, 4.67; S, 25.97.

**Compound 10.** A solution of the monotosylate **8** (0.37 g, 0.60 mmol) and **9** (0.86 g, 1.80 mmol) in anhydrous MeCN (50 mL) containing K<sub>2</sub>CO<sub>3</sub> (0.50 g, 3.6 mmol), LiBr (10 mg, cat) and 18-crown-6 (~10 mg, cat), was heated at 75 °C for 20 h. After cooling down to room temperature the reaction mixture was filtered and the residue washed thoroughly with MeCN (20 mL). The combined organic phase filtrate was concentrated in vacuo and the yellow residue was purified by column chromatography (deactivated SiO<sub>2</sub>: CH<sub>2</sub>Cl<sub>2</sub>/Me<sub>2</sub>CO 97:3). The yellow band (*R<sub>f</sub>* = 0.2) was collected and the solvent evaporated to give 0.38 g (70%) of the title compound **10** as a yellow foam. Data for **10**: <sup>1</sup>H NMR (CD<sub>3</sub>SOCD<sub>3</sub>, 300 MHz) δ 1.17 (t, *J* = 7.6 Hz, 3H), 1.26 (s, 18H), 2.53 (q, *J* = 7.6 Hz, 2H), 3.39–3.49 (m, 4H), 3.62–3.71 (m, 6H), 3.99–4.02 (m, 6H), 4.59 (t, *J* = 5.2

Hz, 1H), 6.80–6.84 (m, 6H), 7.01–7.12 (m, 10H), 7.28–7.31 (m, 4H); MS(EI)  $m/z$  917 ( $M^+$ , 55), 105 (100). Anal. Calcd for  $C_{53}H_{60}N_2O_4S_4$ : C, 69.39; H, 3.05; N, 6.59; S, 13.98. Found: C, 69.63; H, 2.91; N, 6.63; S, 13.73.

**Compound 11.** A solution of compound **10** (0.38 g, 0.41 mmol), TsCl (0.16 g, 0.82 mmol),  $Et_3N$  (0.5 mL, 0.35 g, 3.3 mmol), and DMAP (~10 mg, cat) in anhydrous  $CH_2Cl_2$  (150 mL) was stirred at room temperature for 20 h.  $Al_2O_3$  (10 g, Brockmann 1, neutral) was added, whereupon the solvent was removed and the residue was purified by column chromatography (deactivated  $SiO_2$ :  $CH_2Cl_2/Me_2CO$  99:1). The yellow band ( $R_f = 0.15$ ) was collected and the solvent evaporated to give 0.35 g (81%) of the title compound **11** as a yellow foam. Data for **11**:  $^1H$  NMR ( $CD_3COCD_3$ , 300 MHz)  $\delta$  1.18 (t,  $J = 7.5$  Hz, 3H), 1.29 (s, 18H), 2.43 (s, 3H), 2.60 (q,  $J = 7.5$  Hz, 2H), 3.61–3.66 (m, 4H), 3.75–3.79 (m, 4H), 3.98–4.16 (m, 8H), 6.64 (s, 2H), 6.73 (s, 2H), 6.81 (d,  $J = 9.0$  Hz, 2H), 7.09–7.15 (m, 10H), 7.28–7.32 (m, 4H), 7.45 (d,  $J = 8.4$  Hz, 2H), 7.78 (d,  $J = 8.4$  Hz, 2H); MS(FT-MALDI)  $m/z$  1093 ( $M^+ + Na$ , 2), 1070 ( $M^+$ , 100), 921 (15). Anal. Calcd for  $C_{60}H_{66}N_2O_6S_5$ : C, 67.26; H, 6.21; N, 2.61; S, 14.96. Found: C, 65.78; H, 6.24; N, 2.36; S, 14.91.

**Compound 13.** A solution of the tosylate **11** (0.64 g, 0.60 mmol) and **12** (0.26 g, 0.79 mmol) in anhydrous MeCN (50 mL) containing  $K_2CO_3$  (0.34 g, 2.4 mmol), LiBr (10 mg, cat) and 18-crown-6 (~10 mg, cat), was heated under reflux for 2 d. After cooling down to room temperature the reaction mixture was filtered and the residue washed with MeCN ( $2 \times 50$  mL). The combined organic phase filtrate was concentrated in vacuo and the yellow oily residue was purified by column chromatography (deactivated  $SiO_2$ :

CH<sub>2</sub>Cl<sub>2</sub>/EtOH 97:3). The yellow band was collected and the solvent evaporated affording 0.44 g (60%) of the title compound **13** as a yellow foam. Data for **13**: <sup>1</sup>H NMR (CD<sub>3</sub>COCD<sub>3</sub>, 300 MHz)  $\delta$  1.20 (t,  $J = 7.6$  Hz, 3H), 1.29 (s, 18H), 1.49–1.53 (m, 6H), 2.60 (q,  $J = 7.6$  Hz, 2H), 3.37–3.48 (m, 1H), 3.54–3.64 (m, 1H), 3.75–4.00 (m, 14H), 4.08–4.13 (m, 6H), 4.29–4.32 (m, 4H), 4.63 (bs, 1H), 6.76 (s, 2H), 6.77 (s, 2H), 6.84 (d,  $J = 8.9$  Hz, 2H), 6.94–6.97 (m, 2H), 7.09–7.15 (m, 10H), 7.30–7.44 (m, 6H), 7.80 (d,  $J = 8.4$  Hz, 1H), 7.85 (d,  $J = 8.4$  Hz, 1H); MS(FT–MALDI)  $m/z$  1269 ( $M^+ + K$ , 10), 1253 ( $M^+ + Na$ , 10), 1230 ( $M^+$ , 100).

**Compound 14.** A solution of compound **13** (0.40 g, 0.32 mmol) in THF–EtOH (40 mL, 1:1 v/v) was degassed (N<sub>2</sub>, 10 min) before TsOH•H<sub>2</sub>O (~10 mg, cat) was added. The yellow solution was stirred for 16 h at room temperature, whereupon it was diluted with CH<sub>2</sub>Cl<sub>2</sub> (50 mL). The combined organic phase was washed with a saturated aqueous NaHCO<sub>3</sub> solution (50 mL), H<sub>2</sub>O (50 mL) and dried (MgSO<sub>4</sub>). Concentration in vacuo gave a yellow oil, which was subjected to column chromatography (deactivated SiO<sub>2</sub>: CH<sub>2</sub>Cl<sub>2</sub>/EtOAc 1:1). The yellow band ( $R_f = 0.4$ ) was collected and the solvent evaporated to give 0.21 g (56%) of the title compound **14** as a yellow foam. Data for **14**: <sup>1</sup>H NMR (CD<sub>3</sub>COCD<sub>3</sub>, 300 MHz)  $\delta$  1.24 (t,  $J = 7.6$  Hz, 3H), 1.33 (s, 18H), 2.64 (q,  $J = 7.6$  Hz, 2H), 3.50–3.75 (m, 5H), 3.82–3.86 (m, 4H), 3.91–3.94 (m, 2H), 3.97–4.03 (m, 4H), 4.08–4.19 (m, 6H), 4.32–4.36 (m, 4H), 6.80 (s, 2H), 6.81 (s, 2H), 6.89 (d,  $J = 8.9$  Hz, 2H), 6.99–7.01 (m, 2H), 7.13–7.20 (m, 10H), 7.33–7.48 (m, 6H), 7.83–7.89 (m, 2H); MS(FT–MALDI)  $m/z$  1185 ( $M^+ + K$ , 5), 1169 ( $M^+ + Na$ , 20), 1146 ( $M^+$ , 100).

**Compound 15.** A solution of compound **14** (0.20 g, 0.17 mmol), TsCl (0.068 g, 0.35 mmol), Et<sub>3</sub>N (0.2 mL, 0.14 g, 1.4 mmol), and DMAP (~10 mg, cat) in anhydrous CH<sub>2</sub>Cl<sub>2</sub> (50 mL) was stirred at room temperature for 20 h, whereupon the solvent was removed and the yellow solid was purified by column chromatography (deactivated SiO<sub>2</sub>: CH<sub>2</sub>Cl<sub>2</sub>/EtOAc 19:1). The yellow band (*R<sub>f</sub>* = 0.6) was collected and the solvent evaporated to give 0.22 g (98%) of the title compound **15** as a yellow foam. Data for **15**: <sup>1</sup>H NMR (CD<sub>3</sub>COCD<sub>3</sub>, 300 MHz) δ 1.20 (t, *J* = 7.5 Hz, 3H), 1.33 (s, 18H), 2.36 (s, 3H), 2.60 (q, *J* = 7.5 Hz, 2H), 3.77–3.83 (m, 6H), 3.86–3.96 (m, 6H), 4.07–4.15 (m, 6H), 4.20–4.25 (m, 4H), 4.29–4.32 (m, 2H), 6.75 (s, 2H), 6.77 (s, 2H), 6.83 (d, *J* = 9.0 Hz, 2H), 6.94–6.97 (m, 2H), 7.09–7.15 (m, 10H), 7.30–7.35 (m, 7H), 7.39 (t, *J* = 8.5 Hz, 1H), 7.77–7.83 (m, 4H); MS(FT–MALDI) *m/z* 1300 (*M*<sup>+</sup>, 100).

**Compound 16.** The tosylate **15** (0.22 g, 0.17 mmol) was dissolved in anhydrous Me<sub>2</sub>CO (50 mL) and KSCN (0.49 g, 5.04 mmol) was added in one portion. The yellow reaction mixture was heated under reflux for 1 d, whereupon additional KSCN (0.49 g, 5.04 mmol) was added. The reaction mixture was heated under reflux for further 1 d before being cooled to room temperature. After removal of the solvent, the yellow residue was dissolved in CH<sub>2</sub>Cl<sub>2</sub> (100 mL), washed with H<sub>2</sub>O (2 × 50 mL) and dried (MgSO<sub>4</sub>). Concentration in vacuo gave 0.20 g (97%) of the title compound **16** as a yellow foam. Data for **16**: <sup>1</sup>H NMR (CD<sub>3</sub>COCD<sub>3</sub>, 500 MHz) δ 1.20 (t, *J* = 7.6 Hz, 3H), 1.29 (s, 18H), 2.60 (q, *J* = 7.6 Hz, 2H), 3.37 (t, *J* = 5.7 Hz, 2H), 3.78–3.81 (m, 4H), 3.89 (t, *J* = 4.6 Hz, 2H), 3.93–3.95 (m, 2H), 3.99 (t, *J* = 4.6 Hz, 2H), 4.04–4.08 (m, 2H), 4.09–4.13 (m, 6H), 4.29–4.31 (m, 2H), 4.33–4.35 (m, 2H), 6.76 (s, 2H), 6.77 (s, 2H), 6.84 (d, *J* = 8.8 Hz, 2H), 6.95–6.98 (m, 2H), 7.10–7.15 (m, 10H), 7.30–7.32 (m, 4H), 7.37 (t, *J* = 8.5

Hz, 1H), 7.42 (t,  $J = 8.5$  Hz, 1H), 7.81 (d,  $J = 8.5$  Hz, 1H), 7.85 (d,  $J = 8.5$  Hz, 1H); MS(FT-MALDI)  $m/z$  1226 ( $M^+ + K$ , 15), 1210 ( $M^+ + Na$ , 15), 1187 ( $M^+$ , 100); IR (KBr)  $\nu$  2154 (S-C $\equiv$ N)  $\text{cm}^{-1}$ .

**Dumbbell 1.** Compound **16** (0.19 g, 0.16 mmol) and the chloride **17** (0.14 g, 0.18 mmol) were dissolved in anhydrous THF/EtOH (2:1 v/v, 50 mL), after which powdered NaBH<sub>4</sub> (0.060 g, 1.6 mmol) was added in one portion. The reaction mixture was stirred for 1 d at room temperature whereupon additional NaBH<sub>4</sub> (0.060 g, 1.6 mmol) was added and the reaction mixture was stirred for further 3 d at room temperature. Thereafter, it was poured into an ice cooled saturated aqueous NH<sub>4</sub>Cl solution (50 mL) and extracted with CH<sub>2</sub>Cl<sub>2</sub> (2  $\times$  50 mL). The combined organic extracts were dried (MgSO<sub>4</sub>) and concentration in vacuo gave a yellow oil, which was purified by column chromatography (deactivated SiO<sub>2</sub>: CH<sub>2</sub>Cl<sub>2</sub>/EtOAc 3:2). The yellow band ( $R_f = 0.4$ ) was collected and the solvent evaporated affording 0.21 g (68%) of the title compound **1** as a yellow foam Data for **1**: <sup>1</sup>H NMR (CD<sub>3</sub>COCD<sub>3</sub>, 500 MHz)  $\delta$  1.20 (t,  $J = 7.6$  Hz, 3H), 1.29 (s, 18H), 2.60 (m, 4H), 3.29 (s, 9H), 3.48–3.50 (m, 6H), 3.62–3.64 (m, 6H), 3.75–3.82 (m, 14H), 3.84–3.86 (m, 2H), 3.92–3.94 (m, 4H), 4.07–4.12 (m, 12H), 4.24–4.27 (m, 2H), 4.30–4.32 (m, 2H), 4.87 (s, 2H), 4.96 (s, 4H), 6.74 (s, 2H), 6.74 (s, 2H), 6.75 (s, 2H), 6.80–6.98 (m, 10H), 7.10–7.15 (m, 10H), 7.28–7.41 (m, 12H), 7.79 (d,  $J = 8.6$  Hz, 1H), 7.83 (d,  $J = 8.6$  Hz, 1H); MS(MALDI-TOF)  $m/z$  1925 ( $M^+$ , 100). Anal. Calcd for C<sub>110</sub>H<sub>128</sub>N<sub>2</sub>O<sub>18</sub>S<sub>5</sub>: C, 68.58; H, 6.70; N, 1.45. Found: C, 68.41; H, 6.75; N, 1.29.

**[2]Rotaxane RBPTTF•4PF<sub>6</sub>.** A solution of the dumbbell **1** (0.20 g, 0.10 mmol), **2•2PF<sub>6</sub>** (0.22 g, 0.31 mmol), and the dibromide **3** (0.082 g, 0.31 mmol) in anhydrous

DMF (8 mL) was transferred to a teflon-tube and subjected to 10 kbar of pressure at room temperature for 3 d. The greenish brown solution was directly subjected to column chromatography (deactivated SiO<sub>2</sub>) and unreacted dumbbell was eluted with Me<sub>2</sub>CO, whereupon the eluent was changed to Me<sub>2</sub>CO/NH<sub>4</sub>PF<sub>6</sub> (1.0 g NH<sub>4</sub>PF<sub>6</sub> in 100 mL Me<sub>2</sub>CO) and the greenish brown band was collected. Most of the solvent was removed in vacuo ( $T < 30$  °C), followed by addition of H<sub>2</sub>O (100 mL). The resulting precipitate was collected by filtration, washed with H<sub>2</sub>O (2 × 20 mL) and Et<sub>2</sub>O (2 × 30 mL) and dried in vacuo over P<sub>2</sub>O<sub>5</sub>, affording 0.15 g (47%) of the title compound **RBPTTF**•4PF<sub>6</sub> as a brown solid. Data for **RBPTTF**•4PF<sub>6</sub>: The data given below are for the 1:1 mixture of the two translational isomers; <sup>19</sup>F NMR (CD<sub>3</sub>COCD<sub>3</sub>, 376 MHz)  $\delta$  -72.4 (d); <sup>31</sup>P NMR (CD<sub>3</sub>COCD<sub>3</sub>, 161 MHz)  $\delta$  -144.2 (septet); MS(ES)  $m/z$  1369 ([M - 2PF<sub>6</sub>]<sup>2+</sup>, 15), 864 ([M - 3PF<sub>6</sub>]<sup>3+</sup>, 80), 612 ([M - 4PF<sub>6</sub>]<sup>4+</sup>, 100). Anal. Calcd for C<sub>146</sub>H<sub>160</sub>F<sub>24</sub>N<sub>6</sub>O<sub>18</sub>P<sub>4</sub>S<sub>5</sub>•2H<sub>2</sub>O: C, 57.25; H, 5.40; N, 2.74; S, 5.23. Found: C, 57.05; H, 5.20; N, 2.82; S, 5.04.

**2-Cyanoethylthio-5-ethylthio-1,3-dithiole-2-thione (20)**. A solution of compound **19** (6.09 g, 20.0 mmol) in anhydrous MeCN (150 mL) was degassed (N<sub>2</sub>, 5 min) before a solution of NaOMe (7.6 mL of a 2.75 M solution in MeOH, 20.9 mmol) was added dropwise to the yellow solution via a syringe over a period of 45 min at room temperature. The red mixture was stirred for 15 min, whereupon EtI (3.9 mL, 7.70 g, 49.5 mmol) was added in one portion and the reaction mixture was stirred for 24 h at room temperature. The solvent was evaporated and the resulting red oil was dissolved in CH<sub>2</sub>Cl<sub>2</sub> (250 mL), washed with H<sub>2</sub>O (3 × 200 mL) and dried (MgSO<sub>4</sub>). Removal of the solvent gave a red oil, which was purified by column chromatography (SiO<sub>2</sub>:

CH<sub>2</sub>Cl<sub>2</sub>/cyclohexane 4:1). The second yellow band ( $R_f = 0.35$ ) was collected and concentrated, affording a yellow oil, which was repeatedly dissolved in CH<sub>2</sub>Cl<sub>2</sub> (2 × 50 mL) and concentrated to give 5.14 g (92%) of the title compound **20** as a red oil which solidified upon standing to give a yellow solid. Data for **20**: mp 49.5–50.5 °C; <sup>1</sup>H NMR (CDCl<sub>3</sub>, 300 MHz)  $\delta$  1.36 (t,  $J = 7.4$  Hz, 3H), 2.74 (t,  $J = 7.1$  Hz, 2H), 2.95 (q,  $J = 7.4$  Hz, 2H), 3.08 (t,  $J = 7.1$  Hz, 2H); <sup>13</sup>C NMR CDCl<sub>3</sub>, 75 MHz)  $\delta$  14.8, 18.7, 30.8, 31.8, 117.1, 129.3, 142.4, 210.2; MS(EI)  $m/z$  279 (M<sup>+</sup>, 100), 88 (84); IR (KBr)  $\nu$  2247 cm<sup>-1</sup> (C≡N). Anal. Calcd for C<sub>8</sub>H<sub>9</sub>NS<sub>5</sub>: C, 34.38; H, 3.25; N, 5.01; S, 57.36. Found: C, 34.60; H, 3.22; N, 5.07; S, 57.48.

**2-{4-(2-Cyanoethylthio)-5-ethylthio-1,3-dithiole-2-yliden}-5-tosyl-(1,3)-dithiolo[4,5-*c*]-pyrrole (22).** Ketone **21** (1.87 g, 6.01 mmol) and thione **20** (1.68 g, 6.01 mmol) were suspended in distilled (EtO)<sub>3</sub>P (50 mL) and heated to 135 °C (during heating the two solids dissolved leaving a red solution and after 10–15 min a yellow orange precipitate was formed). Two additional portions of **20** (each containing 0.84 g, 3.01 mmol) were added after 15 and 30 min, respectively. The red reaction mixture was stirred for another 3 h at 135 °C, cooled to room temperature and addition of MeOH (150 mL) yielded a yellow solid, which was filtered and washed with MeOH (3 × 50 mL). The yellow solid was subjected to column chromatography (SiO<sub>2</sub>: CH<sub>2</sub>Cl<sub>2</sub>) and the yellow band ( $R_f = 0.4$ ) was collected and the solvent evaporated to give a yellow solid, which was dissolved in CH<sub>2</sub>Cl<sub>2</sub>/MeOH (1:1 v/v, 500 mL) and concentrated to approximately half of its volume to precipitate the product. The yellow crystals were collected by filtration, washed with MeOH (50 mL) and dried in vacuo to give 2.40 g, (74%) of the title compound **22** as yellow needles. Data for **22**: mp 200–201 °C; <sup>1</sup>H NMR

(CD<sub>3</sub>SOCD<sub>3</sub>, 300 MHz)  $\delta$  1.25 (t,  $J$  = 7.3 Hz, 3H), 2.38 (s, 3H), 2.84 (t,  $J$  = 6.6 Hz, 2H), 2.89 (q,  $J$  = 7.3 Hz, 2H), 3.11 (t,  $J$  = 6.6 Hz, 2H), 7.39 (s, 2H), 7.46 (d,  $J$  = 8.3 Hz, 2H), 7.82 (d,  $J$  = 8.3 Hz, 2H); <sup>13</sup>C NMR (CD<sub>3</sub>SOCD<sub>3</sub>, 75 MHz)  $\delta$  15.0, 18.1, 21.1, 29.9, 30.9, 112.3, 112.8 (2 signals), 117.8, 118.9, 124.0, 125.9, 126.0, 126.8, 129.8, 130.4, 134.4, 145.9; MS(EI)  $m/z$  542 (M<sup>+</sup>, 11), 387 ([M – Ts]<sup>+</sup>, 28), 184 (55), 105 (100), 91 (65); IR (KBr)  $\nu$  2250 cm<sup>-1</sup> (C $\equiv$ N). Anal. Calcd for C<sub>20</sub>H<sub>18</sub>N<sub>2</sub>O<sub>2</sub>S<sub>7</sub>: C, 44.25; H, 3.34; N, 5.16; S, 41.35. Found: C, 44.40; H, 3.34; N, 5.23; S, 41.42.

**Compound 23:** A solution of the iodide **18** (0.95 g, 1.05 mmol) and **22** (0.55 g, 1.01 mmol) in anhydrous THF (70 mL) was degassed (N<sub>2</sub>, 10 min) before a solution of CsOH•H<sub>2</sub>O (0.174 g, 1.04 mmol) in anhydrous MeOH (5.0 mL) was added dropwise via a syringe over a period of 75 min at room temperature. Subsequently, the reaction mixture was stirred for 2 d at room temperature, whereupon the yellow reaction mixture was diluted with CH<sub>2</sub>Cl<sub>2</sub> (150 mL), washed with brine (150 mL), H<sub>2</sub>O (2 × 150 mL) and dried (MgSO<sub>4</sub>). Removal of the solvent gave a yellow foam, which was purified by column chromatography (SiO<sub>2</sub>: CH<sub>2</sub>Cl<sub>2</sub>/cyclohexane 9:1). The broad yellow band ( $R_f$  = 0.35) was collected and concentrated, affording a yellow foam, which was repeatedly dissolved in CH<sub>2</sub>Cl<sub>2</sub> (2 × 30 mL) and concentrated to give 0.99 g (77%) of the title compound **23** as a yellow foam. Data for **23**: <sup>1</sup>H NMR (CD<sub>3</sub>COCD<sub>3</sub>, 300 MHz)  $\delta$  1.20 (t,  $J$  = 7.6 Hz, 3H), 1.23 (t,  $J$  = 7.4 Hz, 3H), 1.29 (s, 18H), 2.38 (s, 3H), 2.61 (q,  $J$  = 7.6 Hz, 2H), 2.84 (q,  $J$  = 7.4 Hz, 2H), 3.10 (t,  $J$  = 6.3 Hz, 2H), 3.84 (t,  $J$  = 6.3 Hz, 2H), 3.93–3.99 (m, 4H), 4.02–4.06 (m, 2H), 4.14–4.19 (m, 2H), 4.27–4.33 (m, 4H), 6.84 (d,  $J$  = 9.0 Hz, 2H), 6.89–6.97 (m, 2H), 7.06–7.14 (m, 10H), 7.24 and 7.27 (AB q,  $J$  = 2.1 Hz, 2H), 7.28–7.43 (m, 8H), 7.80–7.85 (m, 4H); MS(MALDI–TOF)  $m/z$  1265

( $M^+$ , 22), 1111 ( $[M + H - Ts]^+$ , 100); HiRes-FT-MALDI-MS  $m/z$  1265.3580 (calcd for  $C_{70}H_{75}NO_7S_7^+$  1265.3583). Anal. Calcd for  $C_{70}H_{75}NO_7S_7$ : C, 66.37; H, 5.97; N, 1.11; S, 17.72. Found: C, 65.88; H, 5.94; N, 1.30; S, 17.75.

**Compound 24:** Compound **23** (0.85 g, 0.67 mmol) was dissolved in anhydrous THF/MeOH (1:1 v/v, 70 mL) and degassed ( $N_2$ , 10 min) before NaOMe (25% solution in MeOH, 2.3 mL, 0.54 g, 10.1 mmol) was added in one portion. The yellow solution was heated under reflux for 15 min before being cooled to room temperature, whereupon the solvent was evaporated. The yellow residue was dissolved in  $CH_2Cl_2$  (100 mL), washed with  $H_2O$  ( $3 \times 100$  mL) and dried ( $MgSO_4$ ). Concentration gave a yellow foam, which was subjected to column chromatography ( $SiO_2$ :  $CH_2Cl_2$ ). The yellow band ( $R_f = 0.5$ ) was collected and concentrated to provide 0.64 g (87%) of the title compound **24** as a yellow foam. Data for **24**:  $^1H$  NMR ( $CD_3COCD_3$ , 300 MHz)  $\delta$  1.21 (t,  $J = 7.6$  Hz, 3H), 1.26 (t,  $J = 7.3$  Hz, 3H), 1.30 (s, 18H), 2.61 (q,  $J = 7.6$  Hz, 2H), 2.87 (q,  $J = 7.3$  Hz, 2H), 3.11 (t,  $J = 6.4$  Hz, 2H), 3.86 (t,  $J = 6.4$  Hz, 2H), 3.95–4.01 (m, 4H), 4.02–4.05 (m, 2H), 4.16–4.19 (m, 2H), 4.29–4.33 (m, 4H), 6.79 and 6.80 (AB q,  $J = 1.9$  Hz, 2H), 6.85 (d,  $J = 9.0$  Hz, 2H), 6.93 (d,  $J = 8.0$  Hz, 1H), 6.96 (d,  $J = 8.0$  Hz, 1H), 7.06–7.14 (m, 10H), 7.26–7.38 (m, 6H), 7.83 (d,  $J = 8.0$  Hz, 1H), 7.86 (d,  $J = 8.0$  Hz, 1H), 10.36 (bs, 1H); MS(MALDI-TOF)  $m/z$  1112 ( $M^+$ , 100); HiRes-FT-MALDI-MS  $m/z$  1111.3452 (calcd for  $C_{63}H_{69}NO_5S_6^+$  1111.3495). Anal. Calcd for  $C_{63}H_{69}NO_5S_6$ : C, 68.01; H, 6.25; N, 1.26; S, 17.29. Found: C, 67.74; H, 6.36; N, 1.28; S, 17.06.

**Compound 26:** Compound **24** (0.61 g, 0.55 mmol) and compound **25** (0.25 g, 0.90 mmol) were dissolved in anhydrous DMF (20 mL) and degassed ( $N_2$ , 10 min) before

NaH (0.055 g of a 60% suspension in mineral oil, 1.38 mmol) was added. The reaction mixture was stirred for 3.5 h at room temperature, causing the initially yellow solution to become more orange. Brine (80 mL) was added dropwise until no more gas evolution was observed and the resulting yellow precipitate was filtered, washed with H<sub>2</sub>O (20 mL) and dried. The crude product was purified by column chromatography (SiO<sub>2</sub>: CH<sub>2</sub>Cl<sub>2</sub>). The yellow band ( $R_f = 0.5$ ) was collected and the solvent evaporated, providing 0.50 g (75%) of the title compound **26** as a yellow foam. Data for **26**: <sup>1</sup>H NMR (CD<sub>3</sub>COCD<sub>3</sub>, 300 MHz)  $\delta$  1.21 (t,  $J = 7.6$  Hz, 3H), 1.26 (t,  $J = 7.3$  Hz, 3H), 1.30 (s, 18H), 2.61 (q,  $J = 7.6$  Hz, 2H), 2.86 (q,  $J = 7.3$  Hz, 2H), 3.11 (t,  $J = 6.4$  Hz, 2H), 3.61–3.73 (m, 4H), 3.74–3.78 (m, 2H), 3.85 (t,  $J = 6.4$  Hz, 2H), 3.94–4.00 (m, 4H), 4.02–4.05 (m, 2H), 4.08–4.12 (m, 2H), 4.15–4.19 (m, 2H), 4.28–4.34 (m, 4H), 6.76 and 6.79 (AB q,  $J = 2.0$  Hz, 2H), 6.85 (d,  $J = 9.0$  Hz, 2H), 6.93 (d,  $J = 8.0$  Hz, 1H), 6.96 (d,  $J = 8.0$  Hz, 1H), 7.06–7.13 (m, 10H), 7.26–7.38 (m, 6H), 7.83 (d,  $J = 8.0$  Hz, 1H), 7.86 (d,  $J = 8.0$  Hz, 1H); MS(MALDI-TOF)  $m/z$  1217 ( $M^+$ , 100); HiRes-FT-MALDI-MS  $m/z$  1217.3675 (calcd for C<sub>67</sub>H<sub>76</sub>ClNO<sub>6</sub>S<sub>6</sub><sup>+</sup> 1217.3680). Anal. Calcd for C<sub>67</sub>H<sub>76</sub>ClNO<sub>6</sub>S<sub>6</sub>: C, 66.01; H, 6.28; N, 1.15; S, 15.78. Found: C, 66.14; H, 6.30; N, 1.20; S, 15.61.

**Compound 27**: The chloride **26** (0.46 g, 0.38 mmol) was dissolved in anhydrous Me<sub>2</sub>CO (60 mL) and NaI (3.42 g, 22.8 mmol) was added in one portion. The reaction mixture was heated under reflux for 6 d, before being cooled to room temperature and the solvent removed in vacuo. The yellow residue was dissolved in CH<sub>2</sub>Cl<sub>2</sub> (75 mL) and washed with H<sub>2</sub>O (3 × 50 mL), before being dried (MgSO<sub>4</sub>). Concentration in vacuo gave 0.49 g (99%) of the title compound **27** as a yellow foam. Data for **27**: <sup>1</sup>H NMR (CD<sub>3</sub>COCD<sub>3</sub>, 300 MHz)  $\delta$  1.21 (t,  $J = 7.6$  Hz, 3H), 1.26 (t,  $J = 7.3$  Hz, 3H), 1.30

(s, 18H), 2.61 (q,  $J = 7.6$  Hz, 2H), 2.86 (q,  $J = 7.3$  Hz, 2H), 3.11 (t,  $J = 6.4$  Hz, 2H), 3.30 (t,  $J = 6.5$  Hz, 2H), 3.69 (t,  $J = 6.5$  Hz, 2H), 3.74–3.78 (m, 2H), 3.85 (t,  $J = 6.4$  Hz, 2H), 3.95–4.01 (m, 4H), 4.02–4.06 (m, 2H), 4.08–4.12 (m, 2H), 4.16–4.19 (m, 2H), 4.29–4.34 (m, 4H), 6.77 and 6.80 (AB q,  $J = 2.1$  Hz, 2H), 6.85 (d,  $J = 9.0$  Hz, 2H), 6.93 (d,  $J = 8.0$  Hz, 1H), 6.96 (d,  $J = 8.0$  Hz, 1H), 7.06–7.14 (m, 10H), 7.26–7.38 (m, 6H), 7.83 (d,  $J = 8.0$  Hz, 1H), 7.86 (d,  $J = 8.0$  Hz, 1H); MS(MALDI-TOF)  $m/z$  1309 ( $M^+$ , 100); HiRes-FT-MALDI-MS  $m/z$  1309.3035 (calcd for  $C_{67}H_{76}INO_6S_6^+$  1309.3036). Anal. Calcd for  $C_{67}H_{76}INO_6S_6$ : C, 61.40; H, 5.84; N, 1.07; S, 14.68. Found: C, 61.78; H, 5.83; N, 1.11; S, 14.50.

**Compound 28:** The iodide **27** (0.48 g, 0.37 mmol) was dissolved in anhydrous  $Me_2CO$  (50 mL) and KSCN (1.78 g, 18.3 mmol) was added in one portion. The yellow reaction mixture was heated under reflux for 3 d, whereupon the reaction mixture was cooled to room temperature. After removal of the solvent, the yellow residue was dissolved in  $CH_2Cl_2$  (100 mL), washed with  $H_2O$  ( $3 \times 75$  mL) and dried ( $MgSO_4$ ). Concentration in vacuo gave 0.45 g (99%) of the title compound **28** as a yellow foam. Data for **28**:  $^1H$  NMR ( $CD_3COCD_3$ , 300 MHz)  $\delta$  1.21 (t,  $J = 7.6$  Hz, 3H), 1.26 (t,  $J = 7.3$  Hz, 3H), 1.30 (s, 18H), 2.61 (q,  $J = 7.6$  Hz, 2H), 2.87 (q,  $J = 7.3$  Hz, 2H), 3.11 (t,  $J = 6.4$  Hz, 2H), 3.28 (t,  $J = 5.7$  Hz, 2H), 3.76–3.81 (m, 4H), 3.86 (t,  $J = 6.4$  Hz, 2H), 3.94–4.01 (m, 4H), 4.03–4.06 (m, 2H), 4.11–4.14 (m, 2H), 4.16–4.19 (m, 2H), 4.29–4.34 (m, 4H), 6.77 and 6.80 (AB q,  $J = 2.1$  Hz, 2H), 6.85 (d,  $J = 9.0$  Hz, 2H), 6.93 (d,  $J = 8.0$  Hz, 1H), 6.96 (d,  $J = 8.0$  Hz, 1H), 7.06–7.14 (m, 10H), 7.26–7.38 (m, 6H), 7.83 (d,  $J = 8.0$  Hz, 1H), 7.86 (d,  $J = 8.0$  Hz, 1H); MS(MALDI-TOF)  $m/z$  1241 ( $M^+$ , 100); HiRes-FT-MALDI-MS  $m/z$  1240.3743 (calcd for  $C_{68}H_{76}N_2O_6S_7^+$  1240.3743); IR (KBr)  $\nu$  2154  $cm^{-1}$

(S-C≡N). Anal. Calcd for C<sub>68</sub>H<sub>76</sub>N<sub>2</sub>O<sub>6</sub>S<sub>7</sub>: C, 65.77; H, 6.17; N, 2.26; S, 18.08. Found: C, 65.87; H, 6.31; N, 2.28; S, 17.83.

**Dumbbell 29:** The chloride **17** (0.19 g, 0.24 mmol) and compound **28** (0.25 g, 0.20 mmol) were dissolved in anhydrous THF/EtOH (2:1 v/v, 50 mL), after which powdered NaBH<sub>4</sub> (0.15 g, 3.97 mmol) was added in one portion. The reaction mixture was stirred for 2 d at room temperature, whereupon it was poured into a saturated aqueous NH<sub>4</sub>Cl solution (50 mL), and extracted with CH<sub>2</sub>Cl<sub>2</sub> (2 × 75 mL). The combined organic extracts were washed with brine (100 mL) and dried (MgSO<sub>4</sub>). Concentration in vacuo gave a yellow oil, which was purified by column chromatography (SiO<sub>2</sub>: CH<sub>2</sub>Cl<sub>2</sub>/EtOAc 2:1). The yellow band (*R<sub>f</sub>* = 0.5) was collected and the solvent evaporated affording a yellow oil, which was repeatedly dissolved in CH<sub>2</sub>Cl<sub>2</sub> (2 × 25 mL) and concentrated to give 0.31 g (78%) of the title compound **29** as a yellow foam. Data for **29**: <sup>1</sup>H NMR (CD<sub>3</sub>COCD<sub>3</sub>, 300 MHz) δ 1.21 (t, *J* = 7.6 Hz, 3H), 1.24 (t, *J* = 7.3 Hz, 3H), 1.30 (s, 18H), 2.52 (t, *J* = 6.4 Hz, 2H), 2.61 (q, *J* = 7.6 Hz, 2H), 2.84 (q, *J* = 7.3 Hz, 2H), 3.08 (t, *J* = 6.4 Hz, 2H), 3.29 (s, 9H), 3.49 (t, *J* = 6.4 Hz, 2H), 3.48–3.51 (m, 6H), 3.62–3.67 (m, 10H), 3.77–3.82 (m, 6H), 3.83 (t, *J* = 6.4 Hz, 2H), 3.93–3.98 (m, 4H), 4.01–4.18 (m, 12H), 4.26–4.32 (m, 4H), 4.91 (s, 2H), 5.03 (s, 4H), 6.73 (s, 2H), 6.76 and 6.78 (AB q, *J* = 2.0 Hz, 2H), 6.82 (d, *J* = 8.5 Hz, 2H), 6.85 (d, *J* = 9.1 Hz, 2H), 6.92 (d, *J* = 8.0 Hz, 1H), 6.94 (d, *J* = 8.0 Hz, 1H), 6.95 (d, *J* = 8.6 Hz, 4H), 7.07–7.14 (m, 10H), 7.26–7.35 (m, 8H), 7.39 (d, *J* = 8.6 Hz, 4H), 7.83 (d, *J* = 8.0 Hz, 1H), 7.86 (d, *J* = 8.0 Hz, 1H); MS(MALDI-TOF) *m/z* 1976 (M<sup>+</sup>, 100), 1767 (12); HiRes-FT-MALDI-MS *m/z* 1977.7405 (calcd for C<sub>110</sub>H<sub>131</sub>NO<sub>18</sub>S<sub>7</sub><sup>+</sup> 1977.7406). Anal. Calcd for C<sub>110</sub>H<sub>131</sub>NO<sub>18</sub>S<sub>7</sub>: C, 66.74; H, 6.67; N, 0.71; S, 11.34. Found: C, 66.64; H, 6.45; N, 0.77; S, 11.15.

**[2]Rotaxane RBLOCK•4PF<sub>6</sub>**: A solution of the dumbbell **29** (0.25 g, 0.13 mmol), **2•2PF<sub>6</sub>** (0.27 g, 0.38 mmol), and the dibromide **3** (0.10 g, 0.38 mmol) in anhydrous DMF (12 mL) was transferred to a teflon-tube and subjected to 10 kbar of pressure at room temperature for 3 d. The red solution was directly subjected to column chromatography (SiO<sub>2</sub>) and unreacted dumbbell was eluted with Me<sub>2</sub>CO, whereupon the eluent was changed to Me<sub>2</sub>CO/NH<sub>4</sub>PF<sub>6</sub> (1.0 g NH<sub>4</sub>PF<sub>6</sub> in 100 mL Me<sub>2</sub>CO) and the red band was collected. Most of the solvent was removed in vacuo ( $T < 30$  °C), followed by addition of H<sub>2</sub>O (100 mL). The resulting precipitate was collected by filtration, washed with H<sub>2</sub>O (2 × 20 mL) and Et<sub>2</sub>O (2 × 30 mL) and dried in vacuo over P<sub>2</sub>O<sub>5</sub>, affording 0.16 g (41%) of the title compound **RBLOCK•4PF<sub>6</sub>** as a red solid. Data for **RBLOCK•4PF<sub>6</sub>**: mp 170 °C (decomposed without melting); <sup>1</sup>H NMR (400 MHz, CD<sub>3</sub>COCD<sub>3</sub>)  $\delta$  1.18 (t,  $J = 7.6$  Hz, 3H), 1.27 (s, 18H), 1.30 (t,  $J = 7.3$  Hz, 3H), 2.56 (t,  $J = 6.2$  Hz, 2H), 2.58 (q,  $J = 7.6$  Hz, 2H), 2.72 (d,  $J = 8.0$  Hz, 1H), 2.74 (d,  $J = 8.0$  Hz, 1H), 2.93 (q,  $J = 7.3$  Hz, 2H), 3.29 (s, 9H), 3.41–3.46 (m, 2H), 3.48–3.52 (m, 6H), 3.55 (t,  $J = 6.5$  Hz, 2H), 3.63–3.69 (m, 8H), 3.71 (s, 2H), 3.74–3.82 (m, 6H), 4.02–4.22 (m, 10H), 4.34–4.45 (m, 6H), 4.48–4.62 (m, 6H), 4.90 (s, 2H), 5.04 (s, 4H), 6.01–6.14 (bm, 8H), 6.15 (t,  $J = 8.0$  Hz, 1H), 6.24 (t,  $J = 8.0$  Hz, 1H), 6.44 (d,  $J = 8.0$  Hz, 1H), 6.45 (d,  $J = 8.0$  Hz, 1H), 6.66 and 6.72 (AB q,  $J = 2.2$  Hz, 2H), 6.78 (s, 2H), 6.80–6.96 (m, 8H), 7.03–7.10 (m, 10H), 7.26–7.34 (m, 6H), 7.40 (d,  $J = 8.4$  Hz, 4H), 7.50–7.90 (bm, 8H), 8.10–8.50 (bm, 8H), 9.05–9.45 (bm, 8H); MS (MALDI–TOF):  $m/z$  2644 ( $[M - 3PF_6]^+$ , 8) 2499 ( $[M - 4PF_6]^+$ , 8) 1977 (2), 665 ( $[CBPQT•PF_6]^+$ , 16), 561 (100); UV/Vis (MeCN, 298 K)  $\lambda_{max}$  540 nm ( $\epsilon$  920 L mol<sup>-1</sup> cm<sup>-1</sup>). Anal. Calcd for C<sub>146</sub>H<sub>163</sub>F<sub>24</sub>N<sub>5</sub>O<sub>18</sub>P<sub>4</sub>S<sub>7</sub>•2H<sub>2</sub>O: C, 56.27; H, 5.40; N, 2.25; S, 7.20. Found: C, 56.23; H, 5.32; N, 2.46; S, 7.50.

**A-4. Reference**

---

- (Si) Jeppesen, J. O.; Takimiya, K.; Jensen, F.; Brimert, T.; Nielsen, K.; Thorup, N.; Becher J. *J. Org. Chem.* **2000**, *65*, 5794–5805.
- (Sii) Hansen, J. G.; Bang, K. S.; Thorup, N.; Becher, J. *Eur. J. Org. Chem.* **2000**, 2135–2144.
- (Siii) Collier, C. P.; Jeppesen, J. O.; Luo, Y.; Perkins, J.; Wong, E. W.; Heath, J. R.; Stoddart, J. F. *J. Am. Chem. Soc.* **2001**, *123*, 12632–12641.
- (Siv) Yamamoto, T.; Tseng, H.-R.; Stoddart, J. F.; Balzani, V.; Credi, A.; Marchioni, F.; Venturi, M. *Collect. Czech. Chem. C.* **2003**, *68*, 1488–1514.
- (Sv) Anelli, P.-L.; Ashton, P. R.; Ballardini, R.; Balzani, V.; Gandolfi, M. T.; Goodnow, T. T.; Kaifer, A. E.; Philp, D.; Pietraszkiewicz, M.; Prodi, L.; Reddington, M. V.; Slawin, A. M. Z.; Spencer, N.; Vicent, C.; Williams, D. J. *J. Am. Chem. Soc.* **1992**, *114*, 193–218.
- (Svi) Svenstrup, N.; Rasmussen, K. M.; Hansen, T. K.; Becher J. *Synthesis* **1994**, 809–812.
- (Svii) Jeppesen, J. O.; Nygaard, S.; Vignon, S. A.; Stoddart, J. F. *Eur. J. Org. Chem.* **2005**, 196–220.
- (Sviii) Butler, C. L.; Renfrew, A. G.; Cretcher, L. H.; Souther, B. L. *J. Am. Chem. Soc.* **1937**, *59*, 227–229.
- (Six) D. D. Perrin, W. L. F. Armarego, *Purification of Laboratory Chemicals*, Pergamon Press, New York, **1988**.

## Appendix B

### LabWindow Code for Memory Measurement

```

#include <gpib.h>
// #include <windows.h>
#include <utility.h>
#include "decl-32.h"
#include <stdio.h>
#include <string.h>
#include <userint.h>
#include <dataacq.h>
#include <ansi_c.h>
#include "MUX_AC.h"

static int daq, daq1;
FILE *fp_out;
int Device1;
int cross_point[9][9], set_bit[9][9];
int num_read, all_switch, all_control=-1, ramp, ramp_num=20;
double time_write, time_read, volt_write_on, volt_write_off, volt_read, volt_hold, threshold_high, threshold_low;
double adch0, adch1, volt_ramp0, volt_ramp1, ramp_rate;
const char tmp_file[10]="tmp.dat";

void main()
{
    int i;
    Device1=ibdev(0,18,0,10,1,0);           /* initiate 707A */
    ibwrt(Device1,"REMOTE",6);           /* enable remote mode */
    ibwrt(Device1,"EOX",3);              /* Point to present relays */

    daq = LoadPanel (0, "MUX_AC.uir", MUX);
    DisplayPanel (daq);
    i=AI_Clear (1);
    RunUserInterface ();
}

int select_ind (int panel, int control, int event,
               void *callbackData, int eventData1, int eventData2)
{
    {
        daq1 = LoadPanel (1, "MUX_AC.uir", MUX1);
        DisplayPanel (daq1);
        return 1;
    }
}

int close_selection(int panel, int control, int event,
                  void *callbackData, int eventData1, int eventData2)
{
    {
        int i,m;
        i=HidePanel(daq1);
        return 0;
    }
}

int switch_control(int panel, int control, int event,
                  void *callbackData, int eventData1, int eventData2)
{
    {
        int m;
        if(all_control==-1){
            m=SetCtrlAttribute(daq,MUX_ALL_SWITCHES, ATTR_DIMMED, 0);
        }
        else{
            m=SetCtrlAttribute(daq,MUX_ALL_SWITCHES, ATTR_DIMMED, 1);
        }
        all_control=all_control*(-1);
        return 1;
    }
}

int configure_ind (int panel, int control, int event,
                  void *callbackData, int eventData1, int eventData2)
{
    {

```

```

int i,j,k,m,i_ramp;
char c[5],d[6];
if (all_control!=1){
m = GetCtrlVal (daq, MUX_Switch1_1, &cross_point[1][1]);
m = GetCtrlVal (daq, MUX_Switch1_2, &cross_point[1][2]);
m = GetCtrlVal (daq, MUX_Switch1_3, &cross_point[1][3]);
m = GetCtrlVal (daq, MUX_Switch1_4, &cross_point[1][4]);
m = GetCtrlVal (daq, MUX_Switch1_5, &cross_point[1][5]);
m = GetCtrlVal (daq, MUX_Switch1_6, &cross_point[1][6]);
m = GetCtrlVal (daq, MUX_Switch1_7, &cross_point[1][7]);
m = GetCtrlVal (daq, MUX_Switch1_8, &cross_point[1][8]);
m = GetCtrlVal (daq, MUX_Switch2_1, &cross_point[2][1]);
m = GetCtrlVal (daq, MUX_Switch2_2, &cross_point[2][2]);
m = GetCtrlVal (daq, MUX_Switch2_3, &cross_point[2][3]);
m = GetCtrlVal (daq, MUX_Switch2_4, &cross_point[2][4]);
m = GetCtrlVal (daq, MUX_Switch2_5, &cross_point[2][5]);
m = GetCtrlVal (daq, MUX_Switch2_6, &cross_point[2][6]);
m = GetCtrlVal (daq, MUX_Switch2_7, &cross_point[2][7]);
m = GetCtrlVal (daq, MUX_Switch2_8, &cross_point[2][8]);
m = GetCtrlVal (daq, MUX_Switch3_1, &cross_point[3][1]);
m = GetCtrlVal (daq, MUX_Switch3_2, &cross_point[3][2]);
m = GetCtrlVal (daq, MUX_Switch3_3, &cross_point[3][3]);
m = GetCtrlVal (daq, MUX_Switch3_4, &cross_point[3][4]);
m = GetCtrlVal (daq, MUX_Switch3_5, &cross_point[3][5]);
m = GetCtrlVal (daq, MUX_Switch3_6, &cross_point[3][6]);
m = GetCtrlVal (daq, MUX_Switch3_7, &cross_point[3][7]);
m = GetCtrlVal (daq, MUX_Switch3_8, &cross_point[3][8]);
m = GetCtrlVal (daq, MUX_Switch4_1, &cross_point[4][1]);
m = GetCtrlVal (daq, MUX_Switch4_2, &cross_point[4][2]);
m = GetCtrlVal (daq, MUX_Switch4_3, &cross_point[4][3]);
m = GetCtrlVal (daq, MUX_Switch4_4, &cross_point[4][4]);
m = GetCtrlVal (daq, MUX_Switch4_5, &cross_point[4][5]);
m = GetCtrlVal (daq, MUX_Switch4_6, &cross_point[4][6]);
m = GetCtrlVal (daq, MUX_Switch4_7, &cross_point[4][7]);
m = GetCtrlVal (daq, MUX_Switch4_8, &cross_point[4][8]);
m = GetCtrlVal (daq, MUX_Switch5_1, &cross_point[5][1]);
m = GetCtrlVal (daq, MUX_Switch5_2, &cross_point[5][2]);
m = GetCtrlVal (daq, MUX_Switch5_3, &cross_point[5][3]);
m = GetCtrlVal (daq, MUX_Switch5_4, &cross_point[5][4]);
m = GetCtrlVal (daq, MUX_Switch5_5, &cross_point[5][5]);
m = GetCtrlVal (daq, MUX_Switch5_6, &cross_point[5][6]);
m = GetCtrlVal (daq, MUX_Switch5_7, &cross_point[5][7]);
m = GetCtrlVal (daq, MUX_Switch5_8, &cross_point[5][8]);
m = GetCtrlVal (daq, MUX_Switch6_1, &cross_point[6][1]);
m = GetCtrlVal (daq, MUX_Switch6_2, &cross_point[6][2]);
m = GetCtrlVal (daq, MUX_Switch6_3, &cross_point[6][3]);
m = GetCtrlVal (daq, MUX_Switch6_4, &cross_point[6][4]);
m = GetCtrlVal (daq, MUX_Switch6_5, &cross_point[6][5]);
m = GetCtrlVal (daq, MUX_Switch6_6, &cross_point[6][6]);
m = GetCtrlVal (daq, MUX_Switch6_7, &cross_point[6][7]);
m = GetCtrlVal (daq, MUX_Switch6_8, &cross_point[6][8]);
m = GetCtrlVal (daq, MUX_Switch7_1, &cross_point[7][1]);
m = GetCtrlVal (daq, MUX_Switch7_2, &cross_point[7][2]);
m = GetCtrlVal (daq, MUX_Switch7_3, &cross_point[7][3]);
m = GetCtrlVal (daq, MUX_Switch7_4, &cross_point[7][4]);
m = GetCtrlVal (daq, MUX_Switch7_5, &cross_point[7][5]);
m = GetCtrlVal (daq, MUX_Switch7_6, &cross_point[7][6]);
m = GetCtrlVal (daq, MUX_Switch7_7, &cross_point[7][7]);
m = GetCtrlVal (daq, MUX_Switch7_8, &cross_point[7][8]);
m = GetCtrlVal (daq, MUX_Switch8_1, &cross_point[8][1]);
m = GetCtrlVal (daq, MUX_Switch8_2, &cross_point[8][2]);
m = GetCtrlVal (daq, MUX_Switch8_3, &cross_point[8][3]);
m = GetCtrlVal (daq, MUX_Switch8_4, &cross_point[8][4]);
m = GetCtrlVal (daq, MUX_Switch8_5, &cross_point[8][5]);
m = GetCtrlVal (daq, MUX_Switch8_6, &cross_point[8][6]);
m = GetCtrlVal (daq, MUX_Switch8_7, &cross_point[8][7]);
m = GetCtrlVal (daq, MUX_Switch8_8, &cross_point[8][8]);
}
else{
m = GetCtrlVal (daq, MUX_ALL_SWITCHES, &all_switch);
}

```

```

        for(i=1;i<=8;i++){
            for(j=1;j<=8;j++){
                cross_point[i][j]=all_switch;
            }
        }
    }
    m = GetCtrlVal (daq1, MUX1_Switch1_1, &set_bit[1][1]);
    m = GetCtrlVal (daq1, MUX1_Switch1_2, &set_bit[1][2]);
    m = GetCtrlVal (daq1, MUX1_Switch1_3, &set_bit[1][3]);
    m = GetCtrlVal (daq1, MUX1_Switch1_4, &set_bit[1][4]);
    m = GetCtrlVal (daq1, MUX1_Switch1_5, &set_bit[1][5]);
    m = GetCtrlVal (daq1, MUX1_Switch1_6, &set_bit[1][6]);
    m = GetCtrlVal (daq1, MUX1_Switch1_7, &set_bit[1][7]);
    m = GetCtrlVal (daq1, MUX1_Switch1_8, &set_bit[1][8]);
    m = GetCtrlVal (daq1, MUX1_Switch2_1, &set_bit[2][1]);
    m = GetCtrlVal (daq1, MUX1_Switch2_2, &set_bit[2][2]);
    m = GetCtrlVal (daq1, MUX1_Switch2_3, &set_bit[2][3]);
    m = GetCtrlVal (daq1, MUX1_Switch2_4, &set_bit[2][4]);
    m = GetCtrlVal (daq1, MUX1_Switch2_5, &set_bit[2][5]);
    m = GetCtrlVal (daq1, MUX1_Switch2_6, &set_bit[2][6]);
    m = GetCtrlVal (daq1, MUX1_Switch2_7, &set_bit[2][7]);
    m = GetCtrlVal (daq1, MUX1_Switch2_8, &set_bit[2][8]);
    m = GetCtrlVal (daq1, MUX1_Switch3_1, &set_bit[3][1]);
    m = GetCtrlVal (daq1, MUX1_Switch3_2, &set_bit[3][2]);
    m = GetCtrlVal (daq1, MUX1_Switch3_3, &set_bit[3][3]);
    m = GetCtrlVal (daq1, MUX1_Switch3_4, &set_bit[3][4]);
    m = GetCtrlVal (daq1, MUX1_Switch3_5, &set_bit[3][5]);
    m = GetCtrlVal (daq1, MUX1_Switch3_6, &set_bit[3][6]);
    m = GetCtrlVal (daq1, MUX1_Switch3_7, &set_bit[3][7]);
    m = GetCtrlVal (daq1, MUX1_Switch3_8, &set_bit[3][8]);
    m = GetCtrlVal (daq1, MUX1_Switch4_1, &set_bit[4][1]);
    m = GetCtrlVal (daq1, MUX1_Switch4_2, &set_bit[4][2]);
    m = GetCtrlVal (daq1, MUX1_Switch4_3, &set_bit[4][3]);
    m = GetCtrlVal (daq1, MUX1_Switch4_4, &set_bit[4][4]);
    m = GetCtrlVal (daq1, MUX1_Switch4_5, &set_bit[4][5]);
    m = GetCtrlVal (daq1, MUX1_Switch4_6, &set_bit[4][6]);
    m = GetCtrlVal (daq1, MUX1_Switch4_7, &set_bit[4][7]);
    m = GetCtrlVal (daq1, MUX1_Switch4_8, &set_bit[4][8]);
    m = GetCtrlVal (daq1, MUX1_Switch5_1, &set_bit[5][1]);
    m = GetCtrlVal (daq1, MUX1_Switch5_2, &set_bit[5][2]);
    m = GetCtrlVal (daq1, MUX1_Switch5_3, &set_bit[5][3]);
    m = GetCtrlVal (daq1, MUX1_Switch5_4, &set_bit[5][4]);
    m = GetCtrlVal (daq1, MUX1_Switch5_5, &set_bit[5][5]);
    m = GetCtrlVal (daq1, MUX1_Switch5_6, &set_bit[5][6]);
    m = GetCtrlVal (daq1, MUX1_Switch5_7, &set_bit[5][7]);
    m = GetCtrlVal (daq1, MUX1_Switch5_8, &set_bit[5][8]);
    m = GetCtrlVal (daq1, MUX1_Switch6_1, &set_bit[6][1]);
    m = GetCtrlVal (daq1, MUX1_Switch6_2, &set_bit[6][2]);
    m = GetCtrlVal (daq1, MUX1_Switch6_3, &set_bit[6][3]);
    m = GetCtrlVal (daq1, MUX1_Switch6_4, &set_bit[6][4]);
    m = GetCtrlVal (daq1, MUX1_Switch6_5, &set_bit[6][5]);
    m = GetCtrlVal (daq1, MUX1_Switch6_6, &set_bit[6][6]);
    m = GetCtrlVal (daq1, MUX1_Switch6_7, &set_bit[6][7]);
    m = GetCtrlVal (daq1, MUX1_Switch6_8, &set_bit[6][8]);
    m = GetCtrlVal (daq1, MUX1_Switch7_1, &set_bit[7][1]);
    m = GetCtrlVal (daq1, MUX1_Switch7_2, &set_bit[7][2]);
    m = GetCtrlVal (daq1, MUX1_Switch7_3, &set_bit[7][3]);
    m = GetCtrlVal (daq1, MUX1_Switch7_4, &set_bit[7][4]);
    m = GetCtrlVal (daq1, MUX1_Switch7_5, &set_bit[7][5]);
    m = GetCtrlVal (daq1, MUX1_Switch7_6, &set_bit[7][6]);
    m = GetCtrlVal (daq1, MUX1_Switch7_7, &set_bit[7][7]);
    m = GetCtrlVal (daq1, MUX1_Switch7_8, &set_bit[7][8]);
    m = GetCtrlVal (daq1, MUX1_Switch8_1, &set_bit[8][1]);
    m = GetCtrlVal (daq1, MUX1_Switch8_2, &set_bit[8][2]);
    m = GetCtrlVal (daq1, MUX1_Switch8_3, &set_bit[8][3]);
    m = GetCtrlVal (daq1, MUX1_Switch8_4, &set_bit[8][4]);
    m = GetCtrlVal (daq1, MUX1_Switch8_5, &set_bit[8][5]);
    m = GetCtrlVal (daq1, MUX1_Switch8_6, &set_bit[8][6]);
    m = GetCtrlVal (daq1, MUX1_Switch8_7, &set_bit[8][7]);
    m = GetCtrlVal (daq1, MUX1_Switch8_8, &set_bit[8][8]);

```

```

m = GetCtrlVal (daq, MUX_TIME_WRITE, &time_write);
m = GetCtrlVal (daq, MUX_VOLT_WRITE_ON, &volt_write_on);
m = GetCtrlVal (daq, MUX_VOLT_WRITE_OFF, &volt_write_off);
m = GetCtrlVal (daq, MUX_VOLT_HOLD, &volt_hold);
m = GetCtrlVal (daq, MUX_Ramp, &ramp);
m = GetCtrlVal (daq, MUX_Ramp_Rate, &ramp_rate);

/***** starting the loop of configuring *****/

/***** test *****/
m=SetCtrlVal(daq,MUX_STOP_SCAN,1);
m=SetCtrlVal(daq,MUX_Config_complete,0);
m=SetCtrlVal(daq,MUX_Memory_Check_Done,0);
ibwrt(Device1,"CA72X",5);                               /* dummy line */
ibwrt(Device1,"NA72X",5);
for(i=1;i<=8;i++){
    for(j=1;j<=8;j++){
        if (set_bit[i][j]==1){                          /* check if the bit is selected */
            c[0]='C';
            c[1]='B';
            c[2]=(char)(48+i);
            c[3]='X';
            c[4]='\0';
            ibwrt(Device1,c,4);
            c[0]='N';
            c[1]='A';
            c[2]=(char)(48+i);
            c[3]='X';
            c[4]='\0';
            ibwrt(Device1,c,4);
            if (j<2){
                c[0]='C';
                c[1]='C';
                c[2]=(char)(48+j+8);
                c[3]='X';
                c[4]='\0';
                ibwrt(Device1,c,4);
                c[0]='N';
                c[1]='H';
                c[2]=(char)(48+j+8);
                c[3]='X';
                c[4]='\0';
                ibwrt(Device1,c,4);
            }
            else{
                d[0]='C';
                d[1]='C';
                d[2]='1';                               /* two-digit */
                d[3]=(char)(48+j-2);
                d[4]='X';
                d[5]='\0';
                ibwrt(Device1,d,5);
                d[0]='N';
                d[1]='H';
                d[2]='1';                               /* two-digit */
                d[3]=(char)(48+j-2);
                d[4]='X';
                d[5]='\0';
                ibwrt(Device1,d,5);
            }
        }
    }
}
for(k=1;k<=16;k++){
    if((k!=i)&&(k!=j+8)){
        if (k<10){
            if (k<=8){
                c[0]='C';
                c[1]='A';                               /* apply -1.0 volt to rows from Keithley 5-25-01 */
                c[2]=(char)(48+k);
                c[3]='X';
                c[4]='\0';
                ibwrt(Device1,c,4);
            }
        }
    }
}

```

```

    }
    else{
        c[0]='C';
        c[1]='H';

        c[2]=(char)(48+k);
        c[3]='X';
        c[4]='\0';
        ibwrt(Device1,c,4);
    }
}
else{
    d[0]='C';
    d[1]='H';
    d[2]='1';
    d[3]=(char)(48+k-10);
    d[4]='X';
    d[5]='\0';
    ibwrt(Device1,d,5);
}
}
}
/* set write voltage */
Delay(0.1);
printf("\na");
if(ramp==1){
    if(cross_point[i][j]==1){
        volt_ramp0=volt_hold;
        volt_ramp1=0.0;
        for(i_ramp=1; i_ramp<=ramp_num; i_ramp++){
            /* ramp-up */
            volt_ramp0=volt_ramp0 + (volt_write_on/2-volt_hold)/ramp_num;
            volt_ramp1=volt_ramp1 + (volt_write_on/2)/ramp_num;
            m = AO_VWrite (1, 0, volt_ramp0);
            m = AO_VWrite (1, 1, (-volt_ramp1-0.06225)/0.9938);
            Delay(volt_write_on/ramp_num/ramp_rate);
        }
        Delay(time_write); /* hold */
        for(i_ramp=1; i_ramp<=ramp_num; i_ramp++){
            /* ramp-down */
            volt_ramp0=volt_ramp0 - (volt_write_on/2-volt_hold)/ramp_num;
            volt_ramp1=volt_ramp1 - (volt_write_on/2)/ramp_num;
            m = AO_VWrite (1, 0, volt_ramp0);
            m = AO_VWrite (1, 1, (-volt_ramp1-0.06225)/0.9938);
            Delay(volt_write_on/ramp_num/ramp_rate);
        }
    }
}
else{
    volt_ramp0=volt_hold;
    volt_ramp1=0.0;
    for(i_ramp=1; i_ramp<=ramp_num; i_ramp++){
        /* ramp-up */
        volt_ramp0=volt_ramp0 + (volt_write_off/2-
volt_hold)/ramp_num;
        volt_ramp1=volt_ramp1 + (volt_write_off/2)/ramp_num;
        m = AO_VWrite (1, 0, volt_ramp0);
        m = AO_VWrite (1, 1, (-volt_ramp1-0.06225)/0.9938);
        Delay(volt_write_off/ramp_num/ramp_rate);
    }
    Delay(time_write); /* hold */
    for(i_ramp=1; i_ramp<=ramp_num; i_ramp++){
        /* ramp-down */
        volt_ramp0=volt_ramp0 - (volt_write_off/2-volt_hold)/ramp_num;
        volt_ramp1=volt_ramp1 - (volt_write_off/2)/ramp_num;
        m = AO_VWrite (1, 0, volt_ramp0);
        m = AO_VWrite (1, 1, (-volt_ramp1-0.06225)/0.9938);
        Delay(volt_write_off/ramp_num/ramp_rate);
    }
}
}
} /* with ramp */
}

```

```

else{
    if(cross_point[i][j]==1){
        m = AO_VWrite (1, 0, (volt_write_on/2));
        m = AO_VWrite (1, 1, (-volt_write_on/2-0.06225)/0.9938);
    }
    else{
        m = AO_VWrite (1, 0, (volt_write_off/2));
        m = AO_VWrite (1, 1, (-volt_write_off/2-0.06225)/0.9938);
    }
    Delay(time_write);
    m = AO_VWrite (1, 0, volt_hold);
    m = AO_VWrite (1, 1, -0.06225/0.9938);
}
/* no ramp */
/***** set holding voltage to the row, and Ground to the column *****/
c[0]='C';
c[1]='A';
c[2]=(char)(48+i);
c[3]='X';
c[4]='\0';
ibwrt(Device1,c,4);
c[0]='N';
c[1]='B';
c[2]=(char)(48+i);
c[3]='X';
c[4]='\0';
ibwrt(Device1,c,4);
if (j<2){
c[0]='C';
c[1]='H';
c[2]=(char)(48+j+8);
c[3]='X';
c[4]='\0';
ibwrt(Device1,c,4);
c[0]='N';
c[1]='C';
c[2]=(char)(48+j+8);
c[3]='X';
c[4]='\0';
ibwrt(Device1,c,4);
}
else{
d[0]='C';
d[1]='H';
d[2]='1';
d[3]=(char)(48+j-2);
d[4]='X';
d[5]='\0';
ibwrt(Device1,d,5);
d[0]='N';
d[1]='C';
d[2]='1';
d[3]=(char)(48+j-2);
d[4]='X';
d[5]='\0';
ibwrt(Device1,d,5);
}
/*ibwrt(Device1,"POX",3);
} /* finish setting one selected bit */
} /* j */
}
/* close i loop */
m=SetCtrlVal(daq,MUX_Config_complete,1);
return 1;
}
int configure (int panel, int control, int event,
void *callbackData, int eventData1, int eventData2)
{
int i,j,k,m,i_ramp;
char c[5],d[6];
if (all_control !=1){

```

```

m = GetCtrlVal (daq, MUX_Switch1_1, &cross_point[1][1]);
m = GetCtrlVal (daq, MUX_Switch1_2, &cross_point[1][2]);
m = GetCtrlVal (daq, MUX_Switch1_3, &cross_point[1][3]);
m = GetCtrlVal (daq, MUX_Switch1_4, &cross_point[1][4]);
m = GetCtrlVal (daq, MUX_Switch1_5, &cross_point[1][5]);
m = GetCtrlVal (daq, MUX_Switch1_6, &cross_point[1][6]);
m = GetCtrlVal (daq, MUX_Switch1_7, &cross_point[1][7]);
m = GetCtrlVal (daq, MUX_Switch1_8, &cross_point[1][8]);
m = GetCtrlVal (daq, MUX_Switch2_1, &cross_point[2][1]);
m = GetCtrlVal (daq, MUX_Switch2_2, &cross_point[2][2]);
m = GetCtrlVal (daq, MUX_Switch2_3, &cross_point[2][3]);
m = GetCtrlVal (daq, MUX_Switch2_4, &cross_point[2][4]);
m = GetCtrlVal (daq, MUX_Switch2_5, &cross_point[2][5]);
m = GetCtrlVal (daq, MUX_Switch2_6, &cross_point[2][6]);
m = GetCtrlVal (daq, MUX_Switch2_7, &cross_point[2][7]);
m = GetCtrlVal (daq, MUX_Switch2_8, &cross_point[2][8]);
m = GetCtrlVal (daq, MUX_Switch3_1, &cross_point[3][1]);
m = GetCtrlVal (daq, MUX_Switch3_2, &cross_point[3][2]);
m = GetCtrlVal (daq, MUX_Switch3_3, &cross_point[3][3]);
m = GetCtrlVal (daq, MUX_Switch3_4, &cross_point[3][4]);
m = GetCtrlVal (daq, MUX_Switch3_5, &cross_point[3][5]);
m = GetCtrlVal (daq, MUX_Switch3_6, &cross_point[3][6]);
m = GetCtrlVal (daq, MUX_Switch3_7, &cross_point[3][7]);
m = GetCtrlVal (daq, MUX_Switch3_8, &cross_point[3][8]);
m = GetCtrlVal (daq, MUX_Switch4_1, &cross_point[4][1]);
m = GetCtrlVal (daq, MUX_Switch4_2, &cross_point[4][2]);
m = GetCtrlVal (daq, MUX_Switch4_3, &cross_point[4][3]);
m = GetCtrlVal (daq, MUX_Switch4_4, &cross_point[4][4]);
m = GetCtrlVal (daq, MUX_Switch4_5, &cross_point[4][5]);
m = GetCtrlVal (daq, MUX_Switch4_6, &cross_point[4][6]);
m = GetCtrlVal (daq, MUX_Switch4_7, &cross_point[4][7]);
m = GetCtrlVal (daq, MUX_Switch4_8, &cross_point[4][8]);
m = GetCtrlVal (daq, MUX_Switch5_1, &cross_point[5][1]);
m = GetCtrlVal (daq, MUX_Switch5_2, &cross_point[5][2]);
m = GetCtrlVal (daq, MUX_Switch5_3, &cross_point[5][3]);
m = GetCtrlVal (daq, MUX_Switch5_4, &cross_point[5][4]);
m = GetCtrlVal (daq, MUX_Switch5_5, &cross_point[5][5]);
m = GetCtrlVal (daq, MUX_Switch5_6, &cross_point[5][6]);
m = GetCtrlVal (daq, MUX_Switch5_7, &cross_point[5][7]);
m = GetCtrlVal (daq, MUX_Switch5_8, &cross_point[5][8]);
m = GetCtrlVal (daq, MUX_Switch6_1, &cross_point[6][1]);
m = GetCtrlVal (daq, MUX_Switch6_2, &cross_point[6][2]);
m = GetCtrlVal (daq, MUX_Switch6_3, &cross_point[6][3]);
m = GetCtrlVal (daq, MUX_Switch6_4, &cross_point[6][4]);
m = GetCtrlVal (daq, MUX_Switch6_5, &cross_point[6][5]);
m = GetCtrlVal (daq, MUX_Switch6_6, &cross_point[6][6]);
m = GetCtrlVal (daq, MUX_Switch6_7, &cross_point[6][7]);
m = GetCtrlVal (daq, MUX_Switch6_8, &cross_point[6][8]);
m = GetCtrlVal (daq, MUX_Switch7_1, &cross_point[7][1]);
m = GetCtrlVal (daq, MUX_Switch7_2, &cross_point[7][2]);
m = GetCtrlVal (daq, MUX_Switch7_3, &cross_point[7][3]);
m = GetCtrlVal (daq, MUX_Switch7_4, &cross_point[7][4]);
m = GetCtrlVal (daq, MUX_Switch7_5, &cross_point[7][5]);
m = GetCtrlVal (daq, MUX_Switch7_6, &cross_point[7][6]);
m = GetCtrlVal (daq, MUX_Switch7_7, &cross_point[7][7]);
m = GetCtrlVal (daq, MUX_Switch7_8, &cross_point[7][8]);
m = GetCtrlVal (daq, MUX_Switch8_1, &cross_point[8][1]);
m = GetCtrlVal (daq, MUX_Switch8_2, &cross_point[8][2]);
m = GetCtrlVal (daq, MUX_Switch8_3, &cross_point[8][3]);
m = GetCtrlVal (daq, MUX_Switch8_4, &cross_point[8][4]);
m = GetCtrlVal (daq, MUX_Switch8_5, &cross_point[8][5]);
m = GetCtrlVal (daq, MUX_Switch8_6, &cross_point[8][6]);
m = GetCtrlVal (daq, MUX_Switch8_7, &cross_point[8][7]);
m = GetCtrlVal (daq, MUX_Switch8_8, &cross_point[8][8]);
}
else{
    m = GetCtrlVal (daq, MUX_ALL_SWITCHES, &all_switch);
    for(i=1;i<=8;i++){
        for(j=1;j<=8;j++){

```



```

c[4]='\0';
ibwrt(Device1,c,4);
if (j<4){
c[0]='C';
c[1]='A';
c[2]=(char)(48+j+6);
c[3]='X';
c[4]='\0';
ibwrt(Device1,c,4);
}
else{
d[0]='C';
d[1]='A';
d[2]='1';
d[3]=(char)(48+j-4);
d[4]='X';
d[5]='\0';
ibwrt(Device1,d,5);
}
}
2-17-01 */
for(k=1;k<=16;k++){
if((k!=i)&&(k!=j+8)){
if (k<10){
if (k<=8){
c[0]='C';
c[1]='A'; /* apply -1.0 volt to rows from Keithley 5-25-01 */
c[2]=(char)(48+k);
c[3]='X';
c[4]='\0';
ibwrt(Device1,c,4);
}
else{
c[0]='C';
c[1]='H';

/* Ground the columns */
c[2]=(char)(48+k);
c[3]='X';
c[4]='\0';
ibwrt(Device1,c,4);
}
}
else{
d[0]='C';
d[1]='H';
d[2]='1';
d[3]=(char)(48+k-10);
d[4]='X';
d[5]='\0';
ibwrt(Device1,d,5);
}
}
}
}
/* set write voltage */
Delay(0.1);
printf("\a");
if(ramp==1){
if(cross_point[i][j]==1){
volt_ramp0=volt_hold;
volt_ramp1=0.0;
for(i_ramp=1; i_ramp<=ramp_num; i_ramp++){
/* ramp-up */
volt_ramp0=volt_ramp0 + (volt_write_on/2-volt_hold)/ramp_num;
volt_ramp1=volt_ramp1 + (volt_write_on/2)/ramp_num;
m = AO_VWrite (1, 0, volt_ramp0);
m = AO_VWrite (1, 1, (-volt_ramp1-0.06225)/0.9938);
Delay(volt_write_on/ramp_num/ramp_rate);
Delay(-volt_write_on/ramp_num/ramp_rate);
}
}
}
}

```

```

Delay(time_write);                                     /* hold */
for(i_ramp=1; i_ramp<=ramp_num; i_ramp++){
/* ramp-down */
    volt_ramp0=volt_ramp0 - (volt_write_on/2-volt_hold)/ramp_num;
    volt_ramp1=volt_ramp1 - (volt_write_on/2)/ramp_num;
    m = AO_VWrite (1, 0, volt_ramp0);
    m = AO_VWrite (1, 1, (-volt_ramp1-0.06225)/0.9938);
    Delay(volt_write_on/ramp_num/ramp_rate);
    Delay(-volt_write_on/ramp_num/ramp_rate);
}
}
else{
    volt_ramp0=volt_hold;
    volt_ramp1=0.0;
    for(i_ramp=1; i_ramp<=ramp_num; i_ramp++){
/* ramp-up */
        volt_ramp0=volt_ramp0 + (volt_write_off/2-
volt_hold)/ramp_num;
        volt_ramp1=volt_ramp1 + (volt_write_off/2)/ramp_num;
        m = AO_VWrite (1, 0, volt_ramp0);
        m = AO_VWrite (1, 1, (-volt_ramp1-0.06225)/0.9938);
        Delay(volt_write_off/ramp_num/ramp_rate);
        Delay(-volt_write_off/ramp_num/ramp_rate);
    }
    Delay(time_write);                                 /* hold */
    for(i_ramp=1; i_ramp<=ramp_num; i_ramp++){
/* ramp-down */
        volt_ramp0=volt_ramp0 - (volt_write_off/2-volt_hold)/ramp_num;
        volt_ramp1=volt_ramp1 - (volt_write_off/2)/ramp_num;
        m = AO_VWrite (1, 0, volt_ramp0);
        m = AO_VWrite (1, 1, (-volt_ramp1-0.06225)/0.9938);
        Delay(volt_write_off/ramp_num/ramp_rate);
        Delay(-volt_write_off/ramp_num/ramp_rate);
    }
}
} /* with ramp */
else{
    if(cross_point[i][j]==1){
        m = AO_VWrite (1, 0, (volt_write_on/2));
        m = AO_VWrite (1, 1, (-volt_write_on/2-0.06225)/0.9938);
    }
    else{
        m = AO_VWrite (1, 0, (volt_write_off/2));
        m = AO_VWrite (1, 1, (-volt_write_off/2-0.06225)/0.9938);
    }
    Delay(time_write);
    m = AO_VWrite (1, 0, volt_hold);
    m = AO_VWrite (1, 1, -0.06225/0.9938);
} /* no ramp */
}
/***** set holding voltage to the row, and Ground to the column *****/
c[0]='C';
c[1]='A';
c[2]=(char)(48+i);
c[3]='X';
c[4]='\0';
ibwrt(Device1,c,4);
c[0]='N';
c[1]='B';
c[2]=(char)(48+i);
c[3]='X';
c[4]='\0';
ibwrt(Device1,c,4);
if (j<2){
c[0]='C';
c[1]='H';
c[2]=(char)(48+j+8);
c[3]='X';
c[4]='\0';
ibwrt(Device1,c,4);
c[0]='N';

```

```

        c[1]='C';
        c[2]=(char)(48+j+8);
        c[3]='X';
        c[4]='\0';
        ibwrt(Device1,c,4);
    }
    else{
        d[0]='C';
        d[1]='H';
        d[2]='1';
        d[3]=(char)(48+j-2);
        d[4]='X';
        d[5]='\0';
        ibwrt(Device1,d,5);
        d[0]='N';
        d[1]='C';
        d[2]='1';
        d[3]=(char)(48+j-2);
        d[4]='X';
        d[5]='\0';
        ibwrt(Device1,d,5);
    }
    /* ibwrt(Device1,"POX",3);          /* open all relays (skipped 5-25-01) */
}
}
/* close the loop */
m=SetCtrlVal(daq,MUX_Config_complete,1);
return 1;
}
int logic_check(int panel, int control, int event,
                void *callbackData, int eventData1, int eventData2){
    /*SetCtrlVal(daq,MUX_STOP_SCAN,1); */
    return 1;
}
int memory_check(int panel, int control, int event,
                 void *callbackData, int eventData1, int eventData2){
    /*SetCtrlVal(daq,MUX_STOP_SCAN,1); */
    int i,j,k,ii,m;
    double r_dummy;
    int fail[9][9];
    double AD0[9][9][100],AD1[9][9][100];
    char c[5],d[6];
    DeleteGraphPlot (daq, MUX_GRAPH, -1, VAL_IMMEDIATE_DRAW);
    m=SetCtrlVal(daq,MUX_Memory_Check_Done,0);
    m=SetCtrlVal(daq,MUX_Set_phase,0);
/*
    m=SetCtrlAttribute(daq,MUX_switch1_1r, ATTR_DIMMED, TRUE);
    m=SetCtrlAttribute(daq,MUX_switch1_2r, ATTR_DIMMED, TRUE);
    m=SetCtrlAttribute(daq,MUX_switch1_3r, ATTR_DIMMED, TRUE);
    m=SetCtrlAttribute(daq,MUX_switch1_4r, ATTR_DIMMED, TRUE);
    m=SetCtrlAttribute(daq,MUX_switch1_5r, ATTR_DIMMED, TRUE);
    m=SetCtrlAttribute(daq,MUX_switch1_6r, ATTR_DIMMED, TRUE);
    m=SetCtrlAttribute(daq,MUX_switch2_1r, ATTR_DIMMED, TRUE);
    m=SetCtrlAttribute(daq,MUX_switch2_2r, ATTR_DIMMED, TRUE);
    m=SetCtrlAttribute(daq,MUX_switch2_3r, ATTR_DIMMED, TRUE);
    m=SetCtrlAttribute(daq,MUX_switch2_4r, ATTR_DIMMED, TRUE);
    m=SetCtrlAttribute(daq,MUX_switch2_5r, ATTR_DIMMED, TRUE);
    m=SetCtrlAttribute(daq,MUX_switch2_6r, ATTR_DIMMED, TRUE);
    m=SetCtrlAttribute(daq,MUX_switch3_1r, ATTR_DIMMED, TRUE);
    m=SetCtrlAttribute(daq,MUX_switch3_2r, ATTR_DIMMED, TRUE);
    m=SetCtrlAttribute(daq,MUX_switch3_3r, ATTR_DIMMED, TRUE);
    m=SetCtrlAttribute(daq,MUX_switch3_4r, ATTR_DIMMED, TRUE);
    m=SetCtrlAttribute(daq,MUX_switch3_5r, ATTR_DIMMED, TRUE);
    m=SetCtrlAttribute(daq,MUX_switch3_6r, ATTR_DIMMED, TRUE);
    m=SetCtrlAttribute(daq,MUX_switch4_1r, ATTR_DIMMED, TRUE);
    m=SetCtrlAttribute(daq,MUX_switch4_2r, ATTR_DIMMED, TRUE);
    m=SetCtrlAttribute(daq,MUX_switch4_3r, ATTR_DIMMED, TRUE);
    m=SetCtrlAttribute(daq,MUX_switch4_4r, ATTR_DIMMED, TRUE);
    m=SetCtrlAttribute(daq,MUX_switch4_5r, ATTR_DIMMED, TRUE);
    m=SetCtrlAttribute(daq,MUX_switch4_6r, ATTR_DIMMED, TRUE);

```

```

m=SetCtrlAttribute(daq,MUX_switch5_1r, ATTR_DIMMED, TRUE);
m=SetCtrlAttribute(daq,MUX_switch5_2r, ATTR_DIMMED, TRUE);
m=SetCtrlAttribute(daq,MUX_switch5_3r, ATTR_DIMMED, TRUE);
m=SetCtrlAttribute(daq,MUX_switch5_4r, ATTR_DIMMED, TRUE);
m=SetCtrlAttribute(daq,MUX_switch5_5r, ATTR_DIMMED, TRUE);
m=SetCtrlAttribute(daq,MUX_switch5_6r, ATTR_DIMMED, TRUE);
m=SetCtrlAttribute(daq,MUX_switch6_1r, ATTR_DIMMED, TRUE);
m=SetCtrlAttribute(daq,MUX_switch6_2r, ATTR_DIMMED, TRUE);
m=SetCtrlAttribute(daq,MUX_switch6_3r, ATTR_DIMMED, TRUE);
m=SetCtrlAttribute(daq,MUX_switch6_4r, ATTR_DIMMED, TRUE);
m=SetCtrlAttribute(daq,MUX_switch6_5r, ATTR_DIMMED, TRUE);
m=SetCtrlAttribute(daq,MUX_switch6_6r, ATTR_DIMMED, TRUE);
12-12-01 LED's removed and kept in an untitled panel */
for(i=1;i<=8;i++){
    for(j=1;j<=8;j++){
        PlotLine(daq, MUX_GRAPH, (i-1)*8+(j-1), cross_point[i][j], (i-1)*8+j, cross_point[i][j],VAL_BLUE);
    }
}
m = GetCtrlVal (daq, MUX_TIME_READ, &time_read);
m = GetCtrlVal (daq, MUX_VOLT_READ, &volt_read);
m = GetCtrlVal (daq, MUX_Threshold_High, &threshold_high);
m = GetCtrlVal (daq, MUX_Threshold_Low, &threshold_low);
m = GetCtrlVal (daq, MUX_NUM_READ, &num_read);
m = GetCtrlVal (daq, MUX_VOLT_HOLD, &volt_hold);
fp_out=fopen(tmp_file,"w");
/* Device1=ibdev(0,18,0,10,1,0);          /* initiate 707A */
/* ibwrt(Device1,"E0X",3);                /* Point to present relays */
for(i=1;i<=8;i++){
    for(j=1;j<=8;j++){
        c[0]='C';
        c[1]='D';          /* use relay row D to read (Vread+AC from function generator) */
        2]=(char)(48+i);
        c[3]='X';
        c[4]='\0';
        ibwrt(Device1,c,4);
        c[0]='N';
        c[1]='A';
        c[2]=(char)(48+i);
        c[3]='X';
        c[4]='\0';
        ibwrt(Device1,c,4);
        if (j<2){
            c[0]='C';
            c[1]='G';          /* amp-meter */
            c[2]=(char)(48+j+8);
            c[3]='X';
            c[4]='\0';
            ibwrt(Device1,c,4);
            c[0]='N';
            c[1]='H';          /* GND */
            c[2]=(char)(48+j+8);
            c[3]='X';
            c[4]='\0';
            ibwrt(Device1,c,4);
        }
        else{
            d[0]='C';
            d[1]='G';          /* amp-meter */
            d[2]='1';
            d[3]=(char)(48+j-2);
            d[4]='X';
            d[5]='\0';
            ibwrt(Device1,d,5);
            d[0]='N';
            d[1]='H';          /* GND */
            d[2]='1';
            d[3]=(char)(48+j-2);
            d[4]='X';
            d[5]='\0';
            ibwrt(Device1,d,5);
        }
    }
}

```

```

    }
    for(k=1;k<=16;k++){
        if((k!=i)&&(k!=j+8)){
            if (k<10){
                if (k<=8){
                    c[0]='C';
                    c[1]='A'; /* apply -1.0 volt to rows from Keithley 5-25-01 */
                    c[2]=(char)(48+k);
                    c[3]='X';
                    c[4]='\0';
                    ibwrt(Device1,c,4);
                }
                else{
                    c[0]='C';
                    c[1]='H';

/* Ground the columns */

                    c[2]=(char)(48+k);
                    c[3]='X';
                    c[4]='\0';
                    ibwrt(Device1,c,4);
                }
            }
            else{
                d[0]='C';
                d[1]='H';
                d[2]='1';
                d[3]=(char)(48+k-10);
                d[4]='X';
                d[5]='\0';
                ibwrt(Device1,d,5);
            }
        }
    }

/* set read voltage and measure the current */
/* Delay (0.1); 5-25-01 */
printf("\na");
m = AO_VWrite (1, 0, volt_read); /* channel 0's output goes to relay row B directly
and goes to row D through function generator */
Delay (0.1); /* delay after setting the read voltage */
/*manually set phase on the lock-in 5_28_01 */
/*
m=SetCtrlVal(daq,MUX_Set_phase,1);
scanf("%f",r_dummy);
m=SetCtrlVal(daq,MUX_Set_phase,0); taken out for non-volatile devices 6-5-01*/

for (ii=0;ii<num_read;ii++){
    m = AI_VRead (1, 0, 1, &adch0); /* output from current amplifier */
    m = AI_VRead (1, 1, 1, &adch1); /* output from lock-in amplifier */

    AD0[i][j][ii]=-adch0; /**** Current Amplifier revise the polarity!! *****/
    AD1[i][j][ii]=adch1;

    if(ii>0) m=PlotLine (daq, MUX_GRAPH, 8.0*(i-1)+j-1+(double)(ii)/(double)(num_read-1),
AD0[i][j][ii-1], 8.0*(i-1)+j-1+(double)(ii)/(double)(num_read-1), AD0[i][j][ii], VAL_RED);
    if(ii>0) m=PlotLine (daq, MUX_GRAPH, 8.0*(i-1)+j-1+(double)(ii-1)/(double)(num_read-1),
AD1[i][j][ii-1], 8.0*(i-1)+j-1+(double)(ii)/(double)(num_read-1), AD1[i][j][ii], VAL_GREEN);

    Delay (time_read/num_read);
}
/***** set holding voltage to the row, and Ground to the column *****/
c[0]='C';
c[1]='A';
c[2]=(char)(48+i);
c[3]='X';
c[4]='\0';
ibwrt(Device1,c,4);
c[0]='N';
c[1]='D';
c[2]=(char)(48+i);

```

```

c[3]='X';
c[4]='\0';
ibwrt(Device1,c,4);
if (j<2){
c[0]='C';
c[1]='H';
c[2]=(char)(48+j+8);
c[3]='X';
c[4]='\0';
ibwrt(Device1,c,4);
c[0]='N';
c[1]='G';
c[2]=(char)(48+j+8);
c[3]='X';
c[4]='\0';
ibwrt(Device1,c,4);
}
else{
d[0]='C';
d[1]='H';
d[2]='1'; /* two-digit */
d[3]=(char)(48+j-2);
d[4]='X';
d[5]='\0';
ibwrt(Device1,d,5);
d[0]='N';
d[1]='G';
d[2]='1'; /* two-digit */
d[3]=(char)(48+j-2);
d[4]='X';
d[5]='\0';
ibwrt(Device1,d,5);
}
fail[i][j]=0;
if(cross_point[i][j]==0){
for (ii=0;ii<num_read;ii++){
if(AD0[i][j][ii]>threshold_low) {
fail[i][j]=1;
break;
}
}
}
if(cross_point[i][j]==1){
for (ii=0;ii<num_read;ii++){
if(AD0[i][j][ii]<threshold_high) {
fail[i][j]=1;
break;
}
}
}
/* m = AO_VWrite (1, 0, 0.0);
ibwrt(Device1,"POX",3); 5-25-01 */
}
}
/* close the loop */

/***** set holding voltage to the rows, and Ground to the columns *****/
for(k=1;k<=16;k++){
if (k<10){
if (k<=8){
c[0]='C';
c[1]='A'; /* apply -1.0 volt to rows from Keithley 5-25-01 */
c[2]=(char)(48+k);
c[3]='X';
c[4]='\0';
ibwrt(Device1,c,4);
}
else{
c[0]='C';
c[1]='H'; /* Ground the columns */

```

```

        c[2]=(char)(48+k);
        c[3]='X';
        c[4]='\0';
        ibwrt(Device1,c,4);
    }
    else{
        d[0]='C';
        d[1]='H';
        d[2]='1';
        d[3]=(char)(48+k-10);
        d[4]='X';
        d[5]='\0';
        ibwrt(Device1,d,5);
    }
}

/*
if(fail[1][1]==0) {
    m=SetCtrlAttribute(daq,MUX_switch1_1r, ATTR_DIMMED, FALSE);
    m=SetCtrlVal(daq,MUX_switch1_1r,cross_point[1][1]);}
if(fail[1][2]==0) {
    m=SetCtrlAttribute(daq,MUX_switch1_2r, ATTR_DIMMED, FALSE);
    m=SetCtrlVal(daq,MUX_switch1_2r,cross_point[1][2]);}
if(fail[1][3]==0) {
    m=SetCtrlAttribute(daq,MUX_switch1_3r, ATTR_DIMMED, FALSE);
    m=SetCtrlVal(daq,MUX_switch1_3r,cross_point[1][3]);}
if(fail[1][4]==0) {
    m=SetCtrlAttribute(daq,MUX_switch1_4r, ATTR_DIMMED, FALSE);
    m=SetCtrlVal(daq,MUX_switch1_4r,cross_point[1][4]);}
if(fail[1][5]==0) {
    m=SetCtrlAttribute(daq,MUX_switch1_5r, ATTR_DIMMED, FALSE);
    m=SetCtrlVal(daq,MUX_switch1_5r,cross_point[1][5]);}
if(fail[1][6]==0) {
    m=SetCtrlAttribute(daq,MUX_switch1_6r, ATTR_DIMMED, FALSE);
    m=SetCtrlVal(daq,MUX_switch1_6r,cross_point[1][6]);}
if(fail[2][1]==0) {
    m=SetCtrlAttribute(daq,MUX_switch2_1r, ATTR_DIMMED, FALSE);
    m=SetCtrlVal(daq,MUX_switch2_1r,cross_point[2][1]);}
if(fail[2][2]==0) {
    m=SetCtrlAttribute(daq,MUX_switch2_2r, ATTR_DIMMED, FALSE);
    m=SetCtrlVal(daq,MUX_switch2_2r,cross_point[2][2]);}
if(fail[2][3]==0) {
    m=SetCtrlAttribute(daq,MUX_switch2_3r, ATTR_DIMMED, FALSE);
    m=SetCtrlVal(daq,MUX_switch2_3r,cross_point[2][3]);}
if(fail[2][4]==0) {
    m=SetCtrlAttribute(daq,MUX_switch2_4r, ATTR_DIMMED, FALSE);
    m=SetCtrlVal(daq,MUX_switch2_4r,cross_point[2][4]);}
if(fail[2][5]==0) {
    m=SetCtrlAttribute(daq,MUX_switch2_5r, ATTR_DIMMED, FALSE);
    m=SetCtrlVal(daq,MUX_switch2_5r,cross_point[2][5]);}
if(fail[2][6]==0) {
    m=SetCtrlAttribute(daq,MUX_switch2_6r, ATTR_DIMMED, FALSE);
    m=SetCtrlVal(daq,MUX_switch2_6r,cross_point[2][6]);}
if(fail[3][1]==0) {
    m=SetCtrlAttribute(daq,MUX_switch3_1r, ATTR_DIMMED, FALSE);
    m=SetCtrlVal(daq,MUX_switch3_1r,cross_point[3][1]);}
if(fail[3][2]==0) {
    m=SetCtrlAttribute(daq,MUX_switch3_2r, ATTR_DIMMED, FALSE);
    m=SetCtrlVal(daq,MUX_switch3_2r,cross_point[3][2]);}
if(fail[3][3]==0) {
    m=SetCtrlAttribute(daq,MUX_switch3_3r, ATTR_DIMMED, FALSE);
    m=SetCtrlVal(daq,MUX_switch3_3r,cross_point[3][3]);}
if(fail[3][4]==0) {
    m=SetCtrlAttribute(daq,MUX_switch3_4r, ATTR_DIMMED, FALSE);
    m=SetCtrlVal(daq,MUX_switch3_4r,cross_point[3][4]);}
if(fail[3][5]==0) {
    m=SetCtrlAttribute(daq,MUX_switch3_5r, ATTR_DIMMED, FALSE);
    m=SetCtrlVal(daq,MUX_switch3_5r,cross_point[3][5]);}
if(fail[3][6]==0) {
    m=SetCtrlAttribute(daq,MUX_switch3_6r, ATTR_DIMMED, FALSE);

```

```

        m=SetCtrlVal(daq,MUX_switch3_6r,cross_point[3][6]);}
if(fail[4][1]==0) {
    m=SetCtrlAttribute(daq,MUX_switch4_1r, ATTR_DIMMED, FALSE);
    m=SetCtrlVal(daq,MUX_switch4_1r,cross_point[4][1]);}
if(fail[4][2]==0) {
    m=SetCtrlAttribute(daq,MUX_switch4_2r, ATTR_DIMMED, FALSE);
    m=SetCtrlVal(daq,MUX_switch4_2r,cross_point[4][2]);}
if(fail[4][3]==0) {
    m=SetCtrlAttribute(daq,MUX_switch4_3r, ATTR_DIMMED, FALSE);
    m=SetCtrlVal(daq,MUX_switch4_3r,cross_point[4][3]);}
if(fail[4][4]==0) {
    m=SetCtrlAttribute(daq,MUX_switch4_4r, ATTR_DIMMED, FALSE);
    m=SetCtrlVal(daq,MUX_switch4_4r,cross_point[4][4]);}
if(fail[4][5]==0) {
    m=SetCtrlAttribute(daq,MUX_switch4_5r, ATTR_DIMMED, FALSE);
    m=SetCtrlVal(daq,MUX_switch4_5r,cross_point[4][5]);}
if(fail[4][6]==0) {
    m=SetCtrlAttribute(daq,MUX_switch4_6r, ATTR_DIMMED, FALSE);
    m=SetCtrlVal(daq,MUX_switch4_6r,cross_point[4][6]);}

if(fail[5][1]==0) {
    m=SetCtrlAttribute(daq,MUX_switch5_1r, ATTR_DIMMED, FALSE);
    m=SetCtrlVal(daq,MUX_switch5_1r,cross_point[5][1]);}
if(fail[5][2]==0) {
    m=SetCtrlAttribute(daq,MUX_switch5_2r, ATTR_DIMMED, FALSE);
    m=SetCtrlVal(daq,MUX_switch5_2r,cross_point[5][2]);}
if(fail[5][3]==0) {
    m=SetCtrlAttribute(daq,MUX_switch5_3r, ATTR_DIMMED, FALSE);
    m=SetCtrlVal(daq,MUX_switch5_3r,cross_point[5][3]);}
if(fail[5][4]==0) {
    m=SetCtrlAttribute(daq,MUX_switch5_4r, ATTR_DIMMED, FALSE);
    m=SetCtrlVal(daq,MUX_switch5_4r,cross_point[5][4]);}
if(fail[5][5]==0) {
    m=SetCtrlAttribute(daq,MUX_switch5_5r, ATTR_DIMMED, FALSE);
    m=SetCtrlVal(daq,MUX_switch5_5r,cross_point[5][5]);}
if(fail[5][6]==0) {
    m=SetCtrlAttribute(daq,MUX_switch5_6r, ATTR_DIMMED, FALSE);
    m=SetCtrlVal(daq,MUX_switch5_6r,cross_point[5][6]);}
if(fail[6][1]==0) {
    m=SetCtrlAttribute(daq,MUX_switch6_1r, ATTR_DIMMED, FALSE);
    m=SetCtrlVal(daq,MUX_switch6_1r,cross_point[6][1]);}
if(fail[6][2]==0) {
    m=SetCtrlAttribute(daq,MUX_switch6_2r, ATTR_DIMMED, FALSE);
    m=SetCtrlVal(daq,MUX_switch6_2r,cross_point[6][2]);}
if(fail[6][3]==0) {
    m=SetCtrlAttribute(daq,MUX_switch6_3r, ATTR_DIMMED, FALSE);
    m=SetCtrlVal(daq,MUX_switch6_3r,cross_point[6][3]);}
if(fail[6][4]==0) {
    m=SetCtrlAttribute(daq,MUX_switch6_4r, ATTR_DIMMED, FALSE);
    m=SetCtrlVal(daq,MUX_switch6_4r,cross_point[6][4]);}
if(fail[6][5]==0) {
    m=SetCtrlAttribute(daq,MUX_switch6_5r, ATTR_DIMMED, FALSE);
    m=SetCtrlVal(daq,MUX_switch6_5r,cross_point[6][5]);}
if(fail[6][6]==0) {
    m=SetCtrlAttribute(daq,MUX_switch6_6r, ATTR_DIMMED, FALSE);
    m=SetCtrlVal(daq,MUX_switch6_6r,cross_point[6][6]);}

12-12-01  taken out, because the LED's are removed*/

m=SetCtrlVal(daq,MUX_Memory_Check_Done,1);
for(i=1;i<=8;i++){
    for(j=1;j<=8;j++){
        for (k=0;k<num_read;k++){
            fprintf(fp_out, "%d %d %d %f %f\n", i, j, cross_point[i][j], AD0[i][j][k], AD1[i][j][k]);
        }
    }
}
fclose(fp_out);
return 1;
}

```

```

int stop(int panel, int control, int event,
        void *callbackData, int eventData1, int eventData2){
    return 1;
}

int save_file(int panel, int control, int event,
            void *callbackData, int eventData1, int eventData2){
    int i;
    int tmp1[6400],tmp2[6400],tmp3[6400];
    float tmp4[6400], tmp5[6400];
    char line[100];
    char name[30];
    fp_out=fopen (tmp_file,"r");
    for (i = 0; i < num_read*64; ++i)
        {
            fgets(line,sizeof(line),fp_out);
            sscanf(line,"%d %d %d %f %f", &tmp1[i], &tmp2[i], &tmp3[i], &tmp4[i], &tmp5[i]);
        }
    fclose(fp_out);
    PromptPopup ("SAVE FILE", "Enter the file name (*.txt).", name, 20);
    fp_out=fopen(name,"w");
    for (i =0; i < num_read*64; ++i)
        fprintf(fp_out,"%d %f %f\n",tmp3[i], tmp4[i], tmp5[i]);
    fclose(fp_out);
    return 1;
}

int quit(int panel, int control, int event,
        void *callbackData, int eventData1, int eventData2)
{
    int i;
    switch (event) {
        case EVENT_COMMIT:
            i = AO_VWrite (1, 0, 0.0);
            i = AO_VWrite (1, 1, 0.0);
            ibwrt(Device1,"POX",3);
            QuitUserInterface (0);
            break;
        case EVENT_RIGHT_CLICK:
            break;
    }
    return 0;
}
/*
int load_individual_panel (int panel, int control, int event, void *callbackData, int eventData1, int eventData2)
{
    daq1 = LoadPanel (0, "MUX.uir",SET_INDIVI);
    DisplayPanel (daq1);
    return 0;
}
*/

int clear (int panel, int control, int event,
        void *callbackData, int eventData1, int eventData2)
{
    int i;
    switch (event) {
        case EVENT_COMMIT:
            DeleteGraphPlot (daq, MUX_GRAPH, -1, VAL_IMMEDIATE_DRAW);
            DeleteGraphPlot (daq, DAQ_GRAPH_2, -1, VAL_IMMEDIATE_DRAW);
            break;
    }
    return 0;
}

```